NASA TECHNICAL NOTE

NASA TN D-7184

NASA TN D-7184

A MULTISPECTRAL STUDY OF AN EXTRATROPICAL CYCLONE WITH NIMBUS 3 MEDIUM RESOLUTION INFRARED RADIOMETER DATA

by Robert Holub and William E. Shenk

Goddard Space Flight Center
Greenbelt, Md. 20771

1. Report No. NASA TN D–7184	2. Government Accession No.	3. Recipient's Catalog No.
4. Title and Subtitle A Multispectral Study of an Extratropical Cyclone With Nimbus 3 Medium Resolution Infrared Radiometer Data		5. Report Date **November 1973**
		6. Performing Organization Code 651
7. Author(s) Robert Holub and William E. Shenk		8. Performing Organization Report No. G-1085
9. Performing Organization Name and Address Goddard Space Flight Center Greenbelt, Maryland 20771		10. Work Unit No. 160-44-51-01
		11. Contract or Grant No.
12. Sponsoring Agency Name and Address National Aeronautics and Space Administration Washington, D.C. 20546		13. Type of Report and Period Covered Technical Note
		14. Sponsoring Agency Code
15. Supplementary Notes		

16. Abstract

   Four registered channels (0.2 to 4, 6.5 to 7, 10 to 11, and 20 to 23 μm) of the Nimbus 3 Medium Resolution Infrared Radiometer (MRIR) were used to study 24-hr changes in the structure of an extratropical cyclone during a 6-day period in May 1969. Use of a stereographic-horizon map projection insured that the storm was mapped with a single perspective throughout the series and allowed the convenient preparation of 24-hr difference maps of the infrared radiation fields. Single-channel and multispectral analysis techniques were employed to establish the positions and vertical slopes of jetstreams, large cloud systems, and major features of middle and upper tropospheric circulation. Use of these techniques plus the difference maps and continuity of observation allowed the early detection of secondary cyclones developing within the circulation of the primary cyclone. An automated, multispectral cloud-type identification technique was developed, and comparisons that were made with conventional ship reports and with high-resolution visual data from the image dissector camera system (IDCS) showed good agreement.

17. Key Words (Selected by Author(s)) Extratropical cyclones Satellite radiation data Cloud-type identification		18. Distribution Statement Unclassified–Unlimited		
19. Security Classif. (of this report) Unclassified	20. Security Classif. (of this page) Unclassified		21. No. of Pages 71	22. Price* **Domestic, $3.50** **Foreign, $6.00**

CONTENTS

A MULTISPECTRAL STUDY OF
AN EXTRATROPICAL CYCLONE WITH NIMBUS 3
MEDIUM RESOLUTION INFRARED RADIOMETER DATA

Robert Holub
*Environmental Technical Applications Center**

and

William E. Shenk
Goddard Space Flight Center

INTRODUCTION

Many investigators have shown that significant features of extratropical cyclones can be successfully observed from a satellite platform (ref. 1). This paper documents the day-to-day changes in the structure of an Atlantic cyclone in four registered spectral regions (channels) of the Nimbus 3 medium resolution infrared radiometer (MRIR) sensor. In addition, Nimbus 3 pictures from the image dissector camera system (IDCS) and standard surface and upper-air data were used to complement the MRIR information.

BACKGROUND

Early satellite visible imagery revealed that extratropical as well as tropical cyclones are associated with distinctive cloud patterns (refs. 2 and 3). Satellite imagery was used to show that these cloud patterns evolve in a manner that fits the classical Norwegian extratropical cyclone model (refs. 4 and 5). Cyclone identification and tracking techniques are currently used extensively and are summarized in publications such as those of the World Meteorological Organization (ref. 6) and the Environmental Science Services Administration (ref. 7).

Window infrared measurements have been applied to the study of cyclone development and movement (ref. 8). Sherr and Rogers (ref. 9) used Tiros 4 data to show that wave development on fronts is marked by significant cloud growth. Similarly, Shenk (ref. 10) has noted that new cyclogenesis within an old vortex can be detected by monitoring abrupt changes in cloud height. Other studies have related actual cyclone parameters such as central pressure and intensity to the radiation fields associated with cyclones (refs. 11 to 13). The advent of multispectral infrared sensors on geostationary satellites and microwave instruments on satellites in near-Earth orbit in the future promise new knowledge in cyclone studies.

In studying more detailed features within cyclones, satellite measurements have contributed to an understanding of dynamical processes. Rogers and Sherr (ref. 14), among others, used both Tiros

---

visual and window infrared data to study spiral bands. They concluded that the spiral structure is produced by horizontal advection that modifies cloud fields initially created by upward motions prominent in the early part of the storm's life. Emitted radiance in spectral intervals associated with water-vapor absorption has also been correlated with these motions (refs. 15 and 16). Imagery from both the 6.5- to 7.0- and 20.0- to 23.0-μm spectral bands often shows distinct patterns associated with mature cyclones. The most important feature is a tongue of relatively dry air that spirals into the center of the st

The importance of jetstreams in cyclone development is well known. Beran, Merritt, and Chang (ref. 17) studied Nimbus 2 imagery at 6.4 to 6.9 μm and indicated the relationships between the jetstream and relatively high equivalent blackbody temperatures (which correspond to a dry upper troposphere). They concluded that these regions are generally associated either with the area of maximum winds in the jetstream or with broad-scale subsidence over a large high-pressure region, and as a first approximation they felt that the shape of the regions could be used to separate the two conditions. The dynamics associated with the jetstream would normally be expected to produce elongated patterns related to the subsiding air found north of the core of an eastward flowing jet. Martin and Salomonson (ref. 18) verified these findings and also found that the radiation fields had some quantitative diagnostic value in the specification of the magnitude of the wind-speed maximum. Certain characteristic patterns in the visual imagery (refs. 6 and 7) are often used to fix jetstream positions with respect to extratropica storms. Thus, a combination of visible, infrared-window, and water-vapor absorption-band channels appeared to be a useful combination in the study of extratropical storms.

MEDIUM RESOLUTION INFRARED RADIOMETER

The MRIR sensor made simultaneous measurements in five regions of the electromagnetic spectrum, four of which were selected for this study. These are the reflectance channel (0.2 to 4.0 μm), infrared window (10 to 11 μm), and the two channels that are dominated by water-vapor absorption (6.5 to 7.0 and 20 to 23 μm) in the upper and middle troposphere, respectively, when clouds are absent. The first two channels have been used on both experimental and operational satellites; the last two have been flown on experimental satellites. Figure 1 gives weighting functions for the Nimbus 3 MRIR window and water-vapor channels. As can be seen in the figure, the greatest emission at midlatitudes and tropical latitudes for the two water-vapor channels comes from the upper and middle troposphere for the 6.5- to 7.0- and 20- to 23-μm channels, respectively. Thus, the two channels generally yield information on the distribution of water vapor in these portions of the atmosphere when no clouds are present (ref. 19). When high opaque clouds occur, the measurements approach those indicated by the window channel (ref. 20). Also, in relatively dry atmospheres (such as over Arctic regions), the emitted energy emanates principally from at or near the surface in the 20- to 23-μm region. Figure 1 also shows that, in the absence of clouds, the 10- to 11-μm window channel measures the emission from the surface and from the lower troposphere.

Because the individual channels are registered, the emitted energy for all channels comes from the same atmospheric column. The MRIR sensor also has a high signal-to-noise ratio; thus each measurement can be confidently interpreted. There are two important limitations in using the MRIR data. First, the MRIR instrument has a nominal angular field of view of 0.05 rad. From the altitude of the Nimbus 3 spacecraft (1100 km) this results in a nadir spatial resolution of around 55 km. This is rather crude when compared to the current series of operational satellites and it does impose a limit
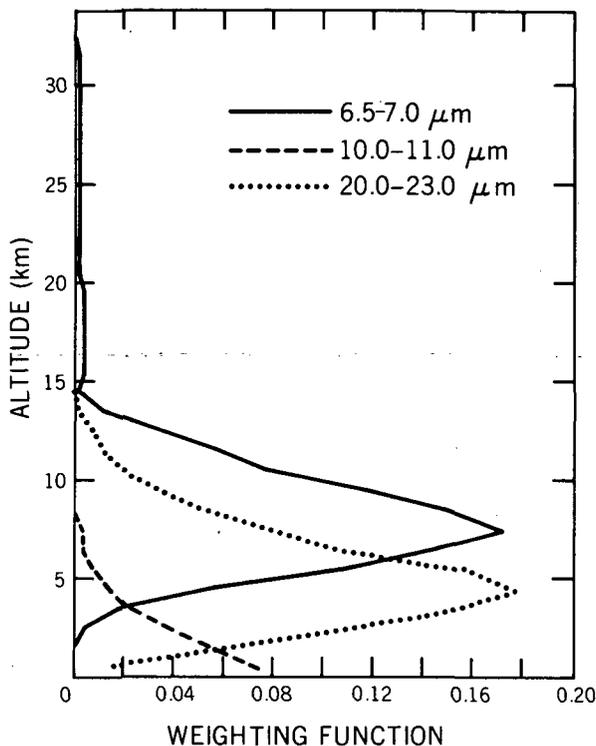
Figure 1.—Weighting functions (probability density functions) for three channels of the Nimbus 3 MRIR (units are w/cm^2 ster cm^{-1} km normalized to unity). Values are for midlatitude (45° N) with 2.644 precipitable cm H_2O.

on the size of meteorological features that can be successfully studied with the sensor. The scale of an extratropical storm is such that there is no difficulty in describing most of the major features with the MRIR sensor. However, small but sometimes important patterns such as cloud striations or shadow lines seen in good-quality, high-resolution visual data cannot be resolved with the MRIR. These are often present in large-scale cloud masses and frequently are used for positioning surface lows or locating jetstreams.

A second limitation is the 24-hr interval between radiation data observations. As a result it is probable that a number of short-lived features were not observed in this series. It is expected that the beginnings and ends of some major events also have been lost because of the time gap.

MRIR DATA REDUCTION

Reduction of the satellite data followed procedures described in the *Nimbus 3 Users' Guide* (ref. 21) with one exception. Limb-darkening corrections for the two water-vapor channels were empirical, based on the examination of some half-million radiation values.[1] The corrections were calculated at different time periods for both different latitude bands (0° to 80°) and different nadir angles (0° to 50°).

Because the reflected energy is dependent on several factors such as sun and viewing angles, it was not possible to directly compare reflectance values taken with a wide range of illumination conditions. To allow comparison, the reflectances were normalized with a method described in reference 21. The effective average radiant reflection $\bar{r}$ is defined by

$$\bar{r} = \frac{\pi \bar{N}}{\bar{H}* \cos \delta*}$$

where

$\delta*$ = solar zenith angle

---

[1]V. V. Salomonson, GSFC: personal communication, 1972.

$\overline{N}$ = effective upwelling radiance

$\overline{H}^*$ = effective solar constant

MAPPING PROCEDURES

The MRIR data were presented in the form of grid print maps. The value at each individual grid point was an average of all the radiance values closest to the geographical location of the point. With the 1:10 000 000 map scale used in this study (the grid spacing was 1.25° of latitude), usually 10 or more digitized measurements were located at each grid point, which further reduced effects of random noise. Errors in the geographical positioning of the satellite radiation data were not important, considering the synoptic scale of the features.

The map projection used for the grid print maps was especially developed for time-series work. As shown by Shenk et al. (ref. 22), the stereographic-horizon map projection allows the map to translate with the weather feature. Translation is done by allowing the pole of the projection to be placed at the same position relative to a moving feature so that the feature can be viewed with the same perspective throughout its lifetime. The feature used to fix the map projection center was the geographical location of the pressure center of the surface cyclone (indicated by a star on each map). Normalization of viewing perspective means that day-to-day comparisons of individual radiance maps can be made more easily. It also allows the construction of 24-hr difference maps showing the changes in radiances from one day to the next. These maps highlight the daily changes in each spectral band. It should be emphasized, however, that because the map projection moves, these products represent changes only in relation to one storm center. They cannot easily be used to record changes at a specific geographic point. Conventional surface charts prepared by the National Meteorological Center (NMC) are included for comparison with the MRIR maps.

Other products presented on the same map base as the radiance and difference maps are daily cloud decision maps. Here each grid point represents one of 10 decisions, nine of which indicate certain cloud regimes. The 10th case is where no clear cloud-type decision can be made. An automated decision matrix was established that employed the measurements from all four channels at each grid point. The decision criteria and the bases for their selection are given in appendix A.

All maps cited in this document (figs. 2 to 23) may be found at the end of the regular section of text.

DATA INTERPRETATION

Segments of three consecutive orbits were generally acquired to completely cover the storm system. Because of the period of the Nimbus 3 orbit, this required about a 4-hr collection period. Also, in areas of orbit overlap, radiation values nearly 2 hr apart are averaged at individual grid points. These temporal constraints, as well as the other limitations mentioned earlier, tend to set a lower limit as to the size and time scale of features that can be successfully studied. However, for the dimensions of an extratropical cyclone, these constraints can be largely neglected.

CASE SELECTION

Two important considerations were used for selecting the extratropical cyclone. The first, and most important, was good MRIR coverage during a significant portion of the storm's life cycle. The second was that, if possible, the storm should be fairly representative for the area where the case study would be performed. The example found essentially fulfilled both requirements.

The storm selected began as a weak low-pressure region (fig. 2(a)) over the Carolinas on April 29, 1969. It drifted slowly east-northeast with no significant changes in central pressure until May 1 (fig. 2(b)) when the first signs of deepening were recorded. The storm then followed the classical pattern of wave development and began tracking toward the northeast. Early on May 4 the storm reached its lowest central pressure and was located over the North Atlantic about 7° south of Greenland (fig. 2(c)). It had reached the mature occluded stage with the frontal system located well away from the low center.

From this point the synoptic situation (fig. 2(d)) became more complex as secondary development occurred and a new surge of colder air began moving around the original vortex. The degree of complexity is shown by the fact that secondary development took place in three different locations within a period of about 1 day while the original vortex was weakening. The original low had begun to fill and retrograde to the southwest by the end of May 4. This continued until May 6, where its remains were shown as a weak depression over Newfoundland.

The storm life cycle can be divided into two important phases. The first, April 29 to May 3, covered primarily the development and mature stages of the cyclone. The second, May 4 to May 6, included the development of secondary cyclones and the filling of the original storm. Both stages are common to extratropical storms that form along the east coast of the United States (refs. 23 and 24).

CASE STUDY

Phase I: Cyclone Development and Maturity

May 1—Weak Surface Depression

A prominent feature in the window and reflectance maps (figs. 3(a) and (b)) is an extensive region of clouds lying roughly along the 60° west longitude line. These clouds are thick and high, judging from the low window equivalent blackbody temperatures T_{bb} and high reflectance values. However, there are no distinctive frontal cloud bands and the MRIR data offer little indication of the position of the surface low.

The two water-vapor channels also indicate the good vertical development within the north-south mass of clouds as seen in the 6.5- to 7.0-μm channel measurements. These clouds are probably associated with overrunning and convective activity. There are some unexplained effects. For example, at points E, F, and G on figures 3(c) and (d), there are reversals in the T_{bb} values for the two water-vapor channels where the 20- to 23-μm values are lower than those for the 6.5- to 7.0-μm channel. Because

the emission sensed by the latter channel comes from a higher layer in the atmosphere, the normal situation is for the 6.5- to 7.0-μm T_{bb} values to be lower. This water-vapor temperature reversal (WVTR) effect, as it hereafter will be called, has also been noted in other examinations of Nimbus 3 MRIR data. Explanations for this feature range from calibration errors at lower temperatures for the MRIR instrument, to differences in cirrus emissivities.

Because high clouds do affect both water-vapor channels, the most independent information from these two channels should be found in the relatively dry regions to the west of the storm center. It has been shown that there is a correlation between the higher T_{bb} values in the water-vapor channels over such regions and subsidence (ref. 25). Using a 10-level numerical model, regions of downward vertical motions were successfully related to areas of relatively high T_{bb} values in Nimbus 3 MRIR water-vapor measurements. Thus, on figures 3(c) and (d), the region containing points A through D can be assumed to be subsidence associated with a trough line in the 50-kN-m^{-2} (500-mb) height field. As verified by the 1200 GMT 50-kN-m^{-2} (500-mb) analysis (fig. 4) the trough in this location also largely explains the orientation of north-south cloud mass. The clouds appear to be reflecting a region of positive vorticity that would normally be expected to the east of a sharp midtropospheric trough.

A band of even higher T_{bb} values (i.e., associated with drier air) is found from points A to B on the water-vapor channel maps (figs. 3(c) and (d)). The orientation of this band and its passage almost over the surface position for the low pressure center indicates that it is associated with the polar jetstream. Extrapolation of the most probable position of the jetstream from appropriate 30-kN-m^{-2} (300-mb) charts shows the jetstream maximum is located just east of the A to B line. Thus, for this day, the water-vapor imagery could be used to position the jetstream maxima over the eastern portion of the 50-kN-m^{-2} (500-mb) trough associated with the developing storm.

Another band of warmer T_{bb} values is located from points C to D. The values found in this area are comparable to those found in the first region, discussed previously. For this reason its zonal orientation and location to the south of the polar jetstream wind maximum might indicate that this band was reflecting the location of the subtropical jetstream. However, examination of both the 30- and 20-kN-m^{-2} (300- and 200-mb) charts revealed that at best only a weak wind maxima could be drawn through this region. A more likely explanation for this dry band will be presented later.

The patterns depicted by both water-vapor channels are very similar. Generally, one or the other could be used to place major features such as subsidence bands or jetstreams. However, there are some significant minor differences (e.g., the WVTR effect).

Equivalent blackbody temperature thresholds were established to delineate moist and dry regions on the 20- to 23- and 6.5- to 7.0-μm maps. On the 20- to 23-μm maps, T_{bb} values of 260 K were assumed to represent a dry atmosphere and of 240 K a moist atmosphere with middle and/or high clouds most likely present. For the 6.5- to 7.0-μm maps, the T_{bb} values were 240 and 230 K for dry and moist atmospheres, respectively. These selections were based on experience and radiative transfer calculations for a wide range of moisture conditions. On May 1, in the region near the line from A to B on figures 3(c) and (d), the 240-K line on the 6.5- to 7.0-μm map shows a definite crescent-shaped pattern that is not evident for the 260-K line on the 20- to 23-μm map. However, the shape of the areas within the 245- and 265-K values are similar. The discrepancy is believed to be due to the effects of the jetstream,

with perhaps the most structure evident on the 6.5- to 7.0-μm map. Because the 6.5- to 7.0-μm channel is an upper tropospheric measurement, the greater detail in this channel associated with the jetstream is not surprising.

The computer generated cloud-type decision map (fig. 5) indicates that the central cloud mass is composed of mainly midlevel clouds with varying amounts of cirrus or cirrostratus above. No areas of only cumulonimbus are indicated, but the resolution of the MRIR sensor and the map scale being used would tend to smooth out the very low window-temperature values found with this type of cloud. Also, the cloud decision map shows the location of cirrus above the main cloud mass. Cirrus can often be used to locate the point at which the jetstream moves across the main cloud mass.

Another feature that shows on the cloud decision map is a deck of cumulus and stratus clouds to the west of the surface low. This deck often forms as cold air moves over warmer water. In this case it would indicate cold air in the lower layers that is pushing southward behind the surface low. The clouds in this region also demonstrate the usefulness of the reflectance and window-data combination in cloud-type identification. With low clouds, the thermal contrast of the clouds and underlying surface is often not great enough to be easily distinguished with window-channel measurements. With these cloud conditions, a strong contrast exists in the reflectance values. The reverse occurs with large cloud-top height variability.

There are three distinct cloud masses at points B, C, and D in figure 5. These cloud masses become more important in the later days of the series. The larger mass (point B) is over the Gulf of Mexico and appears to be composed mainly of cirrostratus with some midlevel clouds below. The smaller masses are over the southeastern United States and the cloud decision map shows evidence of cirrus with the likelihood of some lower clouds. Surface data show a weak trough over the Gulf, with a suggestion of shortwave activity in the sparse upper-air data coverage over this area.

May 2—Young Occlusion

The extratropical cyclone had become more organized on the second day. This development is shown in the four channels of the MRIR data (figs. 6(a) to (d)). Once again the window and reflectance measurements indicate an area of intense cloudiness lying roughly along a north-south line. In this case, however, the southern portion is now elongated and it displays the cyclonic curvature commonly found in a cold- or occluded-front cloud band. A rough estimate for the position of the surface low can now be made by examination of the higher clouds. The surface wave is near the point at which the curvature of the rear edge of the higher clouds changes from concave in the frontal band to convex in the main cloud mass (ref. 7).

The position of the 50-kN-m^{-2} (500-mb) trough line can often be located by noting the point at which the high clouds along the cold front become suppressed. This weakening is associated with subsidence in the trough (ref. 7). Figure 6(a) indicates a break in the frontal cloud band near 20° N 70° W and this is associated with the southern portion of the trough. The water-vapor channels (figs. 6(c) and (d)) should reflect this subsidence. A weak warm area is found in and just to the north of the region where the frontal cloud band was suppressed. The highest T_{bb} values (i.e., greatest subsidence) are now roughly bounded on the poleward side by 35° N. A comparison of the flow in this region with earlier results shows that it has become more zonal. Therefore, the trough has become

7

broader, with the sharpest curvature now poleward of 35° N. This description is verified by figure 7.

Two still higher T_{bb} bands are again noted in the broad subsidence region associated with the trough. The band lying between points A and B would seem to be associated once more with the polar jet. However, it is now not as well defined on either of the two maps (figs. 6(c) and (d)) as was the band found in this same position with respect to the surface low on May 1. This would suggest a weakening of the winds in this area. Extrapolation of the jetstream position from upper-air data shows that the winds in the region from A to B are now about 23 m s^{-1} (45 knots), weaker than the winds found in the same relative position on the previous day. Moreover, the strongest winds are now indicated at the base of the trough. The only important change in the water-vapor data that might be linked to this shift in location of the jetstream wind maximum is found on the western portion of the zonal band of higher T_{bb} values associated with subsidence in the trough. A definite curved pattern at point E is now found on both maps as opposed to the lack of any specific pattern in this region on the 20- to 23-μm map for May 1.

The dry band from C to D is still present and now is 5° south of its former location with respect to the position of the surface low. It contains higher T_{bb} values than are found in the A to B band. The orientation of this feature and its relation with respect to the polar jet location might suggest then that it was similarly related to the position of a subtropical jet. However, as stated in the discussion for May 1, there appears to be a more probable explanation. The 50-kN-m^{-2} (500-mb) analysis shows that a cutoff low has formed over the Florida Panhandle. Anticyclonically curved cirrus with a well-defined poleward edge were observed in conjunction with the closed low in the IDCS data. This cirrus pattern is similar to that found where a jet moves across an extratropical storm; it is instead in an area of weak, high-level (300-mb) winds. Thus, it appears that subsidence associated with the anticyclone north of the cutoff low can produce features similar to those associated with wind maxima. However, in contrast to the patterns that are seen with jetstreams, the area within the 265-K isotherm on the 20- to 23-μm map is much greater than the area within the 245-K isotherm on the 6.5- to 7.0-μm map. The warm tongue on the 20- to 23-μm map would then appear to be related to strong midlevel subsidence and would be important in recognizing this situation. Therefore, the positioning of jetstreams through the use of warm bands, or tongues, in the water-vapor measurements should be done with caution in the vicinity of cutoff lows.

Figure 8 shows the cloud-type decision map for May 2, indicating multilayer clouds with patches of either cumulonimbus or dense cirrostratus near the cyclone center and frontal bands. Points A, B, and C, which are in areas of the most intense cloud activity, again correspond to points where the WVTR is noted. An anticyclonically curved band of cirrus once more locates the most probable point at which the polar jet begins to recurve southward across the cyclone. The stratus and cumulus deck to the west of the surface low is also still in evidence. A single region of mid-level and cirrus clouds is located to the southwest of the map center (point A). As mentioned earlier, this is in the vicinity of a cutoff low aloft and the cloud consolidation probably indicates some improved organization of the vertical motion field associated with this feature. A new cloud

band is seen to the west of the cyclone center. This band is associated with a new surge of cold air that is moving eastward across Canada.

With time continuity, another analysis product available is the 24-hr difference map (figs. 9(a) to (d)). Whereas the difference maps provide the same information as that obtainable by comparing individual maps for each observation, mental storage of the measurements for all four MRIR channels for each day would be a nearly impossible task. To construct the difference maps, the radiation fields for May 1 have been subtracted from those of May 2. The window and reflectance difference values, for example, show the development of the frontal bands as well as the changes in the organization of the clouds about the storm center. The water-vapor difference measurements described change in the orientation of the region of warmest temperatures to the west of the low center, which shows clearly how the flow has become more zonal.

May 3—Mature Occlusion

One of the prominent features in the window and reflectance data (figs. 10(a) and (b)) is that the frontal cloud band has now moved away from the storm center. Two areas of rather intense cloud activity also are indicated at points A and B. The clouds at both points tend to bulge into the cold air behind the front and thus give an indication of the presence of minor waves. On the previous day the window-data map revealed two similar active cloudiness regions in the same positions relative to the storm center, but on that day they did not exhibit any unusual degree of development. Ship reports also indicated precipitation in these two areas for both days. The suspicion of wave formation is satisfied in part by the 1800 GMT surface analysis that indicates point A as being a new center of low-pressure development. There is no evidence of a new cyclone at point B on the 1800 GMT map, but there is little surface data, and so there could be minor and perhaps transient cyclogenesis at this point. The cloud mass associated with the cutoff low to the west of the map center is still in evidence, and the clouds have merged with those associated with the cold front.

The water-vapor measurements (figs. 10(c) and (d)) suggest that the older the vortex, the less information on polar jetstream position in its vicinity can be deduced from the locations of bands or tongues of highest T_{bb} values. Two such tongues from points A to B and C to D stand out in a broad region of relatively high temperatures. But an examination of standard upper level maps shows that the probable positions of the jetstream wind maxima disagree with the locations of the warm tongues. Another possible explanation for the subsidence in the region from A to B would be the development of a sharp ridge forming between the major low and a new trough overtaking it from the west. Evidence of this ridge formation is seen in the 20- to 23-μm data, where a more prominent pattern in the higher T_{bb} values occurred (point A) than was present on the 6.5- to 7.0-μm map. The high T_{bb} region around C once more seems to be related to the anticyclone north of the cutoff low. East of the C area, the subsidence along the original 50-kN-m^{-2} (500-mb) trough line has become more evident.

The cloud-type decision map (fig. 11) shows again the intense activity on the cold front that was thought to be associated with minor waves. Similar activity is noted on the frontal band still moving eastward from its previous position over Canada. Two examples of a WVTR are found and these are associated with the suspected wave (points A and B) on the southern portion of the cold front.

Elsewhere, low decks of stratus and cumulus are now indicated in the cold air behind both the major and secondary frontal bands. Both frontal systems also exhibit bends in the higher clouds, which roughly mark the triple points. On the assumption that the jetstream passes over the triple points, these bends can be used to give two points for the location of the jetstream. Using these points and the position of the northernmost wave on the cold front, one can then draw a cyclonically curved wind maximum through this region that is a better estimate of the real location of the jetstream than would be obtained only from the water-vapor measurements. The high T_{bb} values at point B on the 6.5- to 7.0-μm map would also support a jetstream crossing at this point.

Phase II: Secondary Development and Dissipation of Original Cyclone

May 4—Old Occlusion

The window measurements (fig. 12(a)) reveal a number of interesting changes. The first is the continued eastward advance of the secondary frontal system as opposed to the movement of the primary low, which is now almost stationary (fig. 13). The most intense cloud development associated with this feature is directly south of the main vortex center. The appearance of this cloud field, which is comma shaped (point A of fig. 12(a)), and its movement suggest that it was associated with a short wave feature. Reintensification within the general circulation of the main cyclone is also noted. The window-channel T_{bb} values have dropped significantly over the map center. Such a drop indicates much higher clouds over this region as opposed to the cumulus and stratus field noted there on the previous day.

Like the short wave feature, eastward movement has also occurred for the cloud shield associated with the cutoff low. This movement is about 10° of latitude relative to the principal cyclone center and suggests that the anticyclone north of the cutoff low is weakening. The original frontal band has shown similar movement and in addition there still is a bend that approximately coincides with the location of the triple point. No indication is given on the window or other radiation maps that could be used to position either of the two low centers now being analyzed in the circulation of the original vortex, as was the case on May 1.

The reflectance and water-vapor maps (figs. 12(b) to (d)) once more indicate a pattern for the more intense cloud activity matching that shown by the window data. On the water-vapor maps, a broad band of subsiding air can now be tracked from points A through F. The area from A to B represents the now familiar subsidence band, which has weakened slightly, to the north of the clouds that were first attributed to the cutoff low. The even higher T_{bb} values from C to D suggest that the remains of the subsidence associated with the original 50-kN-m^{-2} (500-mb) trough can still be found in this region. The 50-kN-m^{-2} (500-mb) analysis shows little indication of it, possibly the result of limited data. The final region from E to F again appears to be the result of ridging just to the east of the area, which is being formed as the short wave moves around the major low. From A to F the whole-band outlines a relatively cloud-free area that spirals into the storm center. Such large cloud-free bands are generally a prominent feature of mature extratropical storms.

Positions for maximum wind locations are again not possible in the subsidence band (from A to F) just discussed. There is a second band north and parallel to it. This region (from G to I) is unique

in that it is most prominent in the 6.5- to 7.0-μm data and is associated with a comma-shaped cloud mass which was assumed to be a reflection of positive vorticity advection in conjunction with a short-wave trough. From experience in the interpretation of visible data it has been established that the jet-stream should be shown moving through a shortwave feature traveling around a larger vortex (ref. 7). The orientation of the high T_{bb} tongue from G to I suggests an association with the polar jetstream. Using this tongue and an approximate triple-point position, one can estimate an almost west-to-east flow for the jetstream on this day. The 30-kN-m^{-2} (300-mb) maps about 12 hr before and after the satellite pass show that the jetstream has become almost zonal to the south of the center of the surface low.

Layers of cirrus and midlevel clouds dominate the region along the occlusion and westward through the low center (fig. 14). Of equal interest is the location of two regions of either cirrostratus or cumulonimbus clouds within this band. These represent the increased activity over the old vortex center and the normal activity usually encountered at the triple point of an occlusion. Intense activity is also shown for the cloud shield that has been associated with the cutoff low. There has been a significant change in cloud-top height from the previous day that may indicate an increase in upward vertical motion in this region (refs. 26 and 27). One example of the WVTR is found at this point; and finally, the large well-defined stratus and cumulus deck behind the original cold front is not as extensive as before, which probably signifies some modification of the air mass.

A wide variety of cloud types is found at point A associated with the secondary frontal system. First, a region of midlevel and cirrus clouds is indicated along the frontal band. To the northwest, the cirrus is not present and midlevel clouds predominate. Further northwest, only lower clouds in the form of stratus and cumulus are present. A clear area is also indicated in this region. The chaotic nature of the transition between the higher and lower clouds at some points is also shown by the no-decision band. The cloud decisions around point A reflect the same transitions of cloud topography found in the much larger frontal band that dominates the southern portion of the radiation maps.

May 5—Frontless Vortex

The patterns depicted in the radiation maps have become so complex by this time that con-tinuity contributes substantially to the interpretation. Secondary cyclones (fig. 15) have developed at the triple point of the original frontal system and adjacent to the original vortex at the northern end of the occlusion. In addition, the secondary surge of cold air has pushed well to the east and south of the map center. This has resulted in a parallel set of frontal systems stretching east-west across the Atlantic.

Surface reports now indicate precipitation in the cloud mass at the trailing edge of the original frontal band. This region has been tracked since May 1, and the radiation maps 24 hr previously had suggested increased development. The surface analysis for 0000 GMT on May 5 accounted for a growing number of precipitation reports by indicating an inverted trough line in the easterly surface flow over this region. The same feature is carried on figure 15 6 hr later and it implies a westward movement to the cloud shield in this area. A closed low (fig. 2(d)) is then analyzed on the surface map at 1200 GMT. However, there appears to have been an indication of a closed surface circulation

at roughly 25° N 77° W as early as 1200 GMT on May 4 (fig. 13). Based on this and the eastward movement of the cloud field indicated by the satellite data, it suggests that the cyclogenesis was initiated by the 50-kN-m^{-2} (500-mb) cyclonic circulation that has moved eastward and is now in juxta-position with the new closed circulation at the surface.

The reflectance map (fig. 16(b)) gives the best view of the frontal system cloudiness for this day and shows a minor wave at 34° N 40° W. Because of the apparent low cloud-top heights, there is reduced thermal contrast that does not permit identification of the wave structure. Intense activity outlined by the lowest T_{bb} values (fig. 16(a)) is now found in four regions. One area is located in a band just to the west of the old vortex (point A) and another is along a segment of the secondary cold front (point B). Good vertical cloud development is indicated in association with the secondary cyclone at the old triple point (point C) and in the cloud shield at the western tip of the original front (point D). Of the four cloud regions mentioned above, the activity at points B and D is especially noteworthy. The cloud shield has once more moved about 10° east with respect to the map center. The weakening cutoff low is moving at about the same rate as the associated cloud shield. Troughing associated with this feature is depicted by the north-south orientation of the low T_{bb} values from points D to E.

At point B, development associated with the secondary system has maintained a comma shape and moved eastward to a position that is very close to the cloud band associated with the original occlusion. If it should merge with the original occlusion cloud band, it might be expected to cause some reintensification along the band.

A segment of the polar jetstream is once more detectable on the two water-vapor channel maps (figs. 16(c) and (d)). As was the case on May 4, a high T_{bb} band from A to C is concomitant with the most intense activity associated with the short wave to the south of C. The band of higher T_{bb} values also has a broad curvature on both maps and its base is oriented toward the vicinity of the remains of the cutoff low. This indicates broad 50-kN-m^{-2} (500-mb) troughing along the east coast of the United States, which is consistent with the 1200 GMT 50-kN-m^{-2} (500-mb) analysis (fig. 17). Placement of the polar jetstream along the tongue from A to C would then appear to be reasonable.

The second T_{bb} band from D to E is broader on the 20- to 23-μm map than on the 6.5- to 7.0-μm chart. Using this feature and continuity, one would again dissociate this band from a wind maximum. The highest T_{bb} values found at point D appear to locate the weak but persistent original 50-kN-m^{-2} (500-mb) trough. This conclusion is reached because the 24-hr movement of this point from the location assigned it on the previous day is consistent with other movements in this area. This trough provides some support for a minor wave on the front at point D on figure 16(a). Eastward from point D toward E, the difference between the 260-K isotherm pattern on the 20- to 23-μm map and the 240-K isotherm pattern on the 6.5- to 7.0-μm map becomes even more noticeable. The 260-K band is now much broader than the corresponding 240-K pattern. A study of the midtropospheric winds for this area showed that the winds were parallel to the D to E line. Once established, a region of relatively dry air can be persistent; thus the band from D to E seems to be best explained by advection over this region. The zonal midtropospheric winds appear to be advecting relatively dry air downstream from its source at point D.

The cloud decisions made on figure 18 do not yield a good picture of the cloud patterns associated with the complex synoptic situation. The only points of reference that readily appear are in the

four areas of greatest cloud activity mentioned earlier (points *A, B, C,* and *D* on figs. 16(a) and (b)). For example, a large region of cumulonimbus or cirrostratus is indicated to the south of the map center. With these exceptions, however, vast no-decision areas are prevalent. Because the original vortex and frontal bands are weakening, increased difficulty in making cloud decisions would be expected. Knowledge of the synoptic history can be used to give at least a general appraisal of the cloud conditions occurring over the no-decision areas.

May 6—Filling Vortex

The MRIR data for the last day in the series reflect vast changes that have occurred in the previous 24 hr. They are of such degree that perhaps the clearest way to present them is to start with a discussion of the difference maps (fig. 19). The window data (fig. 19(a)) show the development of a large wave-shaped cloud mass to the southeast of the old vortex center. Judging only from the radiation maps for the previous day, it would appear that the cloud shield once associated with the cutoff low has moved some 2200 km (1200 n. mi.) to the northeast. This would require a speed of about 26 m s^{-1} (50 knots), which is extremely fast. The surface maps 12 and 6 hr before the 1200 GMT, May 6 map (fig. 20) do not indicate rapid movement of the low first analyzed in this area on May 5. Rather, they indicate new development some 10° to the northeast of it. If this assumption is correct, the region from points *A* to *B* on figure 19(a) could be related to the area from *D* to *E* on figure 16(a). The result translates into an eastward movement of some 5° for the original cloud mass in this area, which is more consistent with previous movements. Thus, it appears that the movement of the trough related to the filling of the cutoff low has spawned a new wave as it moved across the two weak frontal bands in the area. The 1200 GMT, May 6 50-kN-m^{-2} (500-mb) chart (fig. 21) shows the extensive trough that now exists to the west of this development. Satellite data taken at shorter intervals would have been extremely useful in this situation.

The reflectance difference map (fig. 19(b)) shows decreased reflectances over the area of the original vortex. Window T_{bb} values at both times were high and the changes were not significant, which indicates that low clouds in this area have become more scattered. The decrease in cloudiness beneath the new 50-kN-m^{-2} (500-mb) trough is also shown in the reflectance and window differences. Such a decrease results in a distinct warming trend in water-vapor T_{bb} values, also indicated on their difference maps (figs. 19(c) and (d)).

The window temperature map (fig. 22(a)) shows four distinct active cloud regions (points *A* to *D*). These regions correspond well to the areas of cyclonic circulation indicated by surface analysis. The satellite data allow an accurate appraisal of the cloud growth and development in these regions. Point *A* locates the new development; its rapid growth in less than 24 hr is indicated in the pattern for the lowest T_{bb} values. A small hook pattern indicates the early stages of occlusion. Points *B* and *C,* as suggested by the difference map (fig. 19(a)), appear to be the same cloud masses that were labeled *D* and *E,* respectively, on the previous window-channel map. The fourth area (point *D*) was not shown on the May 5 window map because it was located to the south of the map boundary. As verified by IDCS data, a small active cloud region existed near the present position of point *D.* Thus, 24-hr continuity can be found for points *B* to *D.* However, this continuity is nearly impossible using

the surface analyses. The T_{bb} values recorded at points A and D (fig. 22(a)) also indicate a much greater degree of cloud activity than would be suggested by the two weak regions of cyclonic circulation indicated at these points on a surface map (fig. 20).

The window difference maps indicate that there has been substantial clearing in the region under the 50-kN-m^{-2} (500-mb) trough. The possible development of subsidence in this region is reinforced by the reflectance map (fig. 22(b)), which now shows a large number of values characteristic of ocean surface reflectances. The presence of subsidence should be confirmed in the water-vapor measurements (figs. 22(c) and (d)) and a broad region of high T_{bb} values are found on both maps. A crescent-shaped tongue of high T_{bb} values is found on the northern boundary of the broad subsidence region (points A to C). Its curvature is related to the curvature of the 50-kN-m^{-2} (500-mb) trough in this area. Because of its location in the trough and the equal definition of the pattern on both maps, the tongue apparently is related to the polar jetstream. The jetstream appears to be associated with the hook pattern at point D. This pattern is characteristic of the anticyclonic curvature on the northern edge of cirrus masses moving equatorward on the downstream side of an extratropical storm. Using the dry tongue and the northernmost part of the wave pattern at point A on figure 22(a), the position of the jetstream can be drawn from about 30° to 75°W. The 30-kN-m^{-2} (300-mb) map reveals good agreement between the satellite and conventional-data positions for the jetstream. Recalling the success in locating the jetstream on May 1 by similar methods, it has been found that the jetstream positions could be located with the most success over newly developed extratropical cyclones with the water-vapor and cloud-type data.

Several different areas now exhibit WVTR's. Reversals occur at three points (A, B, and D on fig. 22(a)) of the four areas of most intense activity noted in the general wave-shaped cloud pattern. For the 6-day series, it is interesting to note that, as on May 6, the greatest number of reversals are found in areas of new cloud development. As the features age, the reversal decreases or ceases to exist. With one exception in this limited sample, the WVTR effect was always noted south of 35° N. An examination of other data revealed that the WVTR is also found with nighttime data, which would eliminate any explanation related to reflected solar radiation.

A final point of interest on the two water-vapor maps is the crescent-shaped subsidence band attributed to the jetstream. The warmest values are found on the western wing of the trough on the 20- to 23-μm map and on the eastern side of the 6.5- to 7.0-μm map. An explanation may be that the slope of the jetstream is such that maximum winds are farther east at the higher level.

The cloud decision map (fig. 23) indicates large areas of clear skies or small areas of cumulus southwest of the old vortex. Over the vortex are disorganized areas of cirrus and cumulus clouds. The greatest vertical development is over the region of new wave development. A measure of the extent of this development is given by the large region designated as being covered by either cirrostratus or cumulonimbus clouds.

CONCLUSIONS

The extratropical cyclone examined in this 6-day series followed the classical Norwegian model. The value of the satellite in making these observations is that the vantage point from space far above

the cyclone can determine large-scale spatial and temporal changes that occurred in the cloud and moisture fields. As important as is knowledge of the general evolution of a storm, equal significance should be given to the detection of shortwave features and other minor perturbations within the storm circulation. A number of these were seen to modify the day-to-day structure of the cyclone. Yet, because of their relatively small size, they were often missed by the standard observing network. Examples of some of these were the minor perturbations noted on the frontal bands and the clouds associated with vorticity advection, which moved around the original vortex. The satellite observations allowed some estimate to be made for movement and changes in intensity of most of these features and offered a basis for estimates of future modifications in the general cloud patterns. Finer detail on a shorter time scale would have been helpful in making better estimates for the movement and development of these small-scale features. More frequent observations will be available in the future from a geosynchronous satellite platform.

A multispectral view of the meteorological features offered some unique advantages. Cases were found, for example, where the reflectance and window channels complemented one another. Often, with low cloud fields the thermal contrast between cloud and ground was small. However, good contrast in reflectance values could be used to delineate the cloud field. Also, the difference maps showed that variations in reflectance values appeared to be related to the dissipation or development of low clouds where the cloud decision map provided information on cloud type. However, cloud height differentiation with solid layers of clouds at different heights was done more easily with the window data in conjunction with the reflectance data. Together they offered a better daytime cloud-discrimination capability than was available with either alone. When these channels were used with the water-vapor measurements, which were affected by upper level and midlevel moisture and cloudiness, the result was an automated cloud decision map.

The 20- to 23- and 6.5- to 7.0-μm channels were often useful in positioning the jetstream, with perhaps the most distinctive features being found on the 6.5- to 7.0-μm map. However, there were some problems. Cutoff lows, for example, produced a pattern of dry air quite similar to that produced by a jetstream. Advection could cause an elongated region of warmer values. Cirrostratus canopies associated with the cyclone also served to mask the location of the jetstream. Still, continuity and the locations of other features such as frontal triple points could be used to prevent misinterpretation.

The water-vapor channels used together also offered other interesting possibilities. The reversal in the magnitudes of the temperatures occasionally recorded by the two in active cloud regions deserves further investigation. In the cloud-free regions, the ability to make some vertical separation of water-vapor patterns was useful in determining the existence of wind maxima at different levels. An example is the possible indication of a vertical variation in the axis of the polar jetstream on May 6. Thus, as for the window and reflectance channels, there appear to be occasions when the two channels complement one another.

The usefulness of multispectral viewing of a meteorological feature such as a cyclone depend on both the user's needs and on further confirmation of the validity of some of the observations made in this paper. However, the value of an instrument that could make measurements simultaneously in the 0.2- to 4.0-, 6.5- to 7.0-, and 10- to 11-μm spectral intervals with spatial and spectral resolution

approaching that found in current operational satellites would appear to be high. Combined with a geostationary platform, such an instrument would lead to improved understanding of many meteorological features and processes.
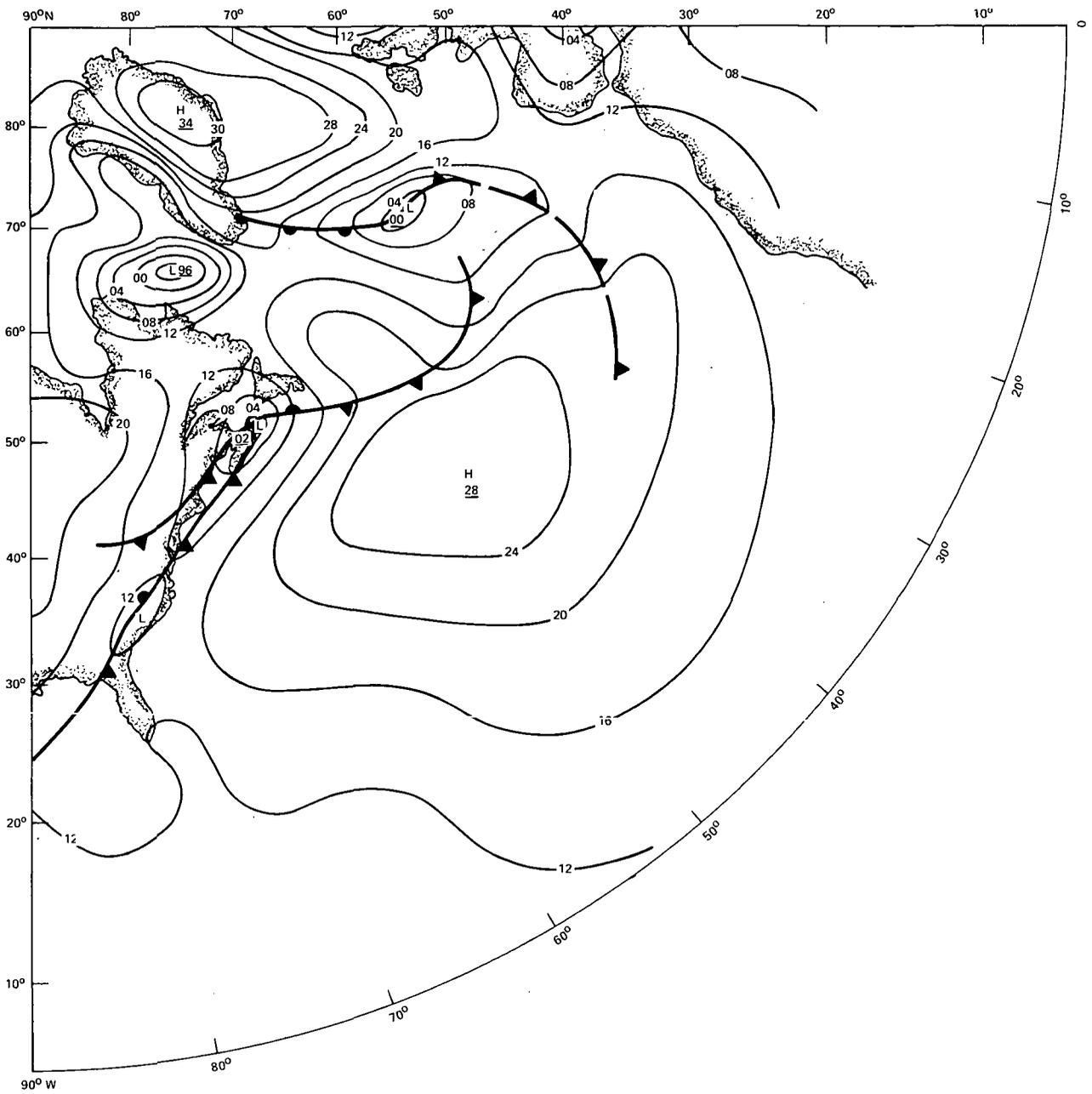
Figure 2.—NMC surface charts. (a) 1200 GMT Apr. 29, 1969. Units are in 10^2 N m^{-2} (millibars).

17
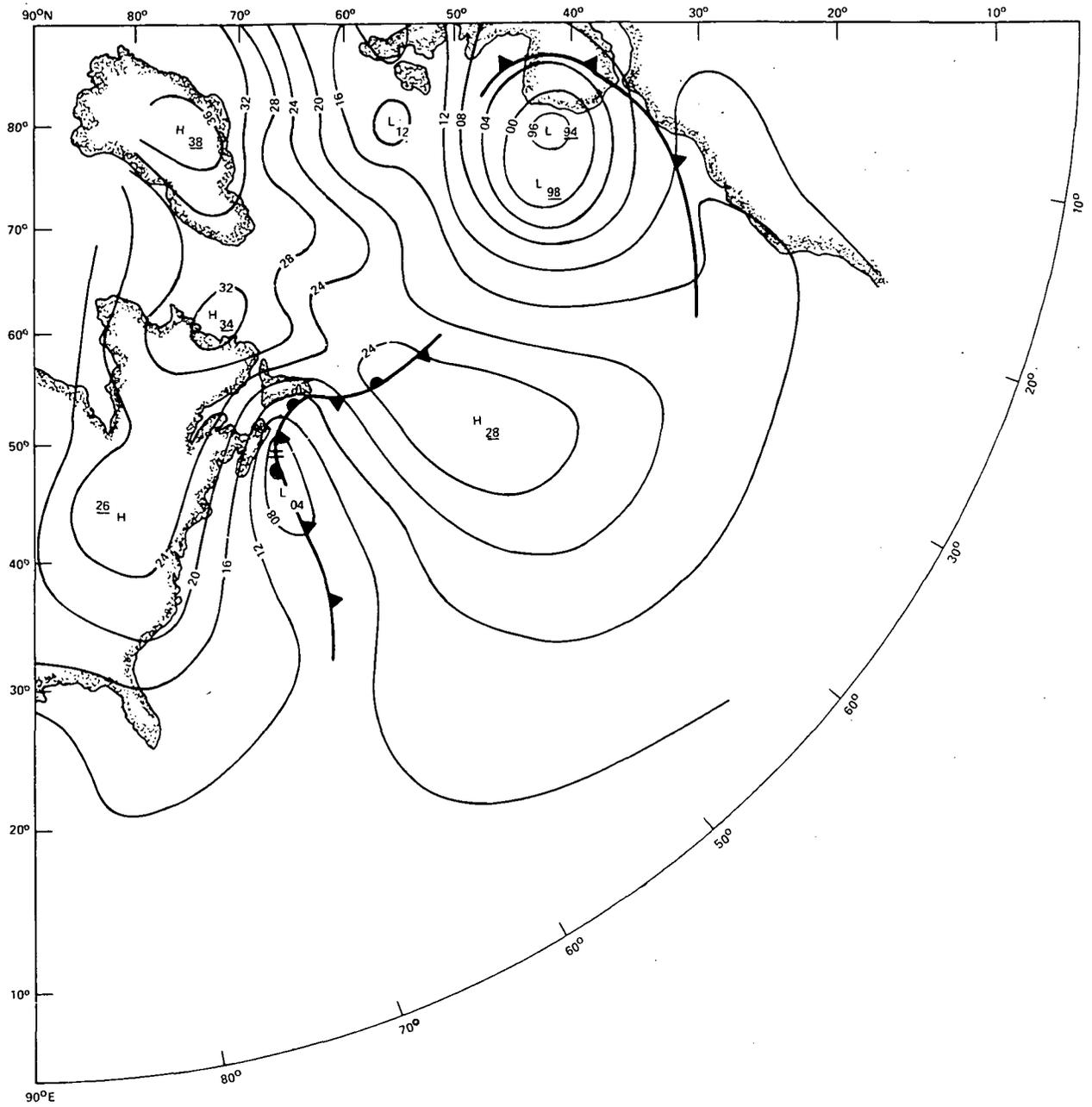
Figure 2 (continued).—NMC surface charts. (b) 1200 GMT May 1, 1969. Units are in 10^2 N m^{-2} (millibars).

18
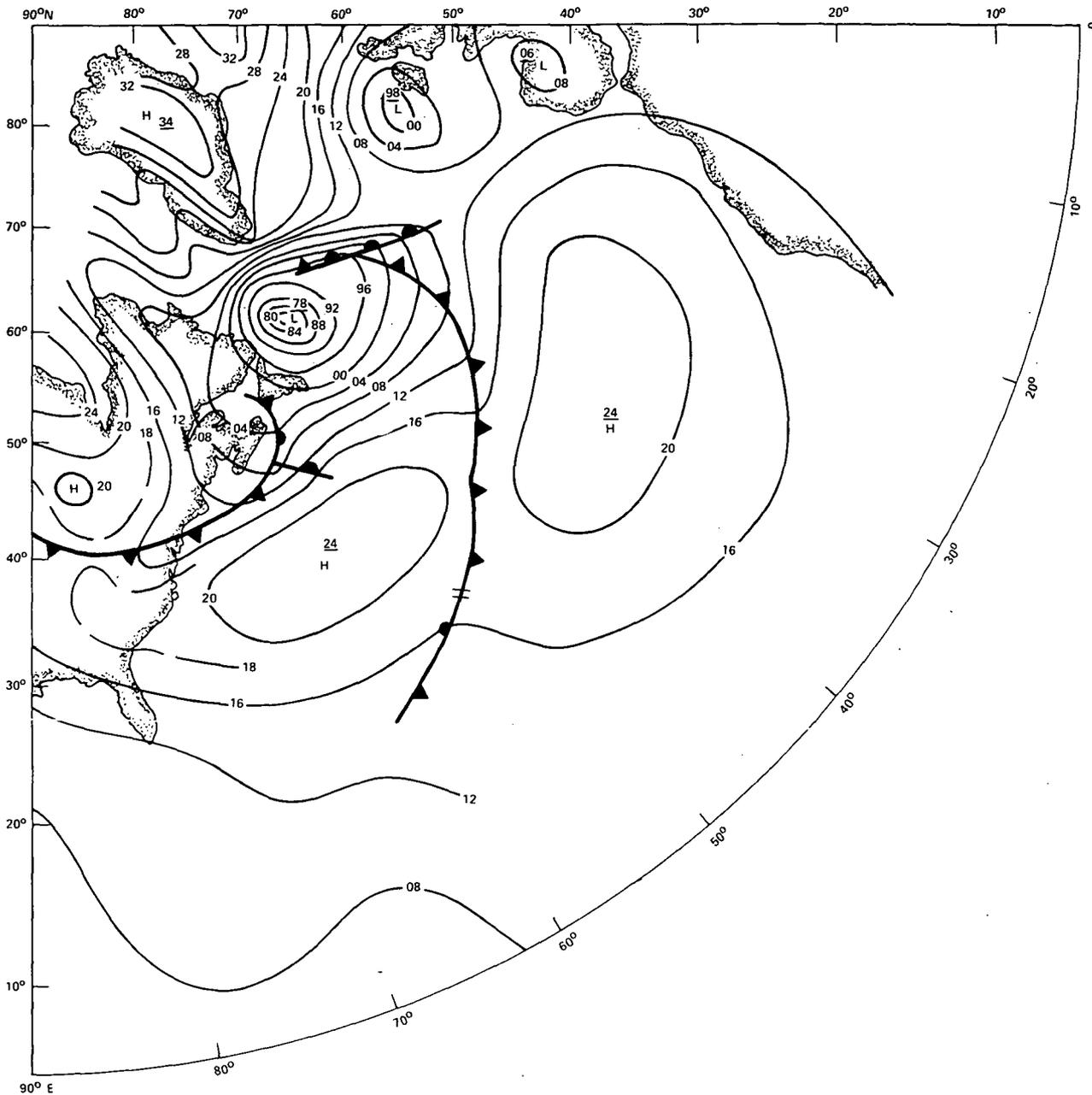
Figure 2 (continued).—(c) 0600 GMT May 4, 1969. Units are in 10^2 N m^{-2} (millibars).

Figure 2 (concluded).—NMC surface charts. (d) 1200 GMT May 5, 1969. Units are in 10^2 N m^{-2} (millibars).

Figure 3.—Radiation maps for May 1, 1969. (a) 10- to 11-μm. Isotherms are in °Kelvin.
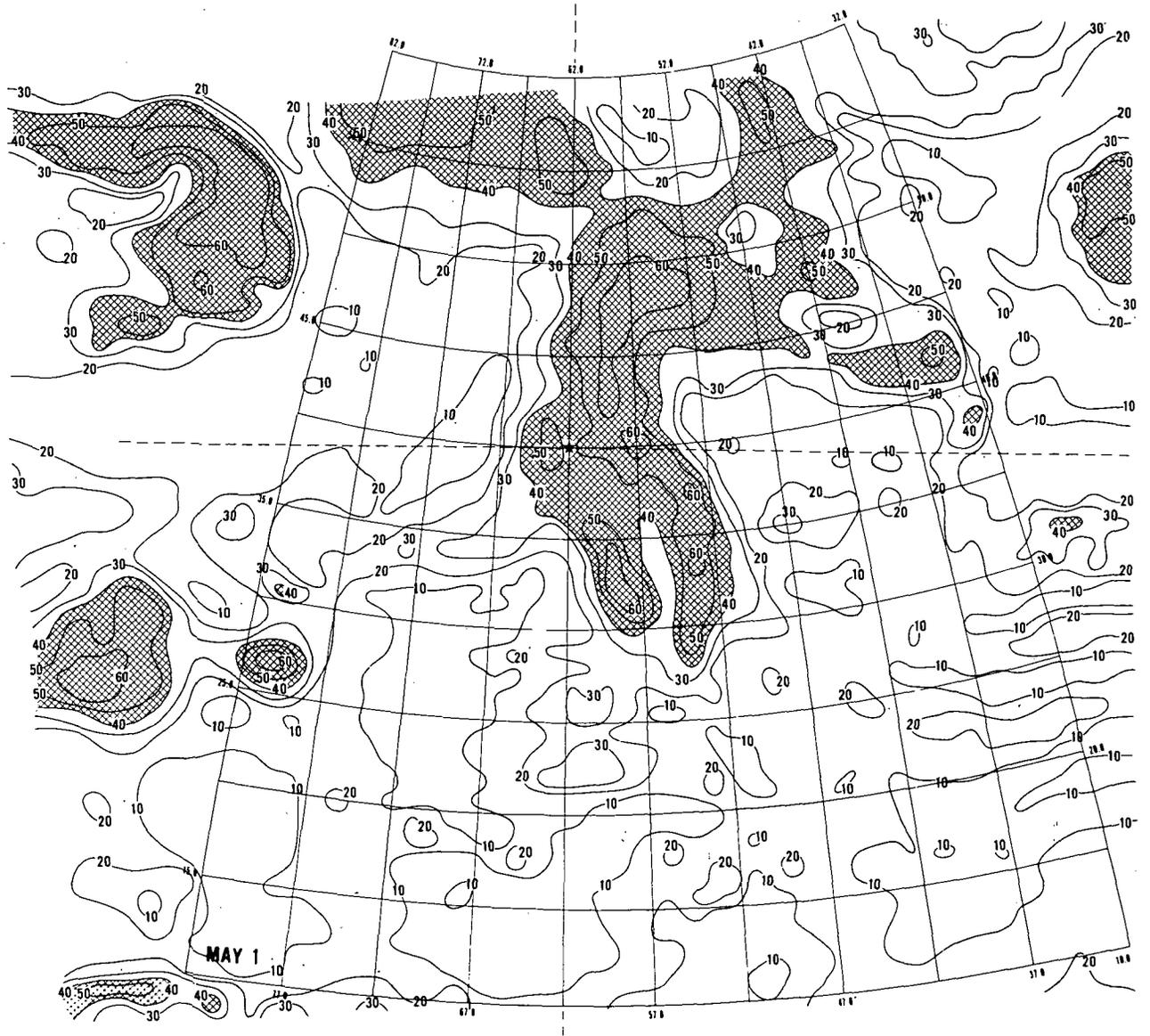
Figure 3 (continued).—Radiation maps for May 1, 1969. (b) 0.2- to 4.0-μm.   Isolines are normalized reflectances in percent.

22
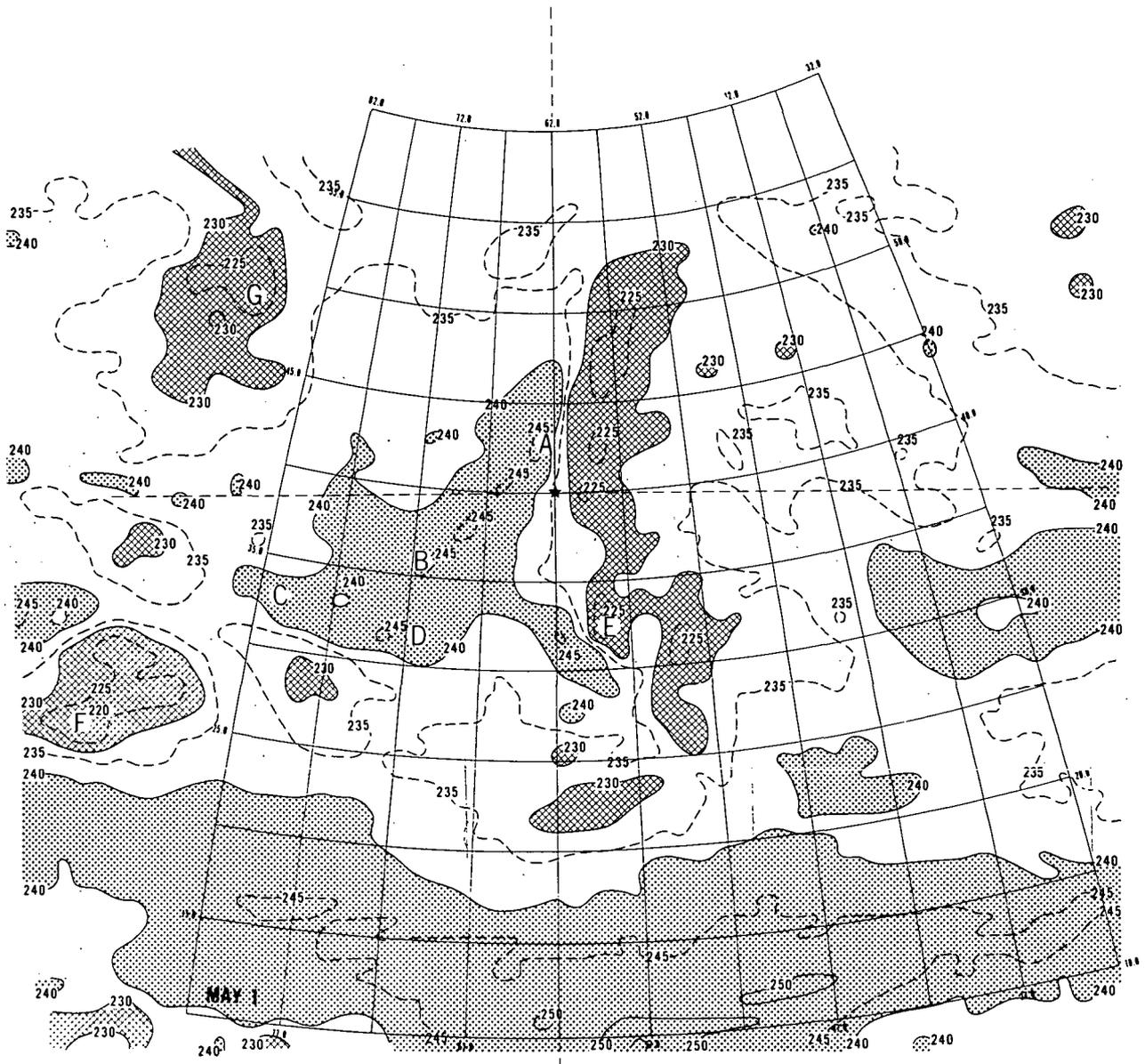
Figure 3 (continued).—Radiation maps for May 1, 1969. (c) 6.5- to 7.0-μm.   Isotherms are in °Kelvin.

23
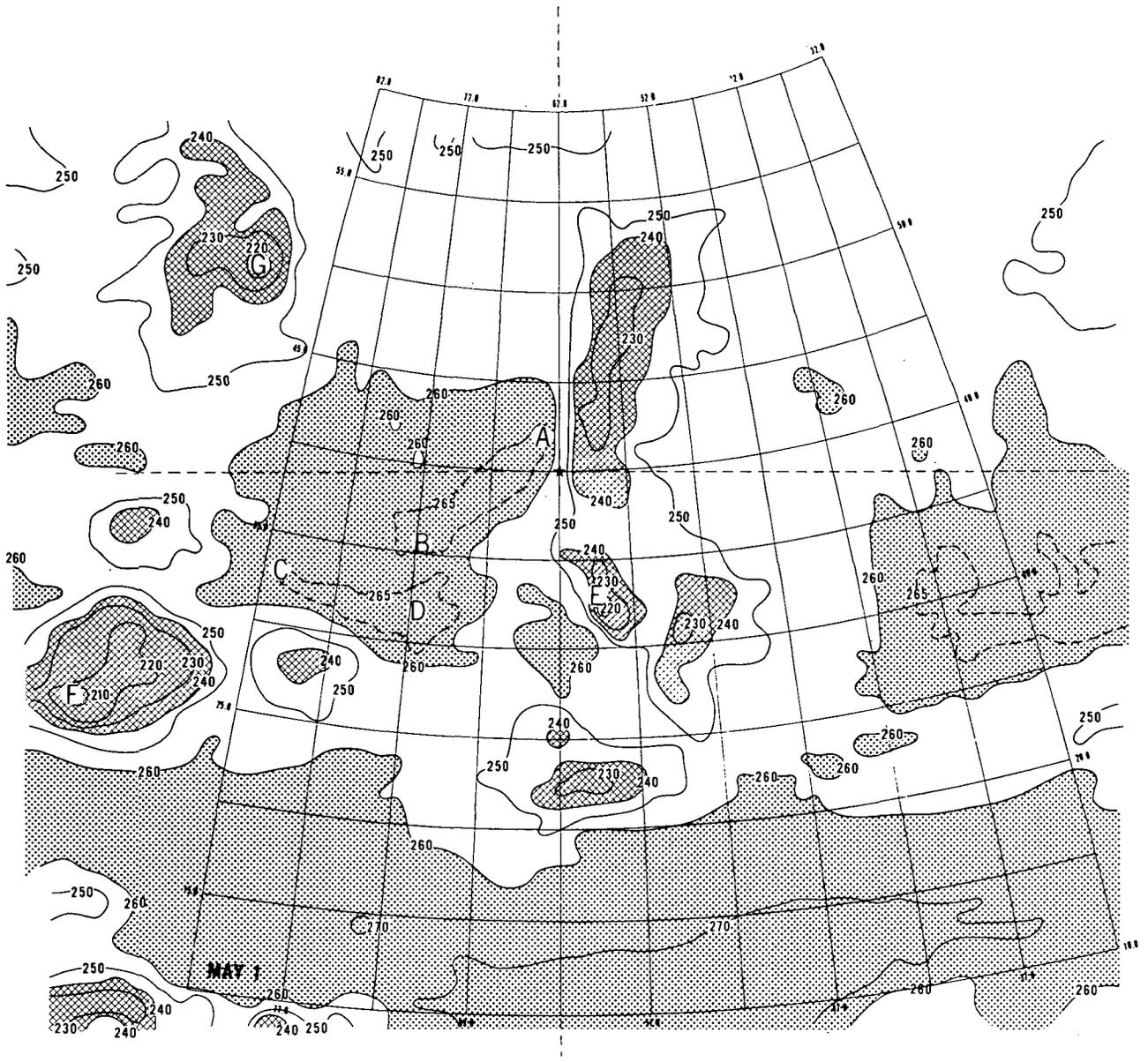
Figure 3 (concluded).—Radiation maps for May 1, 1969. (d) 20- to 23-μm.   Isotherms are in $^\circ$Kelvin.
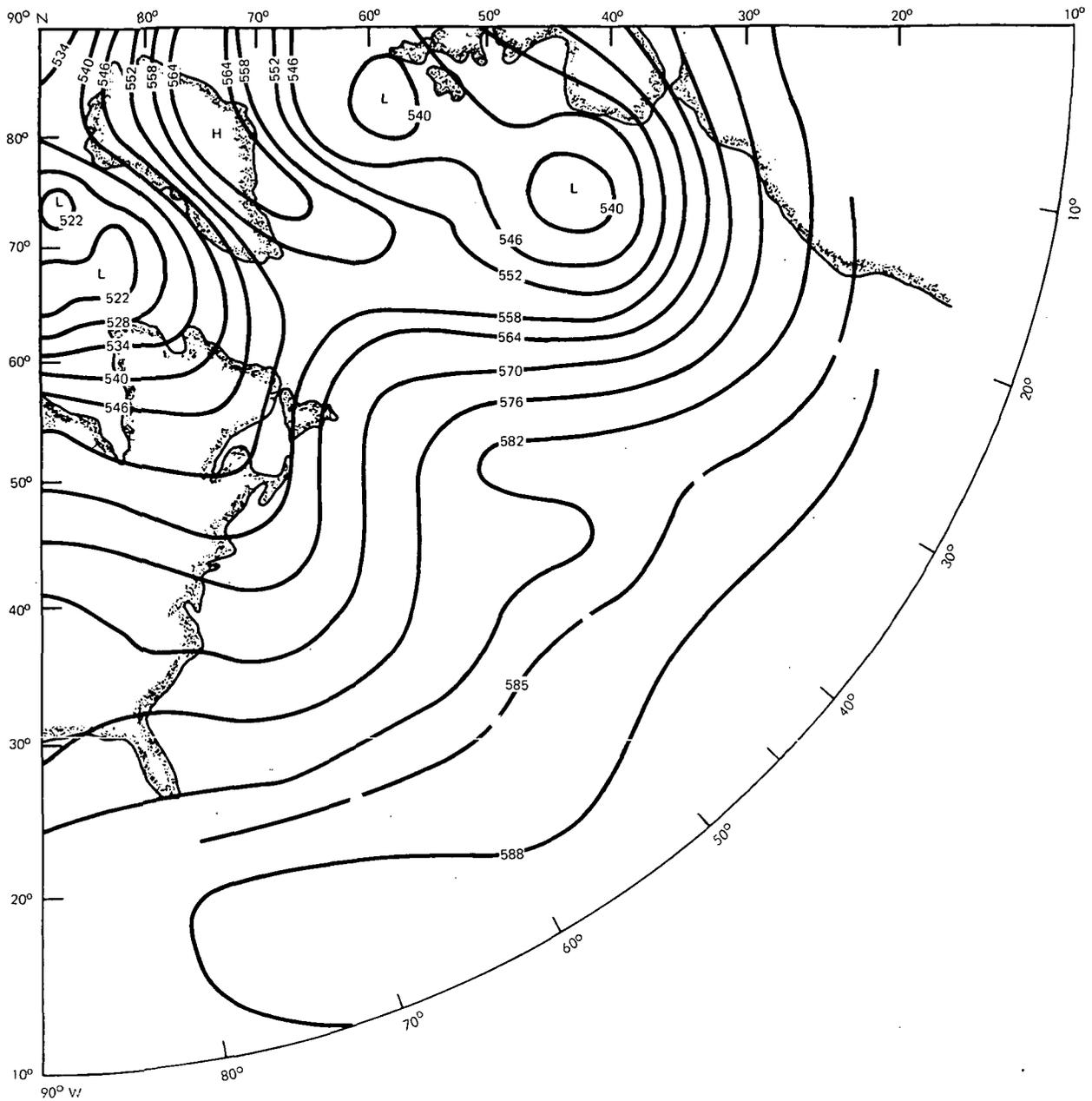
Figure 4.—NMC 50-kN·m^{-2} (500-mb) chart for 1200 GMT May 1, 1969 with geopotential heights in decameters.

CLOUD-TYPE DECISION LEGEND

1. CIRRUS
2. CIRRUS WITH LOW CLOUDS
3. CIRROSTRATUS AND / OR CUMULONIMBUS
4. CUMULONIMBUS
5. MIDDLE CLOUDS

6. MIDDLE CLOUDS WITH CIRRUS ABOVE
7. STRATUS OR STRATOCUMULUS
8. CUMULUS
9. CLEAR
10. NO DECISION
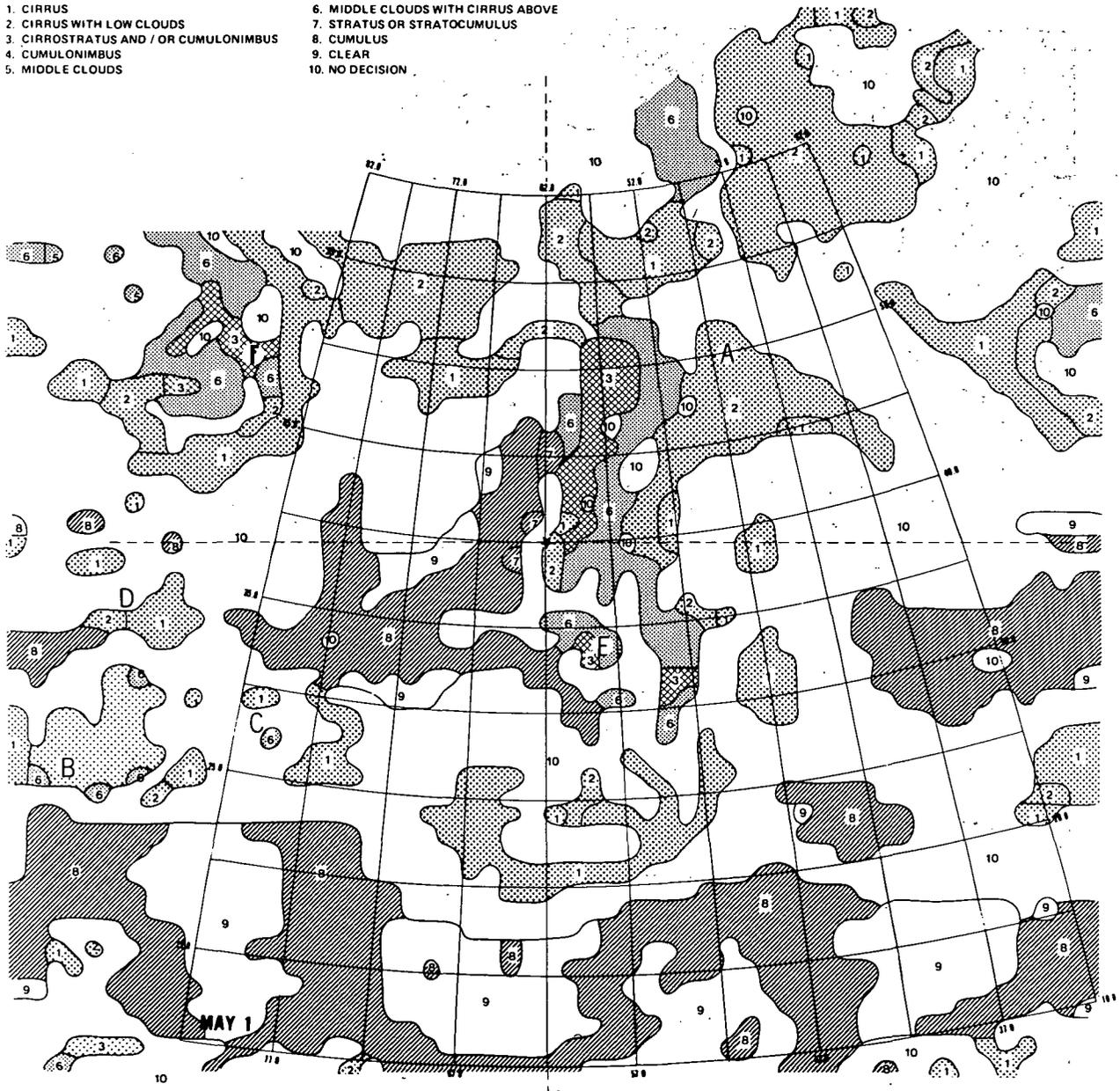
Figure 5.—Cloud-type decision map, May 1, 1969.

26
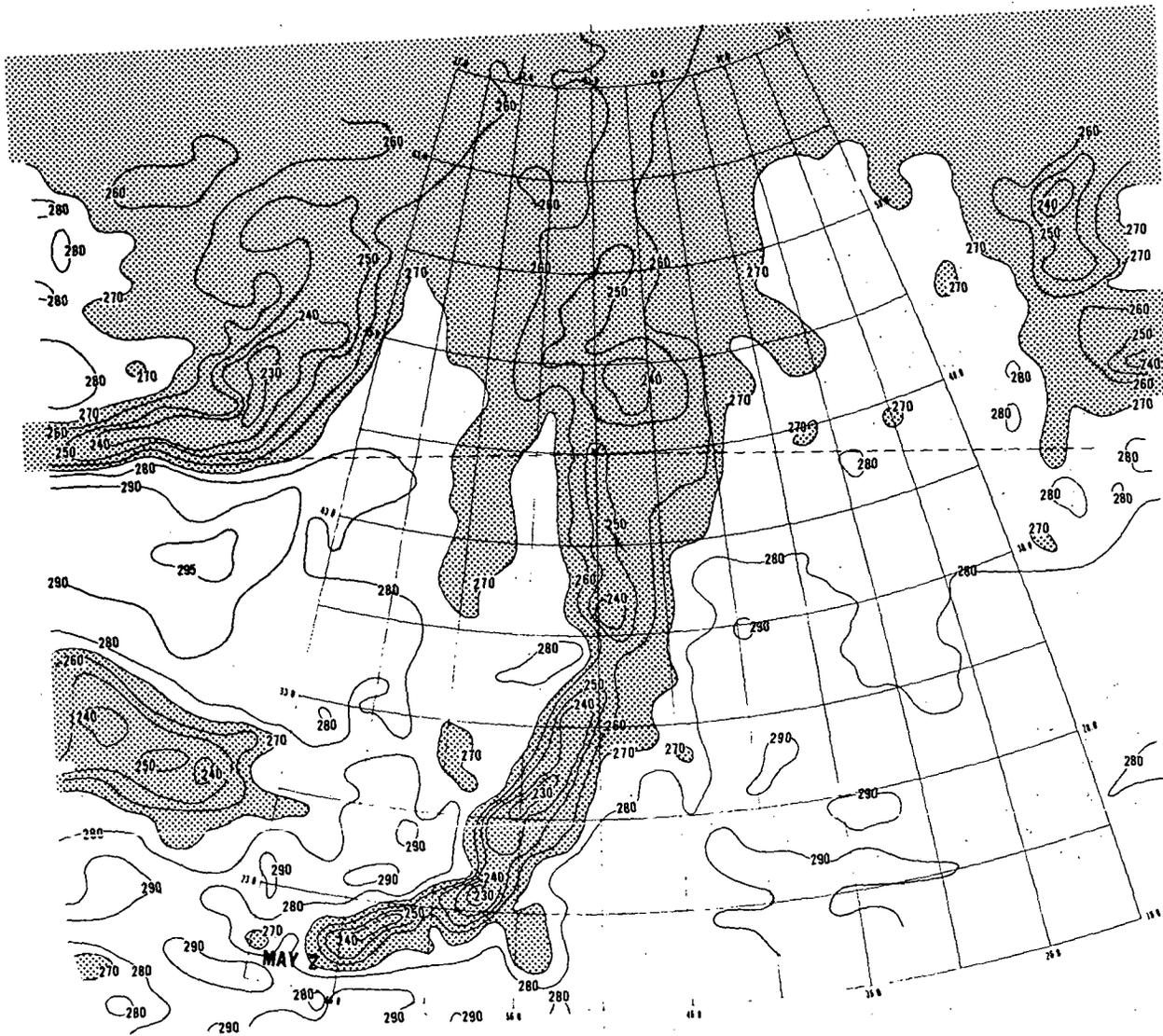
Figure 6.—Radiation maps for May 2, 1969. (a) 10- to 11-μm. Isotherms are in °Kelvin.
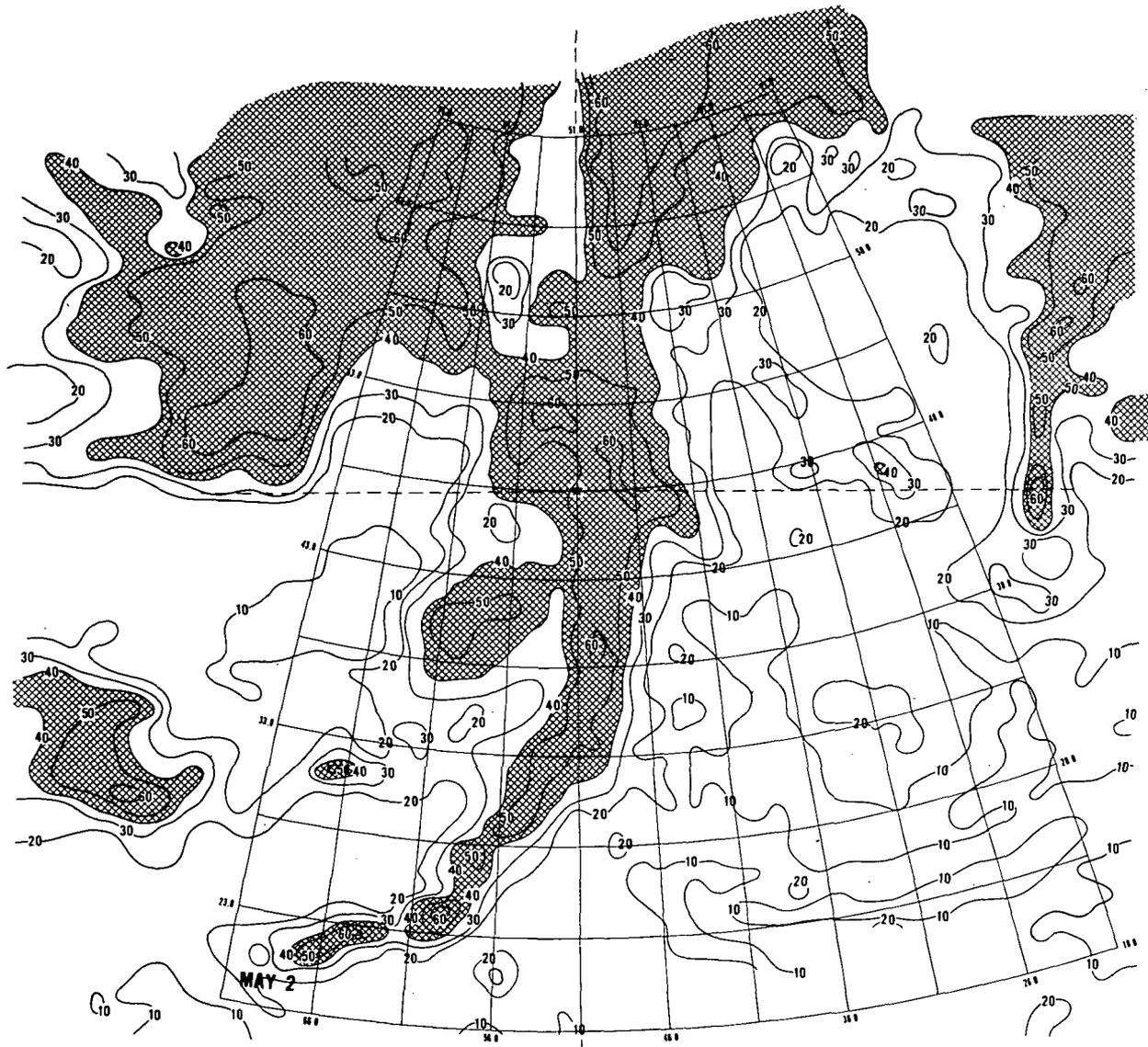
Figure 6 (continued.—Radiation maps for May 2, 1969. (b) 0.2- to 4.0-μm. Isolines are normalized reflectances in percent.

Figure 6 (continued).—Radiation maps for May 2, 1969. (c) 6.5- to 7.0-μm. Isotherms are in °Kelvin.
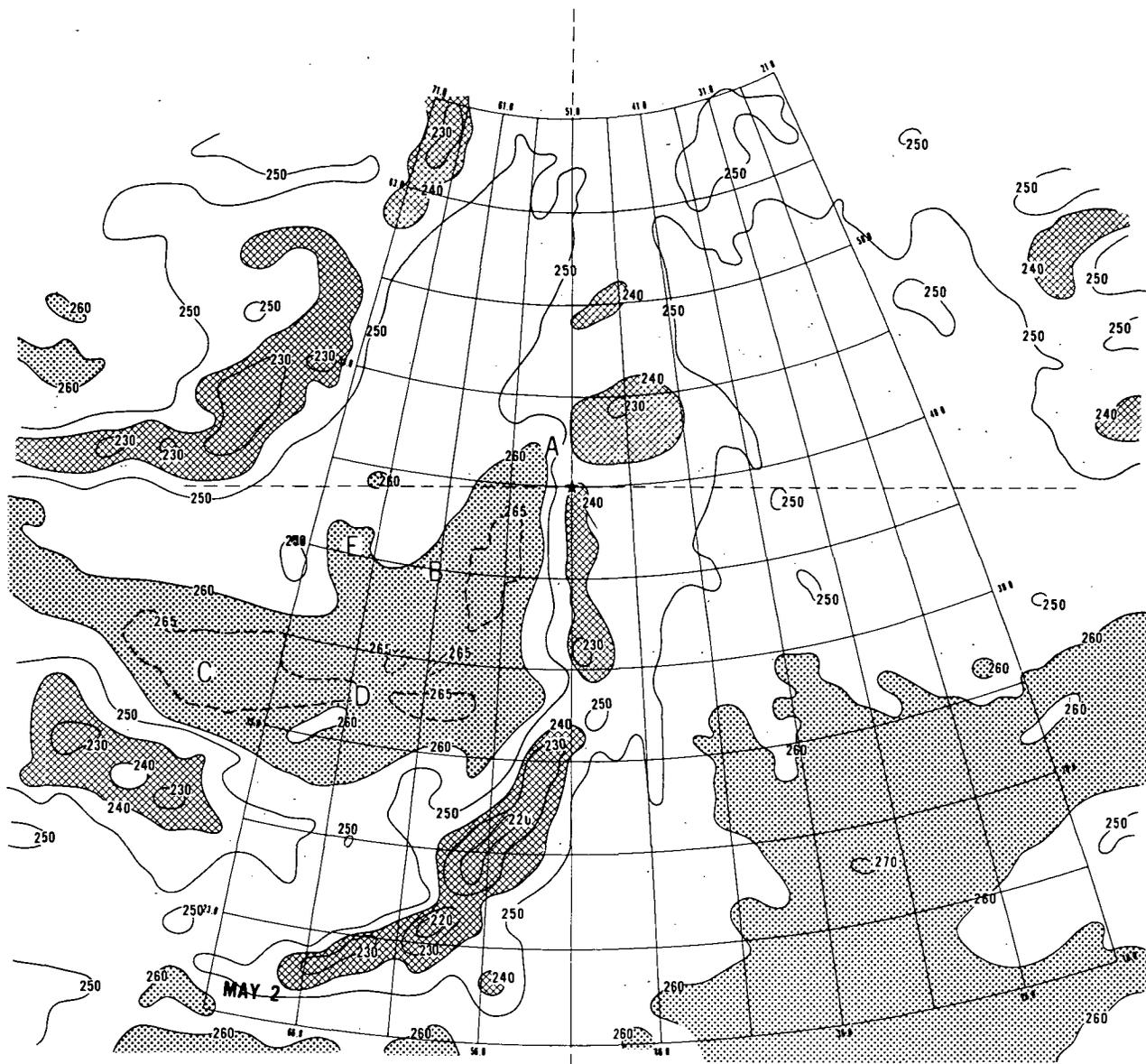
Figure 6 (concluded).—Radiation maps for May 2, 1969. (d) 20- to 23-μm. Isotherms are in °Kelvin.
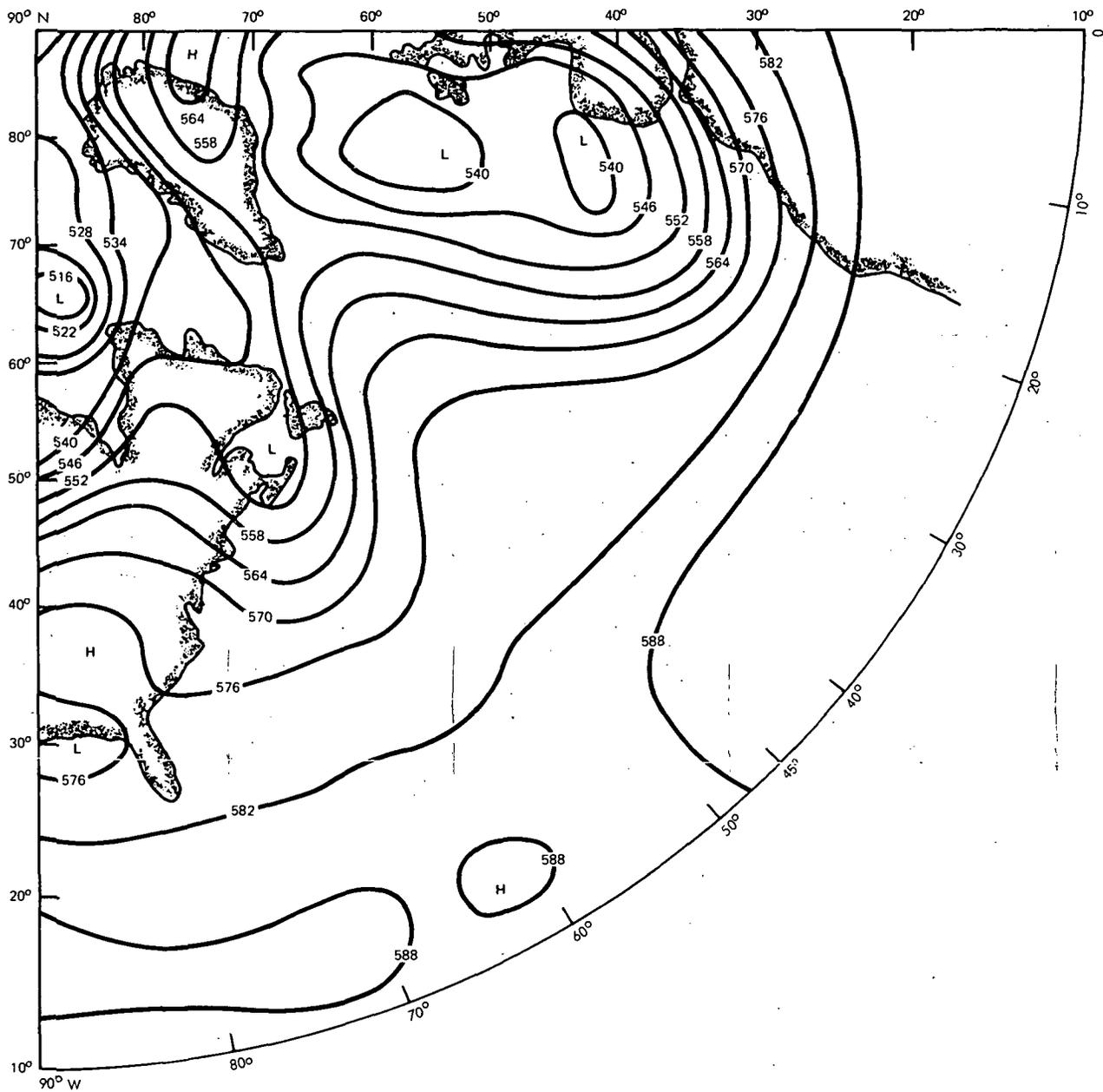
Figure 7.—NMC 50-kN·m^{-2} (500-mb) chart for 1200 GMT May 2, 1969 with geopotential heights in decameters.

1. CIRRUS
2. CIRRUS WITH LOW CLOUDS
3. CIRROSTRATUS AND / OR CUMULONIMBUS
4. CUMULONIMBUS
5. MIDDLE CLOUDS

6. MIDDLE CLOUDS WITH CIRRUS ABOVE
7. STRATUS OR STRATOCUMULUS
8. CUMULUS
9. CLEAR
10. NO DECISION
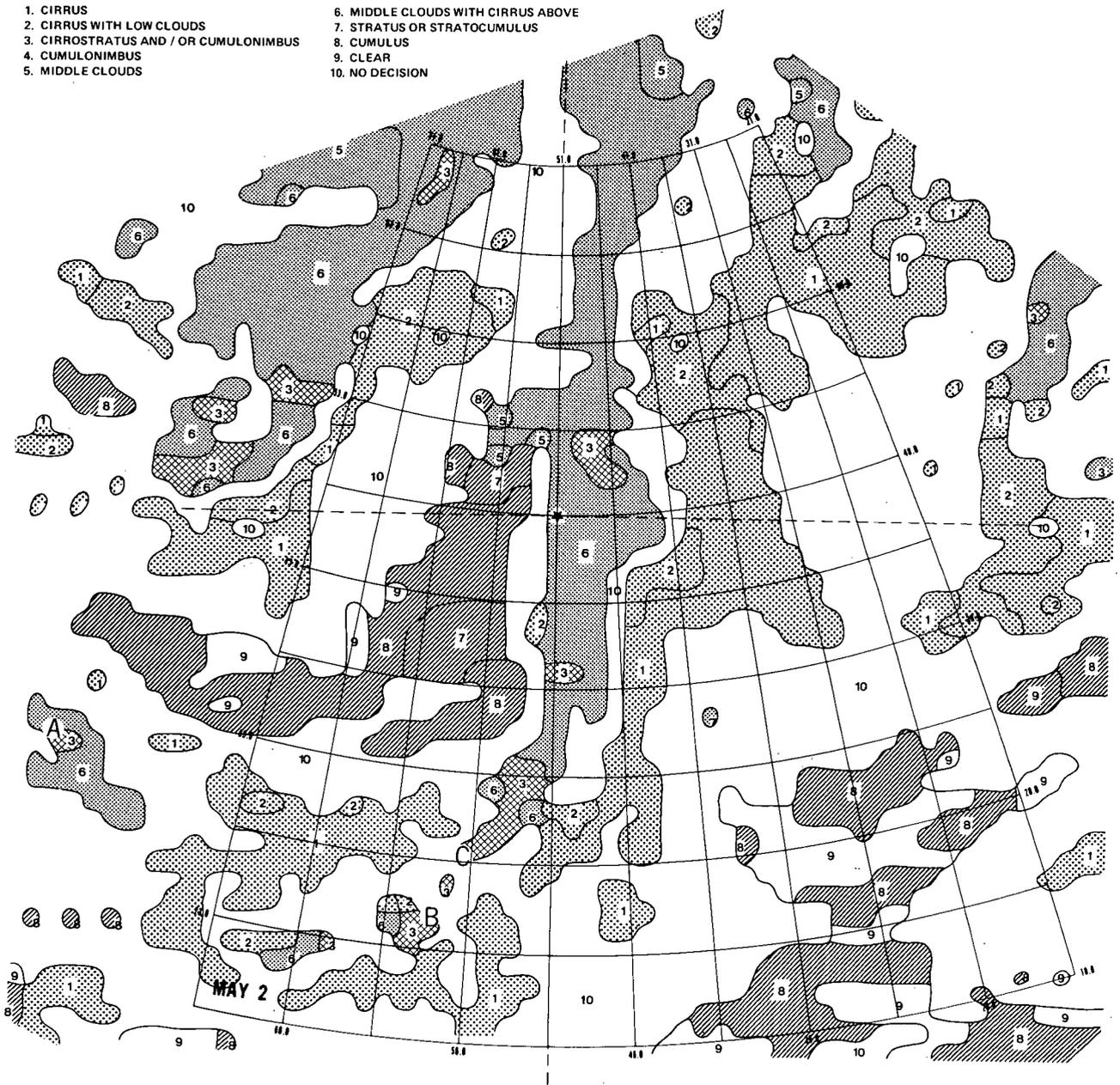
Figure 8.—Cloud-type decision map, May 2, 1969.

32
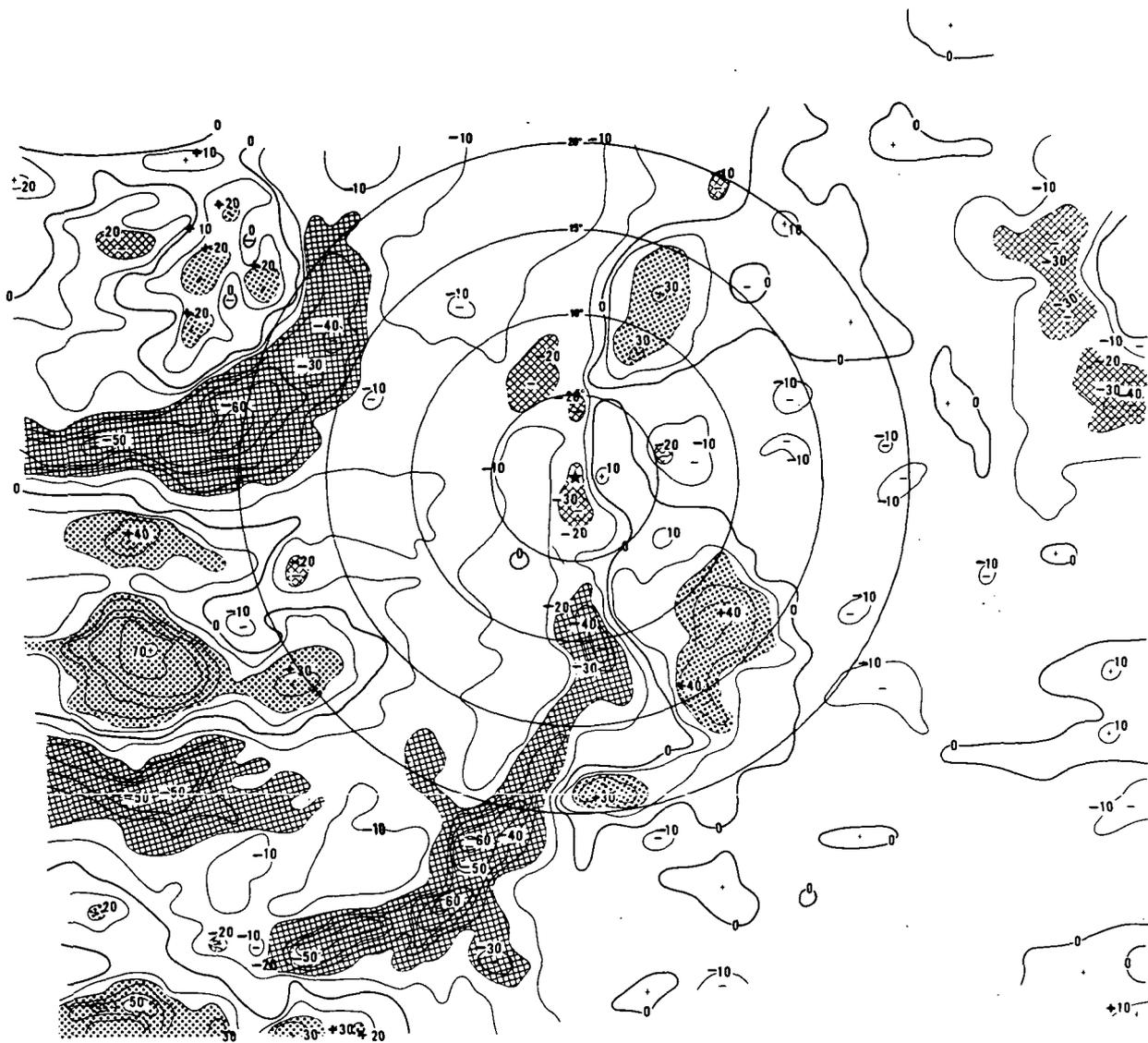
Figure 9.—Radiation difference maps for May 1 and 2, 1969. (a) 10- to 11-μm. Isotherms are in °Kelvin.
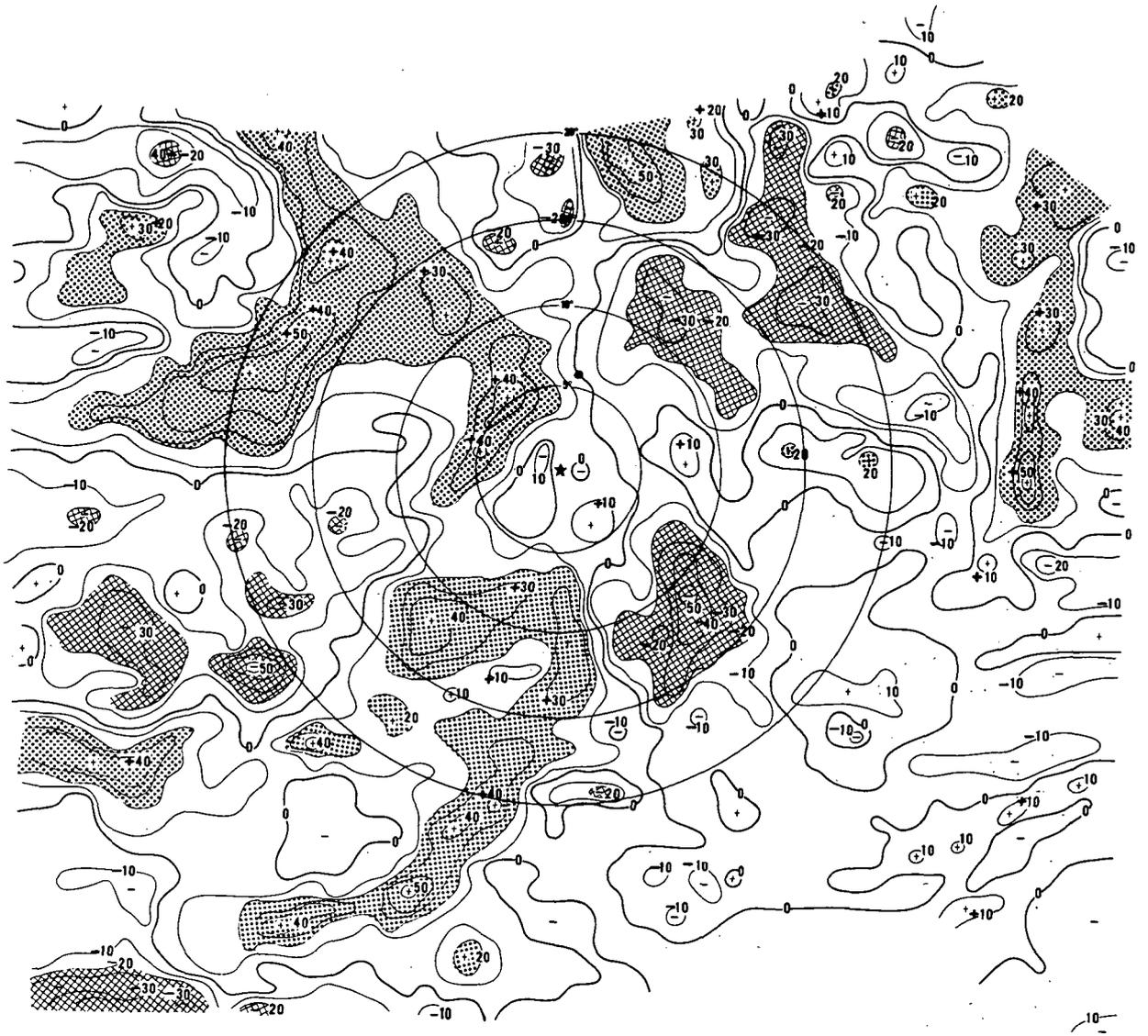
Figure 9 (continued).—Radiation difference maps for May 1 and 2, 1969. (b) 0.2- to 4.0-μm. Isolines are normalized reflectance differences in percent. The circles are in degrees of latitude from the cyclone center.
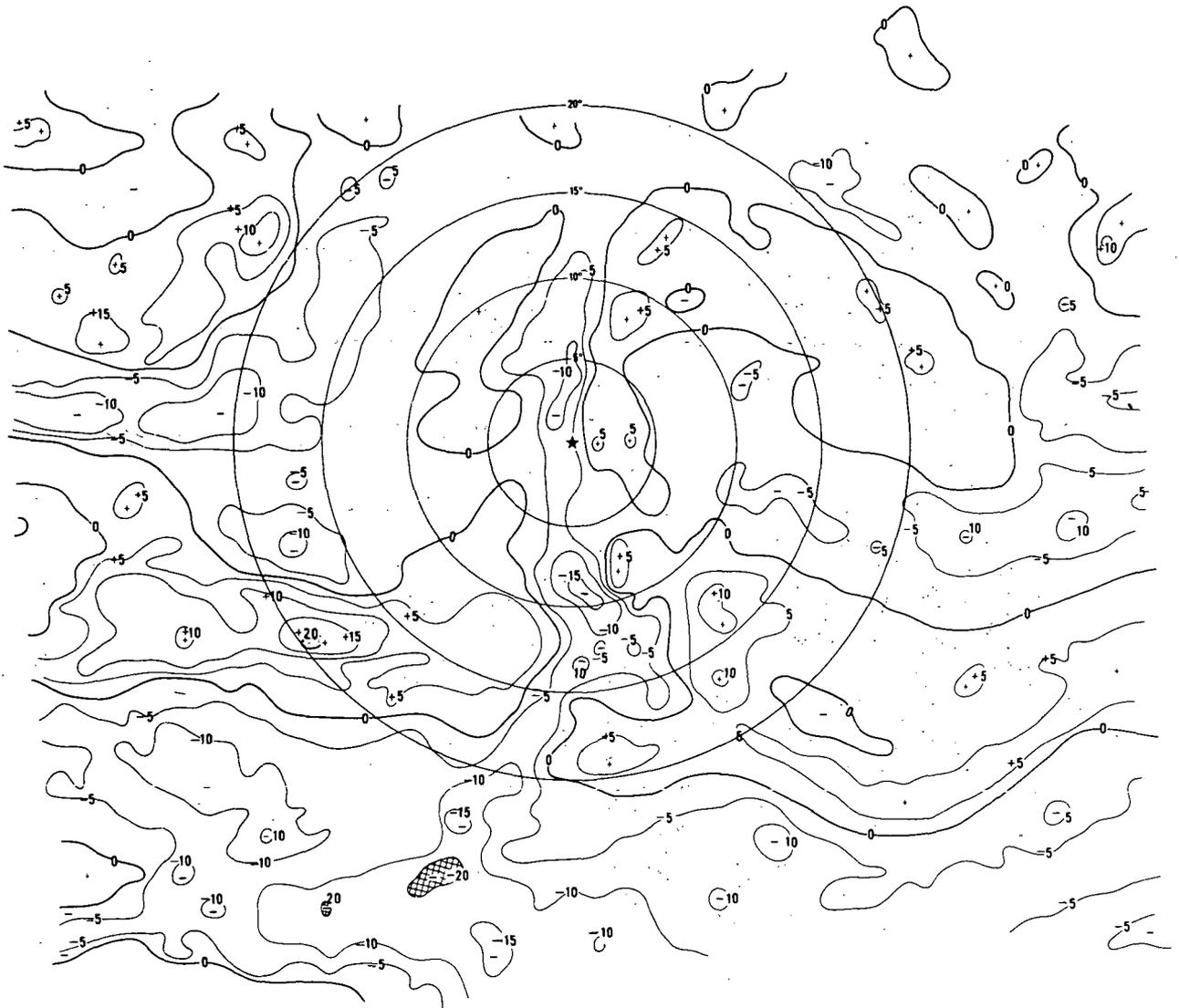
Figure 9 (continued).—Radiation difference maps for May 1 and 2, 1969. (c) 6.5- to 7.0-μm. Isolines are equivalent blackbody temperature differences in °Kelvin. The circles are in degrees of latitude from the cyclone center.
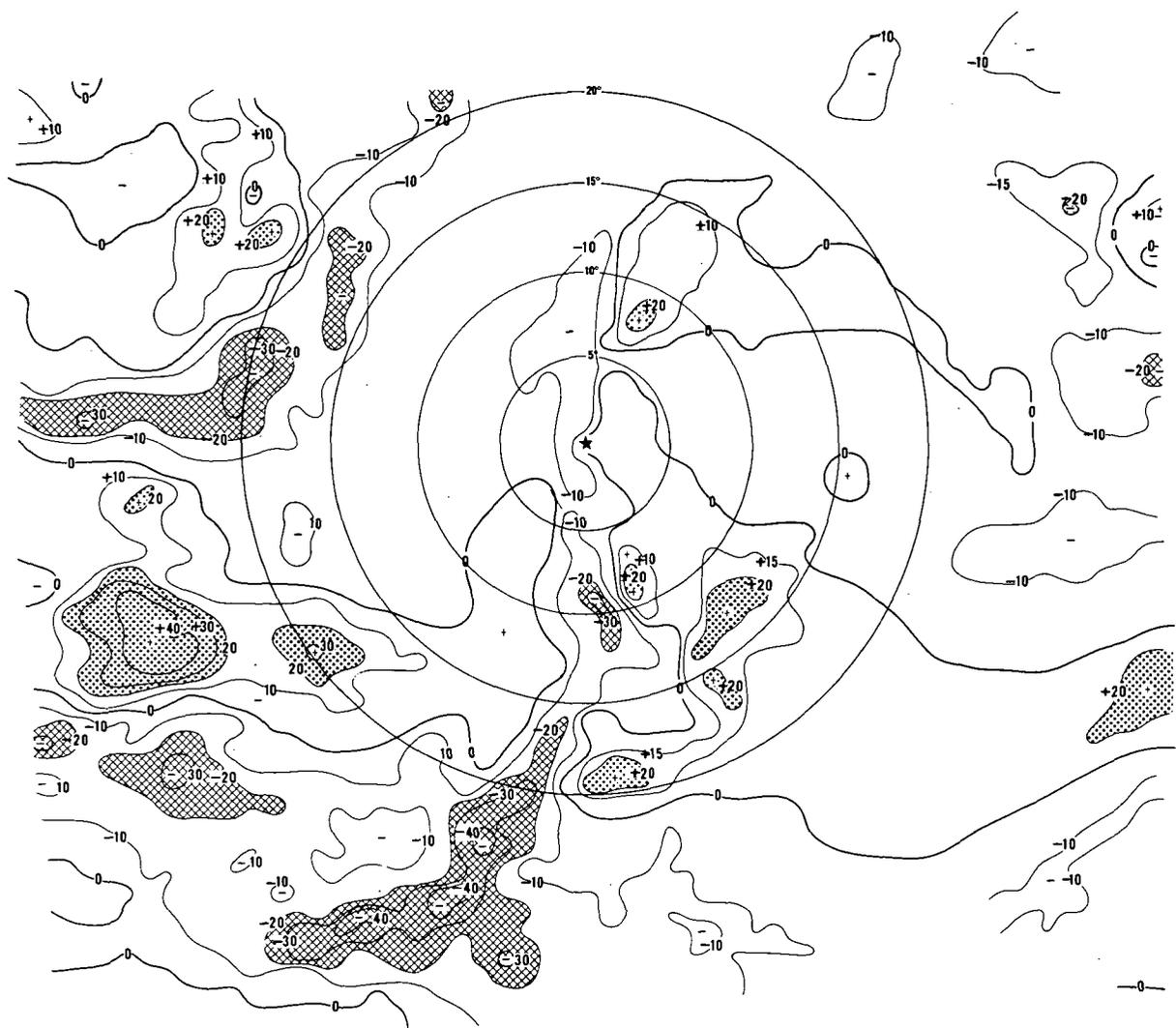
Figure 9 (continued).—Radiation difference maps for May 1 and 2, 1969. (d) 20- to 23-μm. Isolines are equivalent blackbody temperature differences in °Kelvin. The circles are in degrees of latitude from the cyclone center.
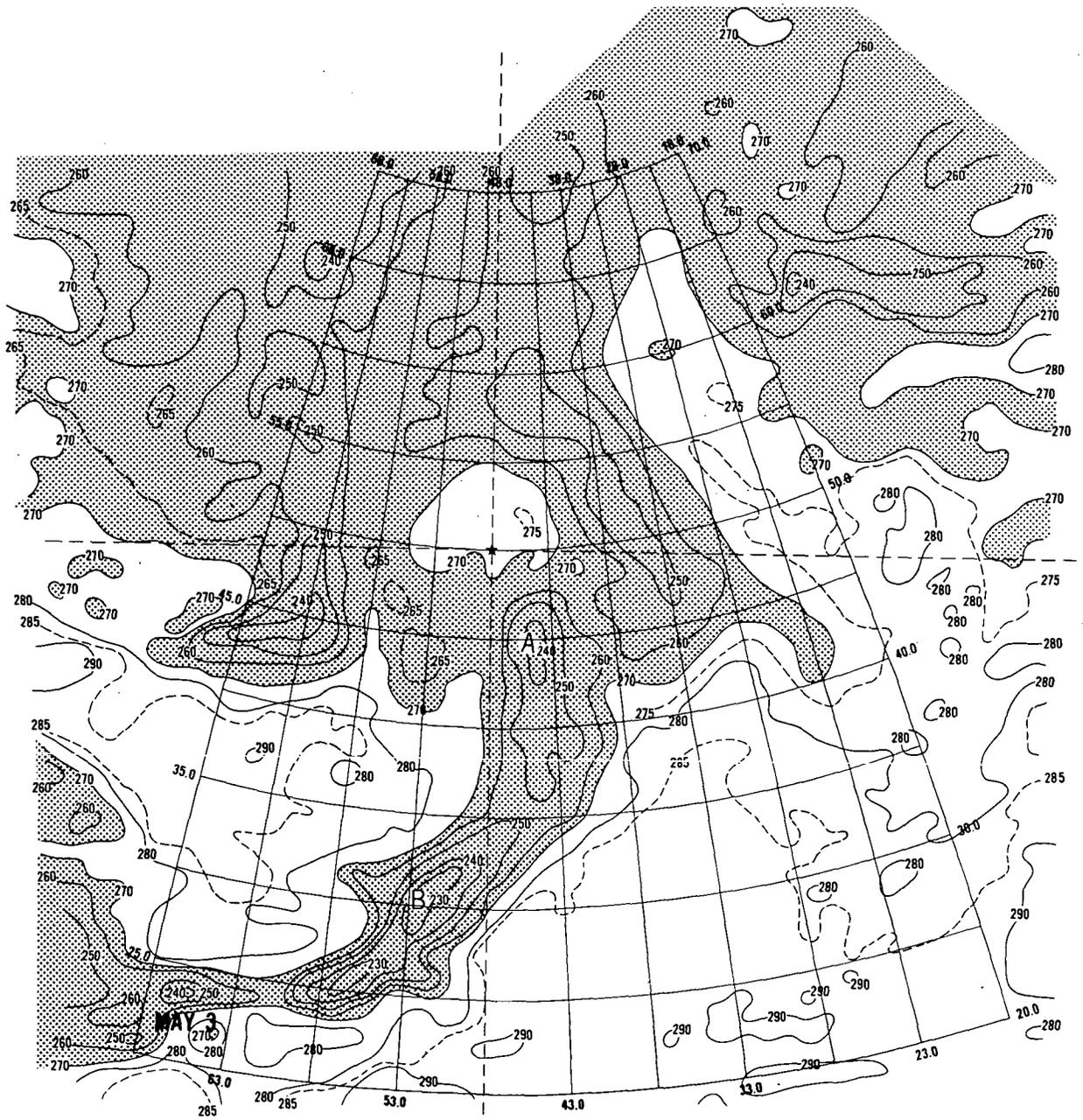
Figure 10.—Radiation maps for May 3, 1969. (a) 10- to 11-µm. Isotherms are in °Kelvin.
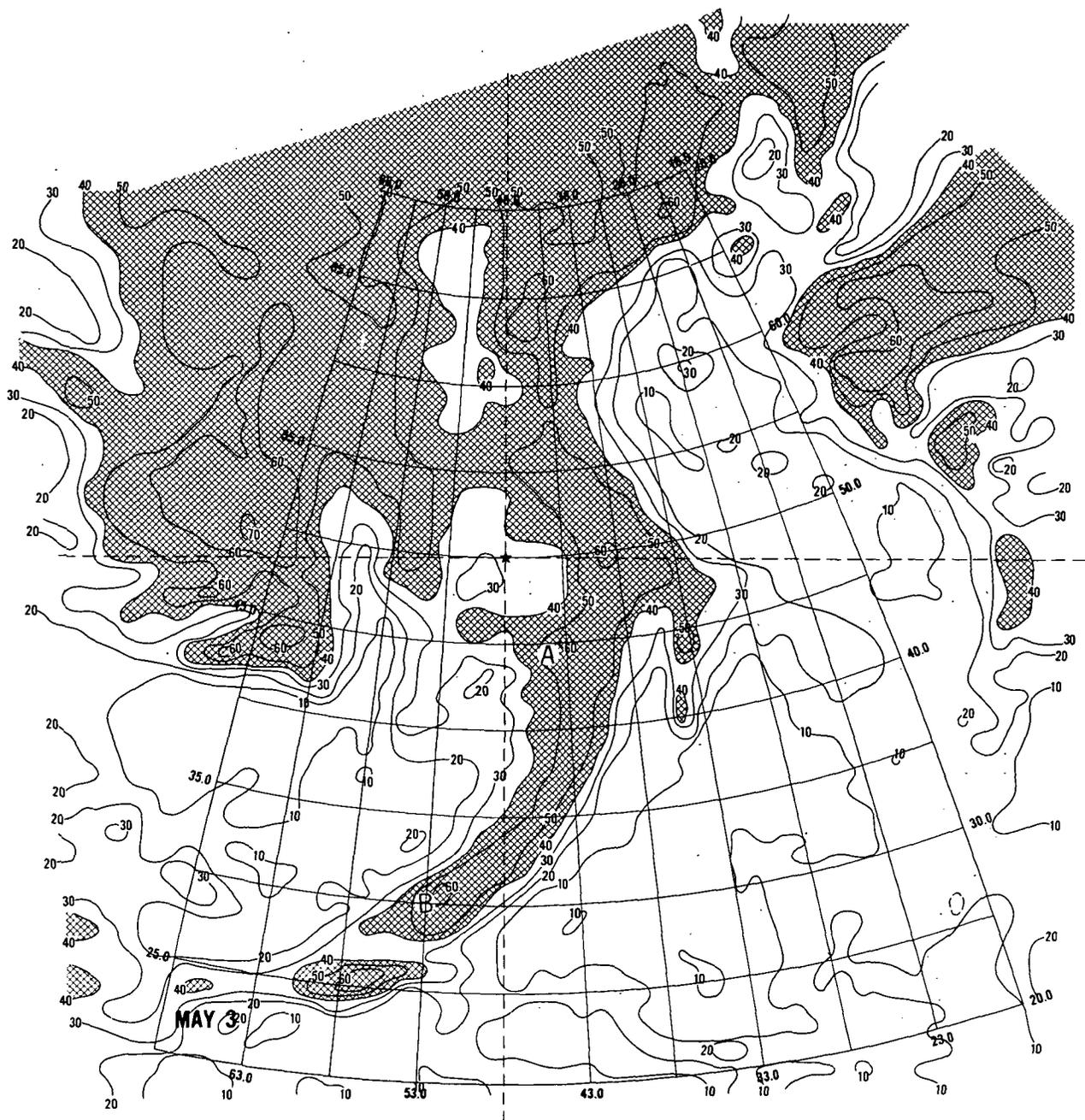
Figure 10 (continued).—Radiation maps for May 3, 1969. (b) 0.2- to 4.0-μm. Isolines are normalized reflectances in percent.
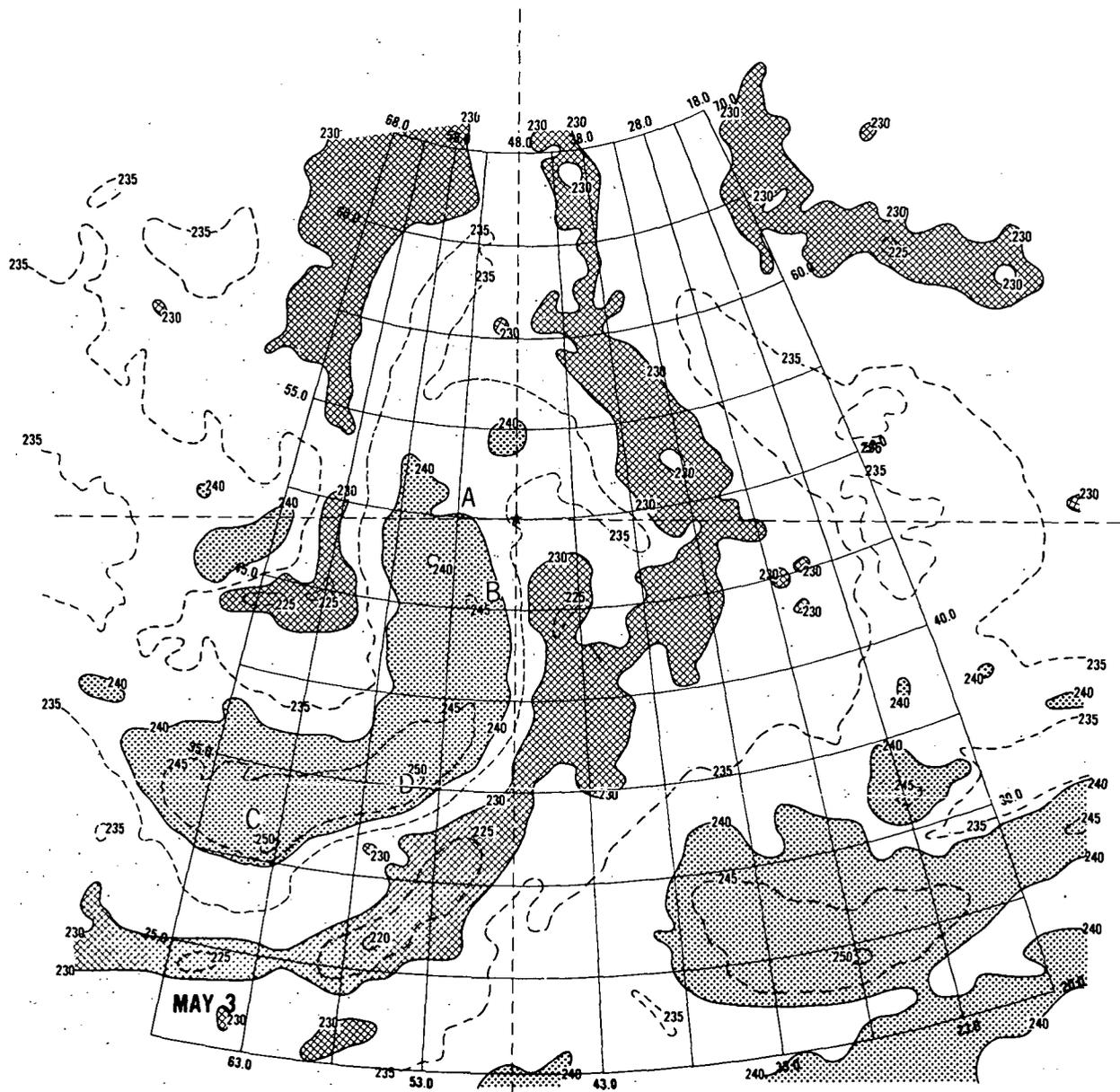
Figure 10 (continued).—Radiation maps for May 3, 1969. (c) 6.5- to 7.0-μm.
Isotherms are in °Kelvin.
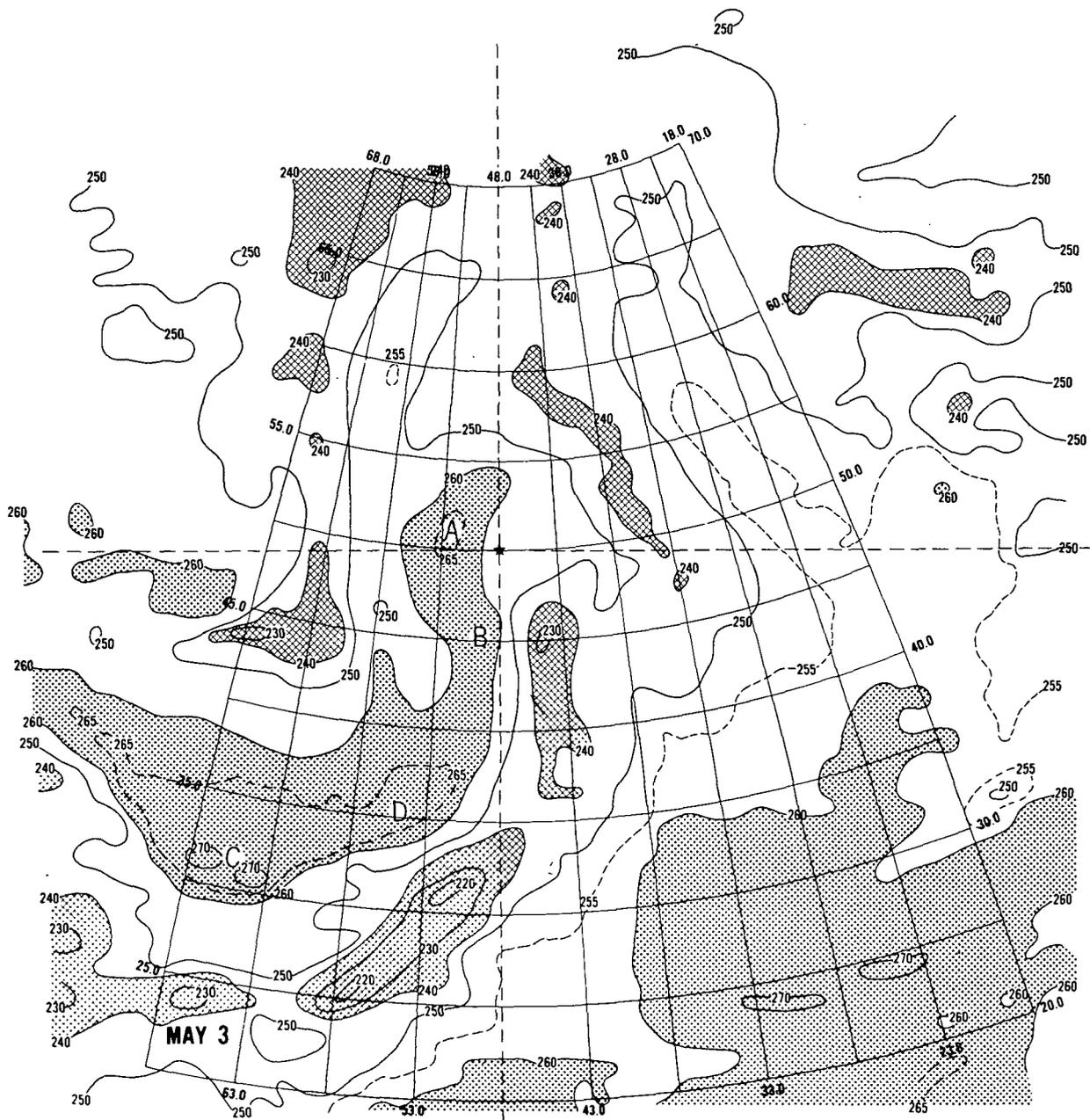
Figure 10 (concluded).—Radiation maps for May 3, 1969. (d) 20- to 23-μm.
Isotherms are in °Kelvin.
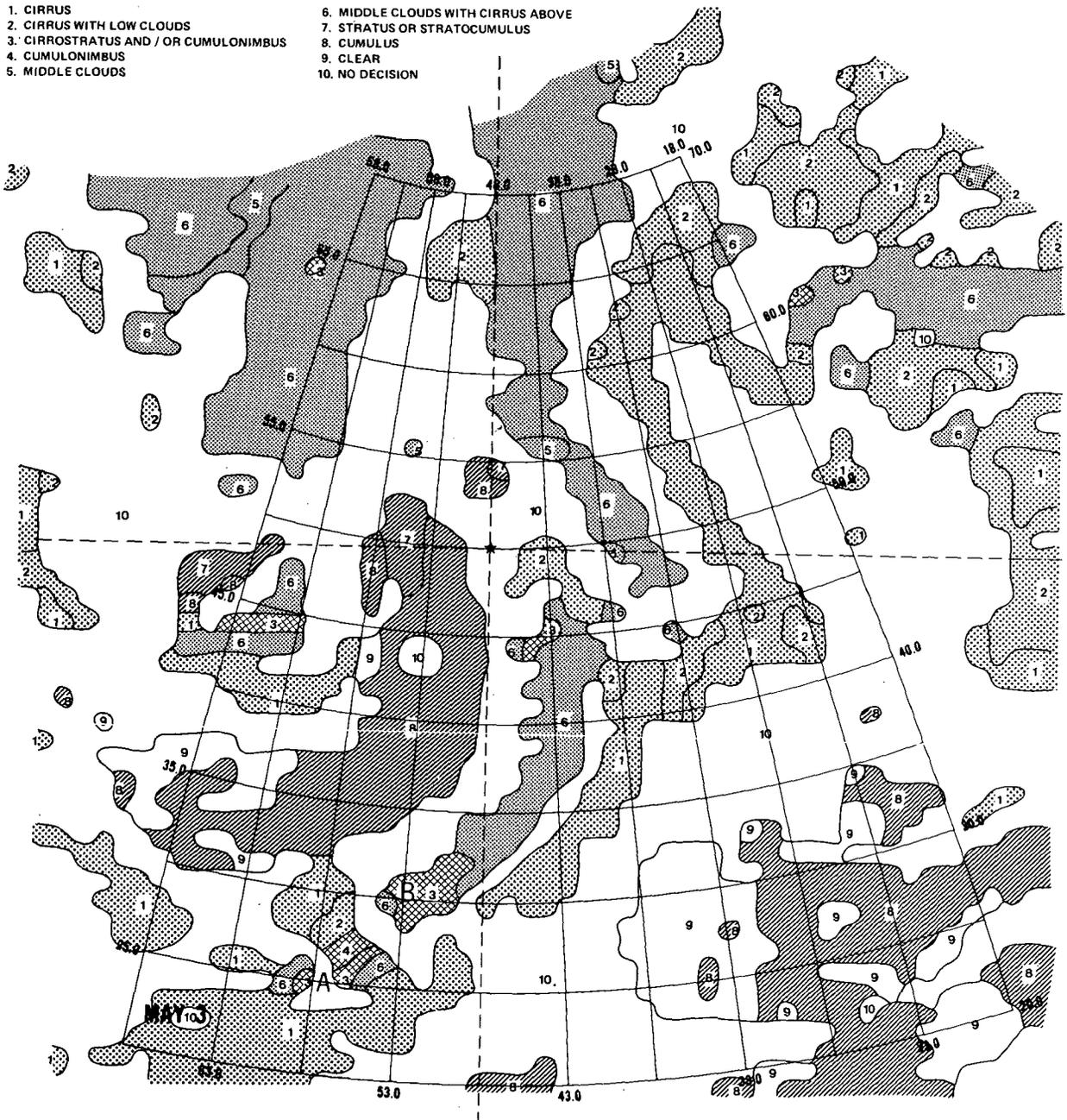
Figure 11.—Cloud-type decision map, May 3, 1969.
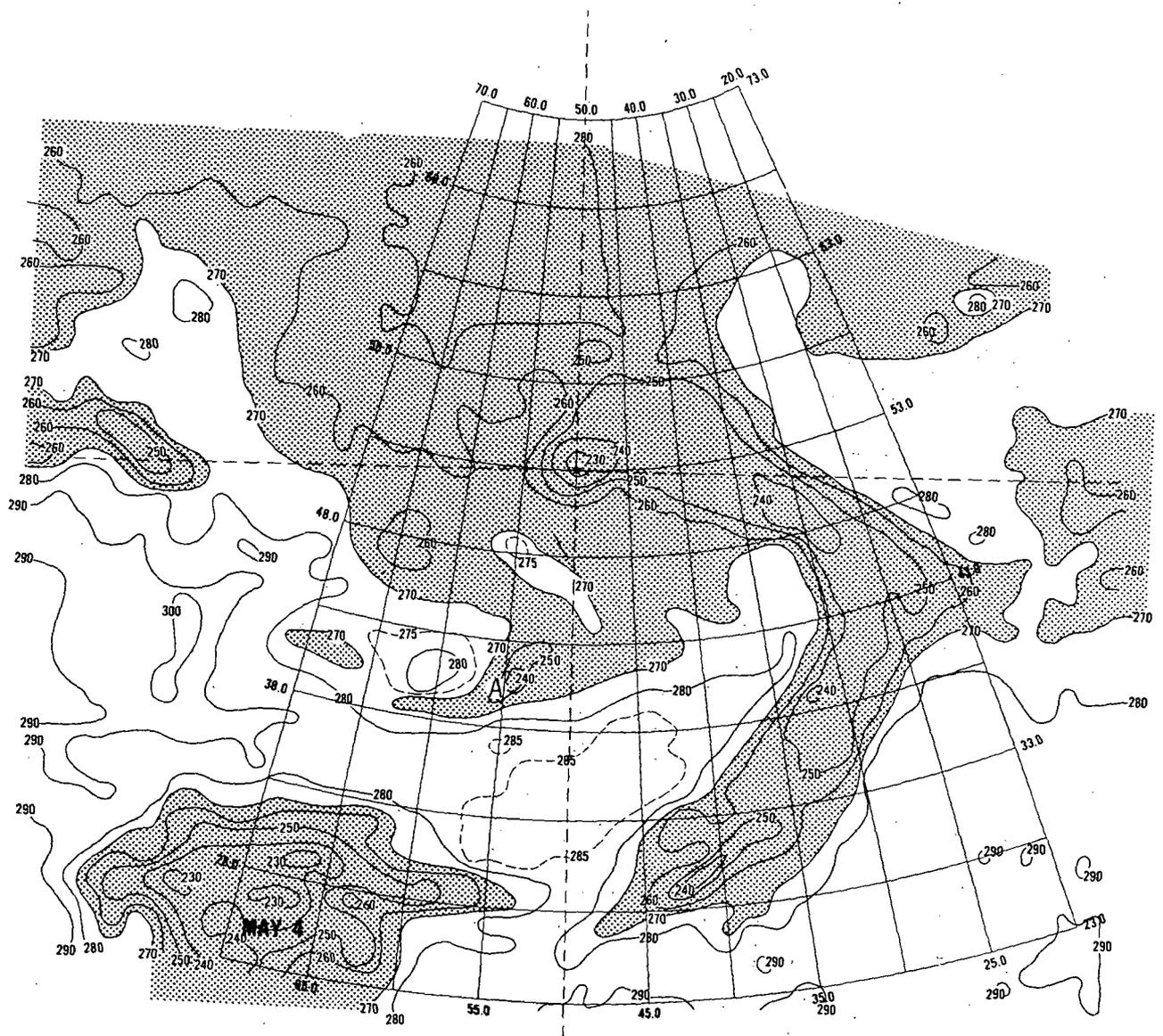
Figure 12.—Radiation maps for May 4, 1969. (a) 10- to 11-μm.   Isotherms are in °Kelvin.
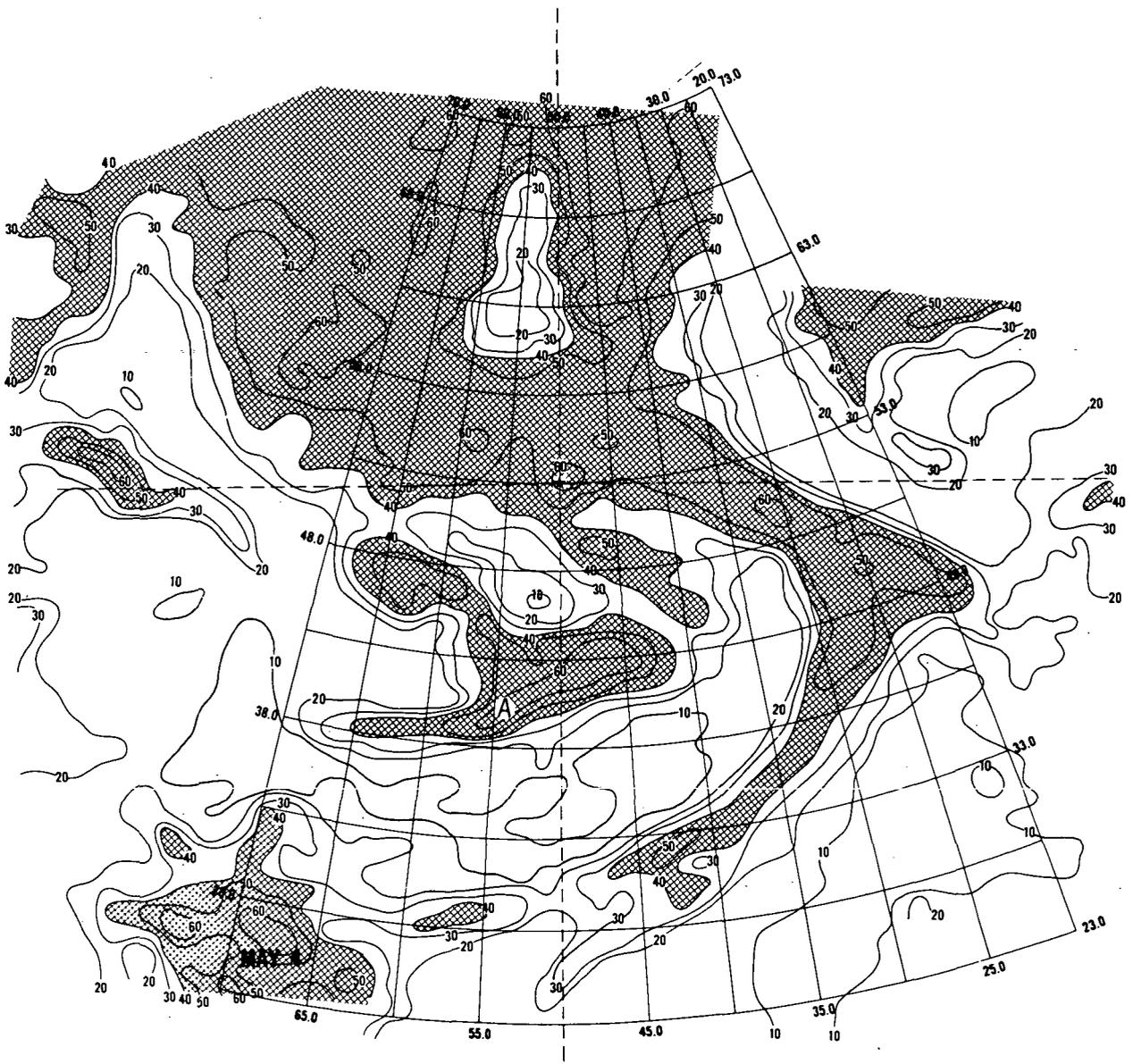
Figure 12 (continued).—Radiation maps for May 4, 1969. (b) 0.2- to 4.0-μm. Isolines are normalized reflectances in percent.

43
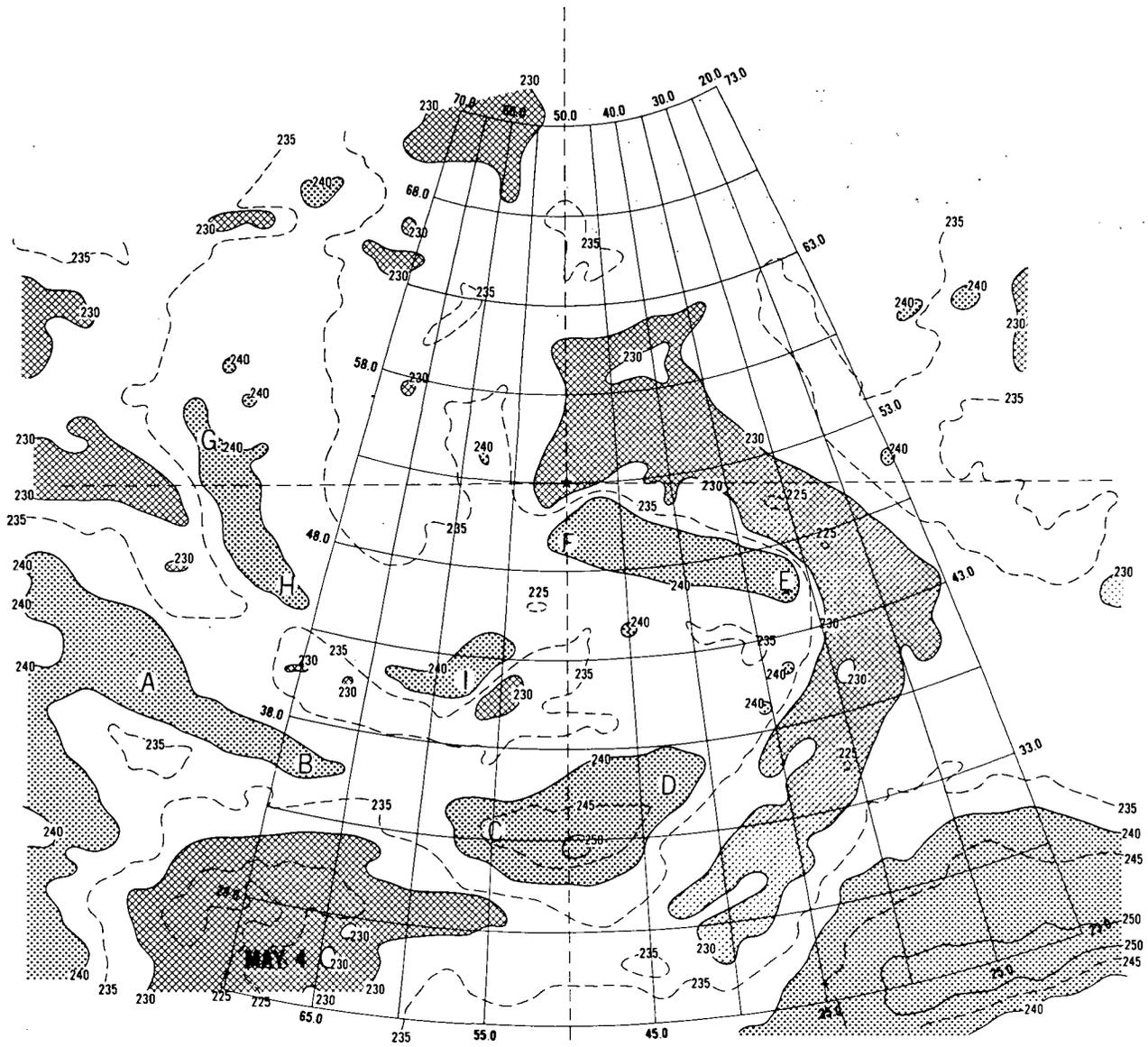
Figure 12 (continued).—Radiation maps for May 4, 1969. (c) 6.5- to 7.0-μm. Isotherms are in °Kelvin.
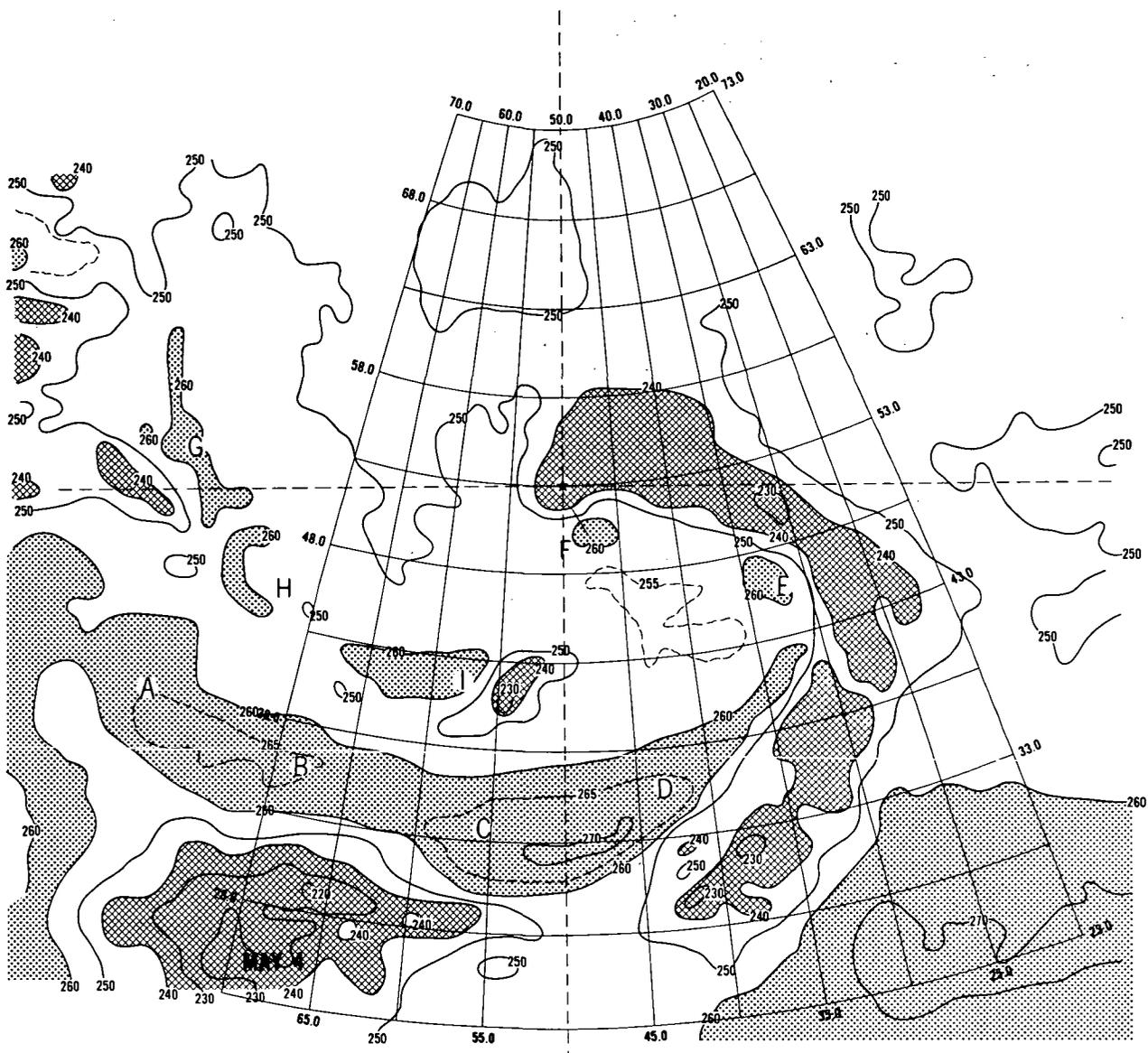
Figure 12 (concluded).—Radiation maps for May 4, 1969. (d) 20- to 23-μm. Isotherms are in $^\circ$Kelvin.
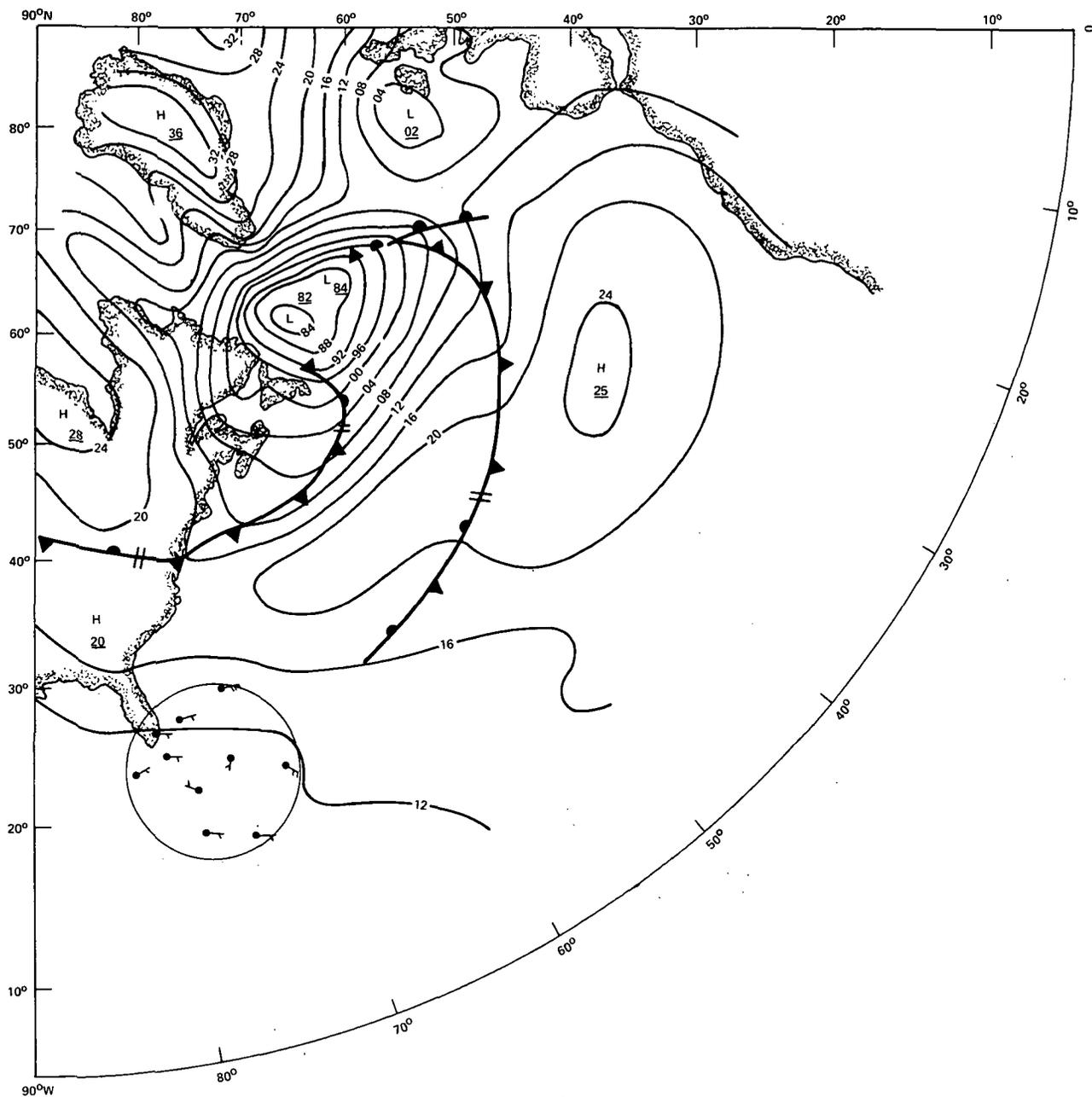
Figure 13.—NMC surface chart, 1200 GMT May 4, 1969. The wind directions and speeds for selected land stations and ship reports are shown within the circle south and east of the Florida coast.

CLOUD-TYPE DECISION LEGEND

1. CIRRUS
2. CIRRUS WITH LOW CLOUDS
3. CIRROSTRATUS AND / OR CUMULONIMBUS
4. CUMULONIMBUS
5. MIDDLE CLOUDS

6. MIDDLE CLOUDS WITH CIRRUS ABOVE
7. STRATUS OR STRATOCUMULUS
8. CUMULUS
9. CLEAR
10. NO DECISION
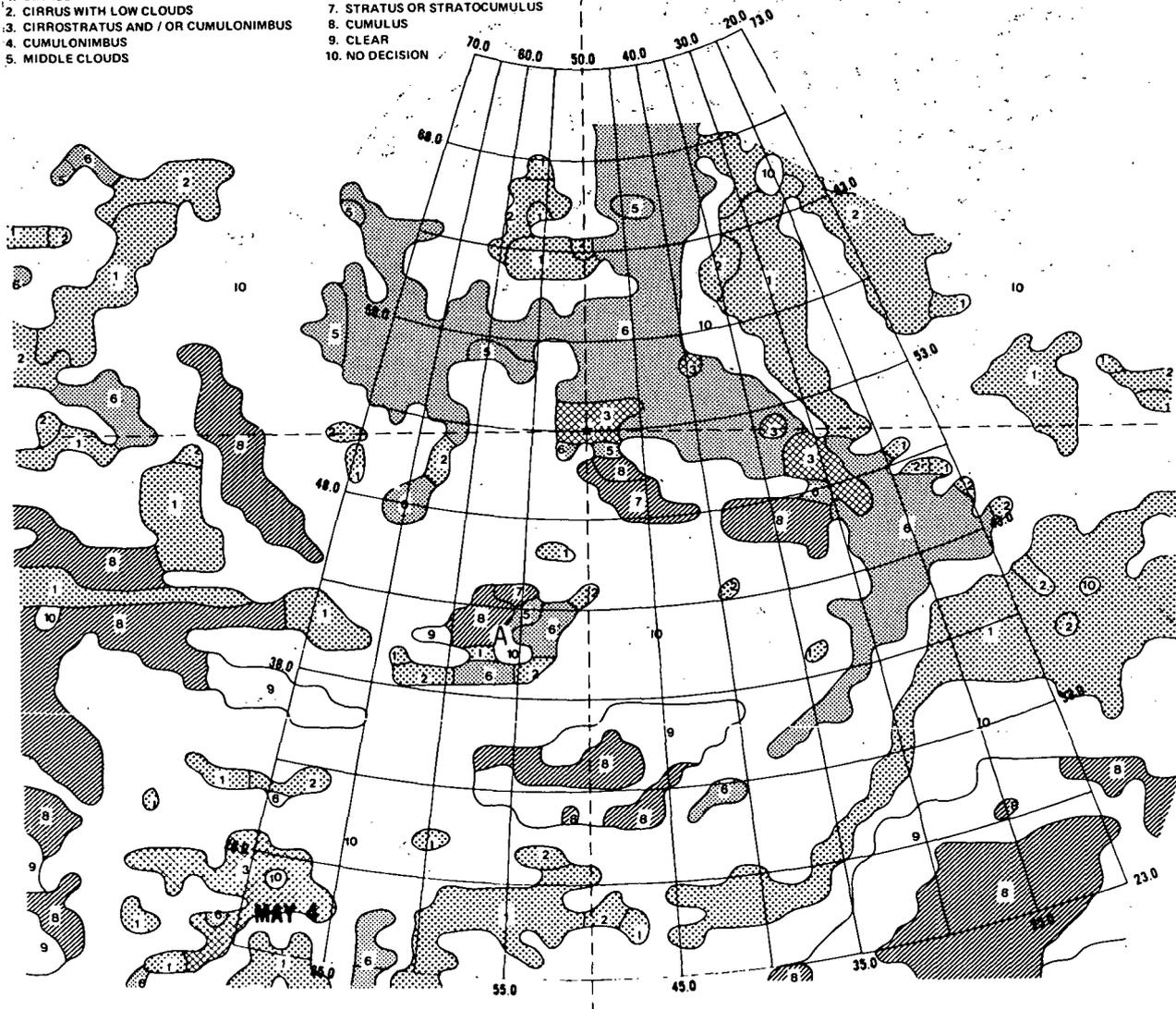
Figure 14.—Cloud-type decision map, May 4, 1969.
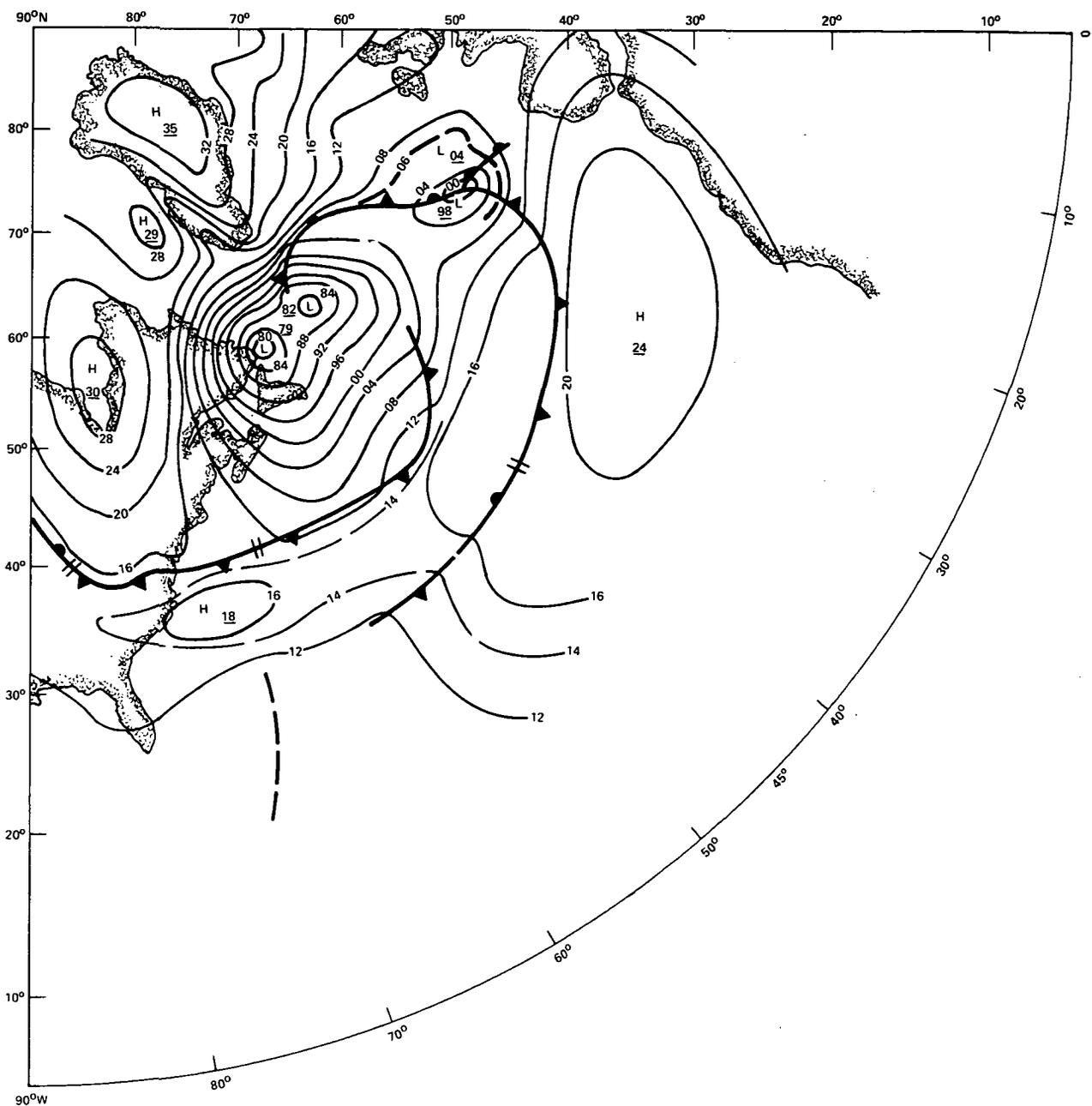
Figure 15.—NMC surface chart, 0600 GMT May 5, 1969.
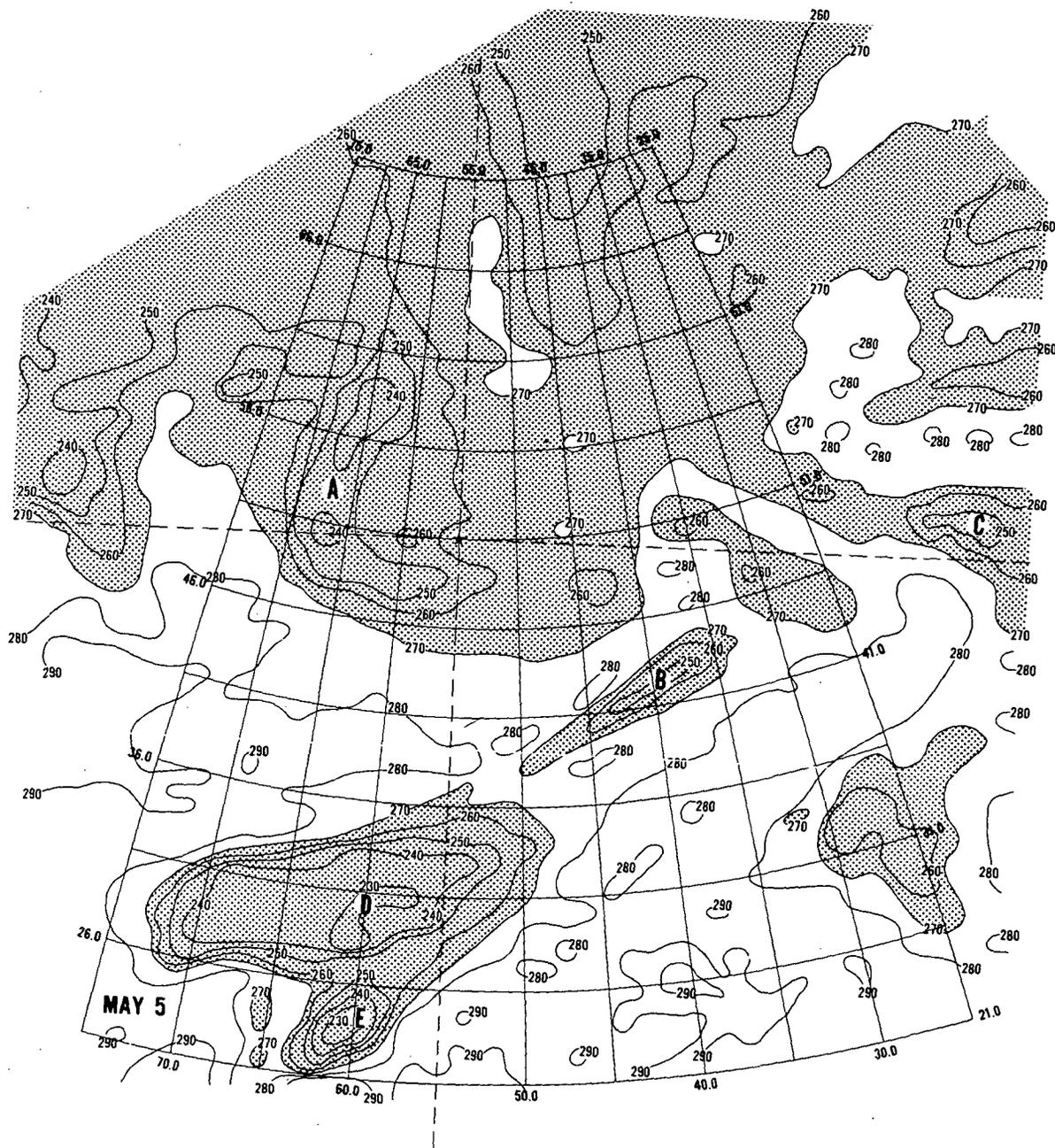
Figure 16.—Radiation maps for May 5, 1969. (a) 10- to 11-μm. Isotherms are in °Kelvin.
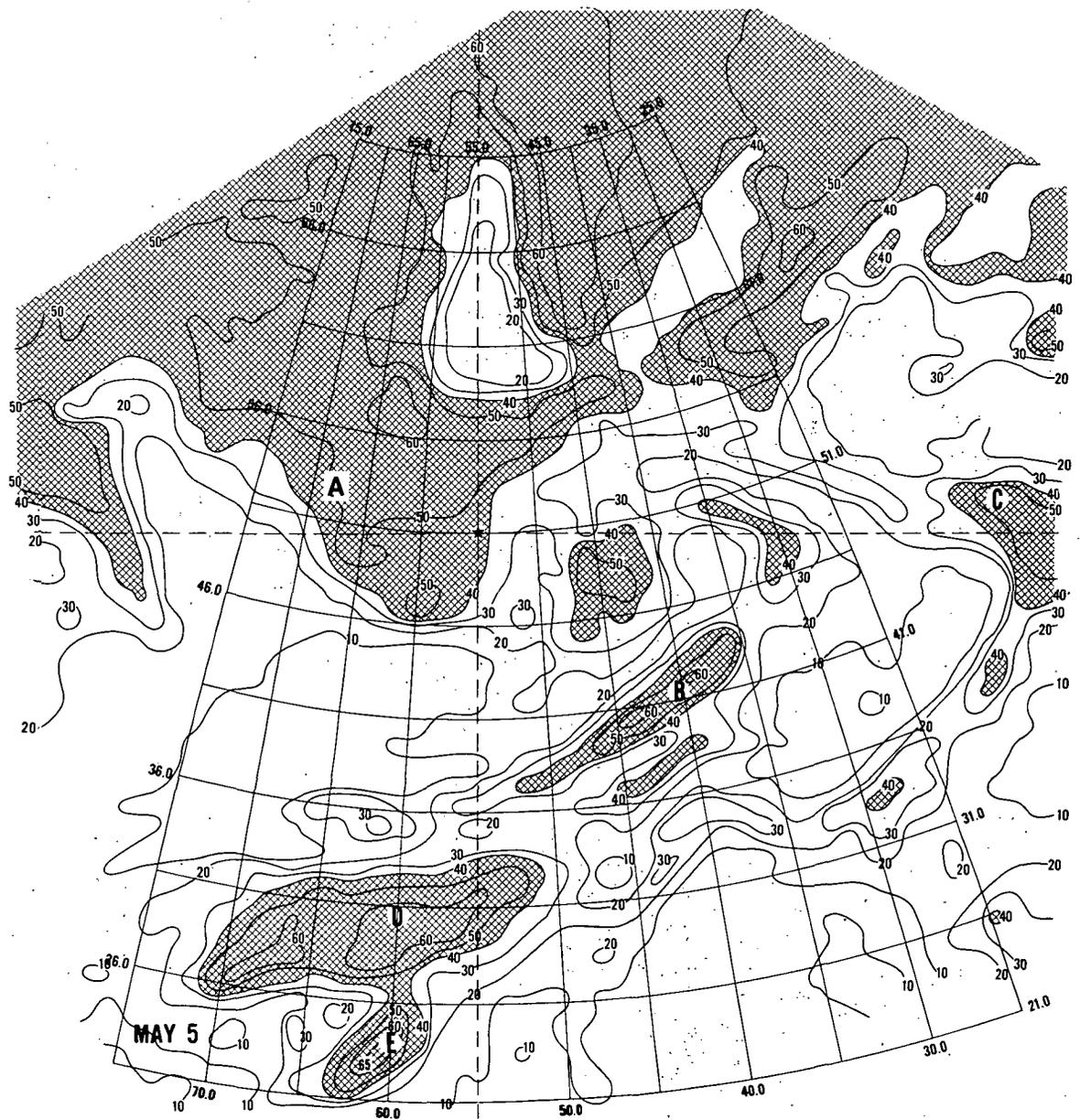
Figure 16 (continued).—Radiation maps for May 5, 1969. (b) 0.2- to 4.0-µm. Isolines are normalized reflectances in percent.
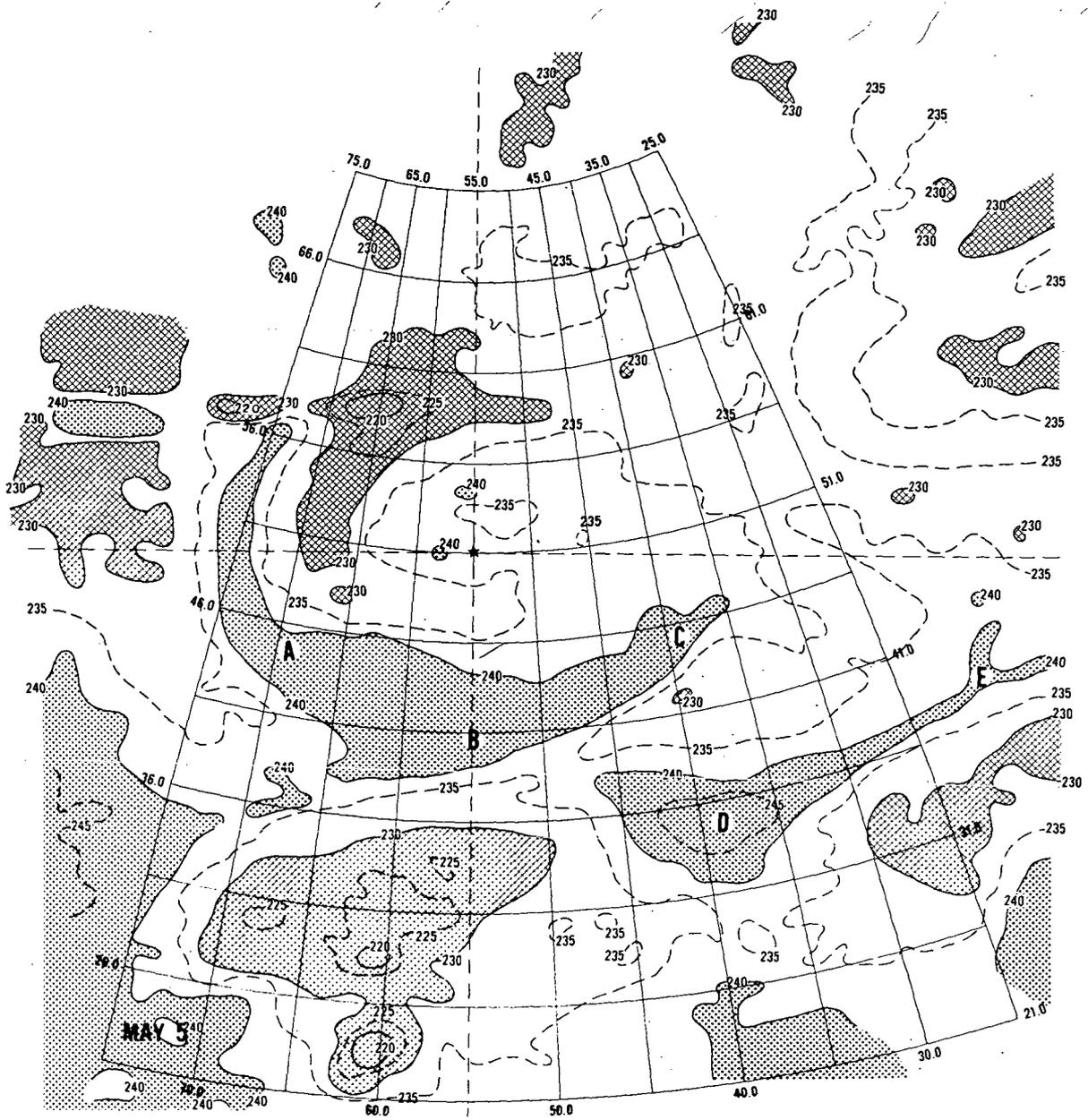
Figure 16 (continued).—Radiation maps for May 5, 1969. (c) 6.5- to 7.0-μm. Isotherms are in °Kelvin.
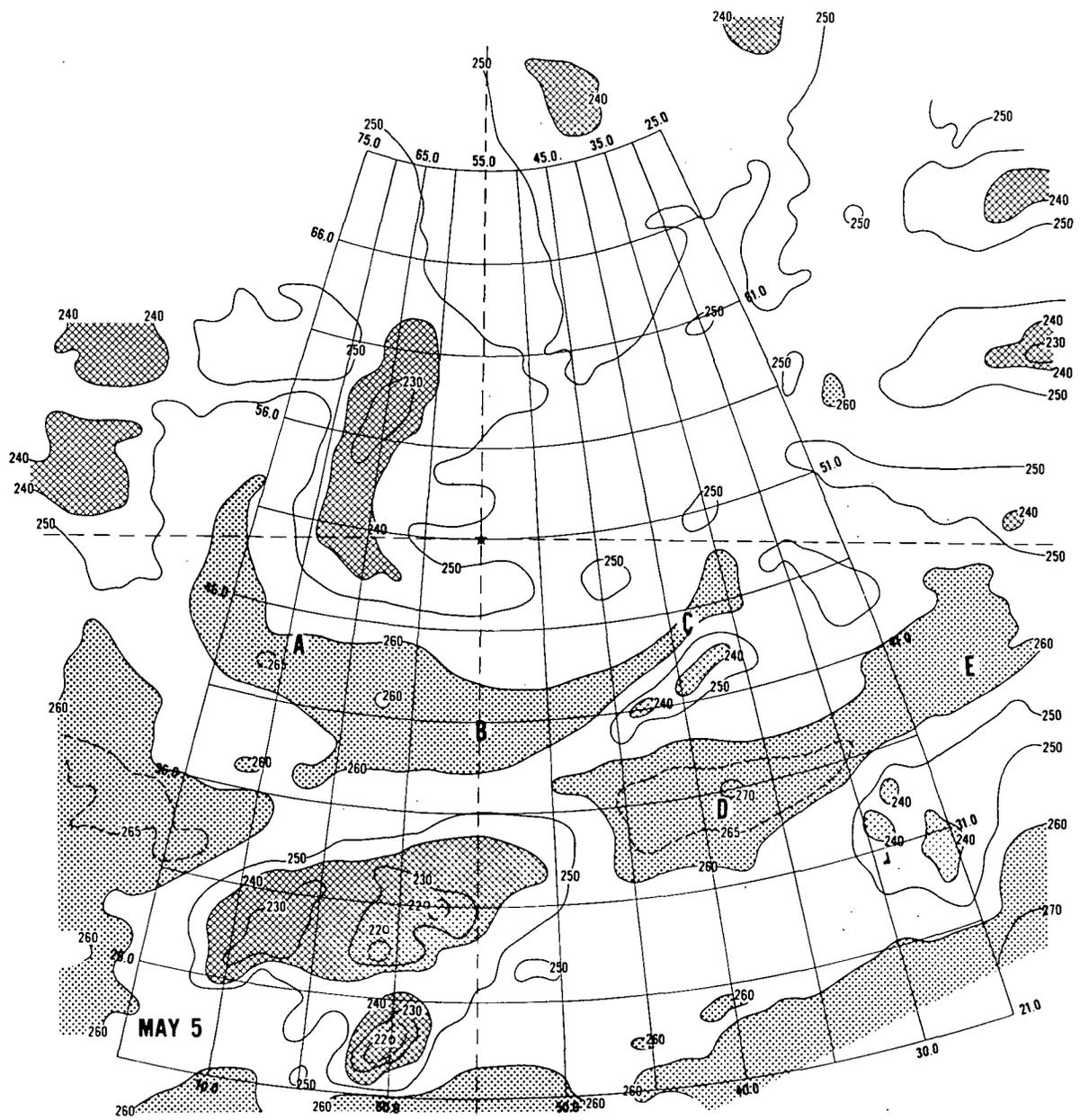
Figure 16 (concluded).—Radiation maps for May 5, 1969. (d) 20- to 23-μm. Isotherms are in °Kelvin.
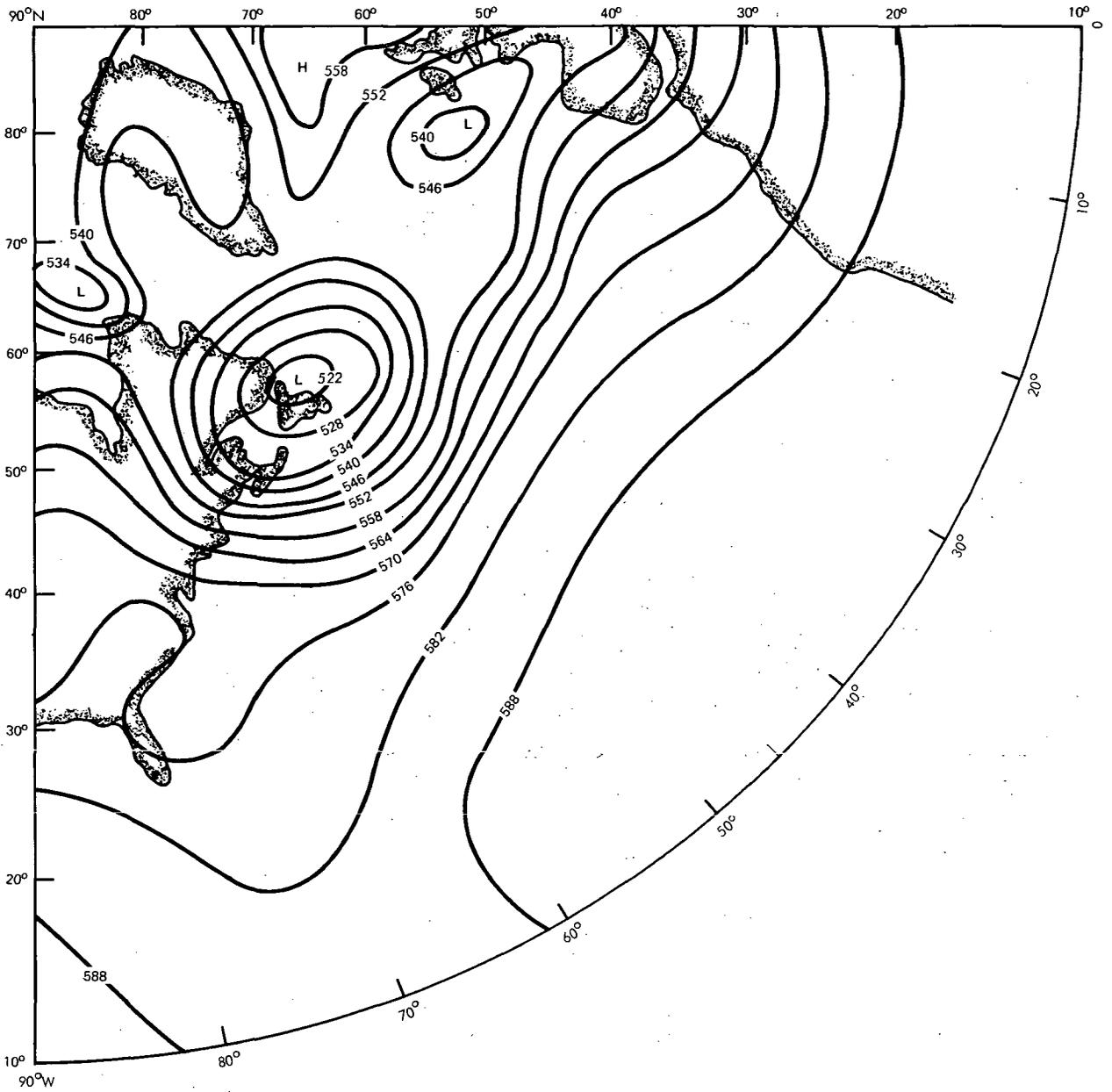
Figure 17.—NMC 50-kN·m⁻² (500-mb) chart for 1200 GMT May 5, 1969 with geopotential heights in decameters.

CLOUD-TYPE DECISION LEGEND

1. CIRRUS
2. CIRRUS WITH LOW CLOUDS
3. CIRROSTRATUS AND / OR CUMULONIMBUS
4. CUMULONIMBUS
5. MIDDLE CLOUDS

6. MIDDLE CLOUDS WITH CIRRUS ABOVE
7. STRATUS OR STRATOCUMULUS
8. CUMULUS
9. CLEAR
10. NO DECISION
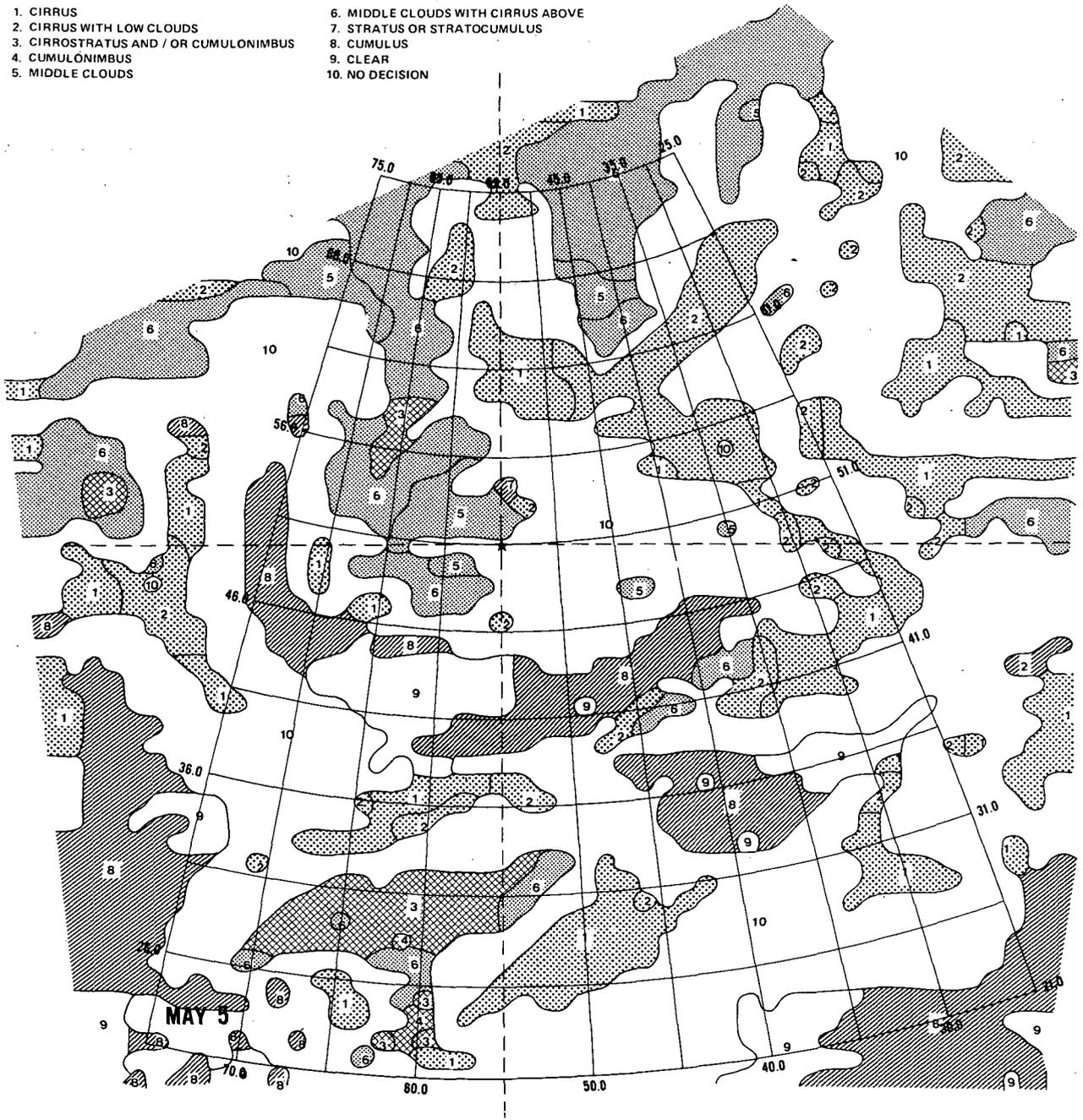
Figure 18.—Cloud-type decision map, May 5, 1969.
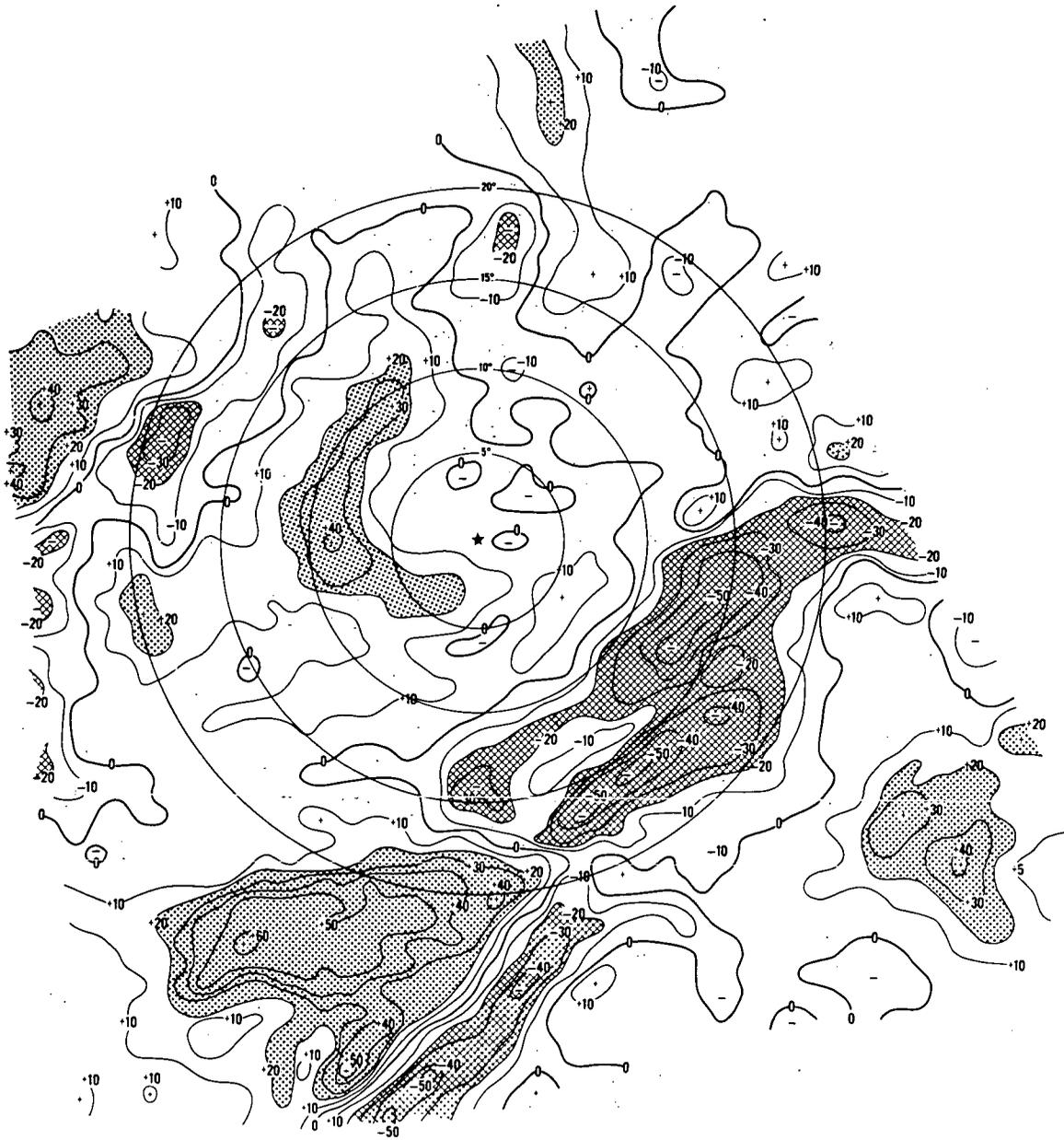
Figure 19. Radiation difference maps for May 5 and 6, 1969. (a) 10- to 11-μm. Isolines are equivalent blackbody temperature differences in °Kelvin. The circles are in degrees of latitude from the cyclone center.

Figure 19 (continued).—Radiation difference maps for May 5 and 6, 1969. (b) 0.2- to 4.0-μm. Isolines are normalized reflectance differences in percent. The circles are in degrees of latitude from the cyclone center.
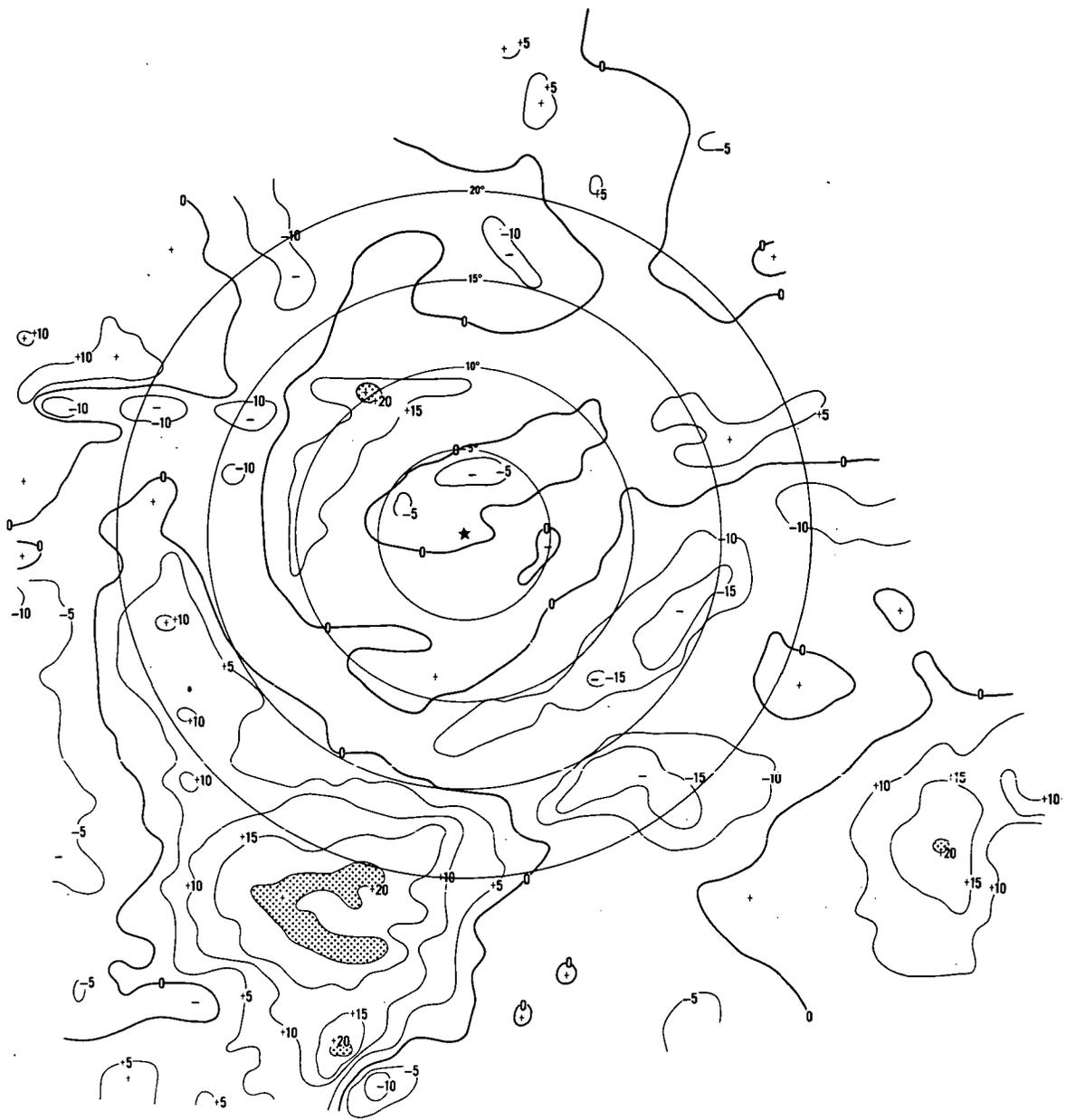
Figure 19 (continued).—Radiation difference maps for May 5 and 6, 1969. (c) 6.5- to 7.0-μm. Isolines are equivalent blackbody temperature differences. The circles are in degrees of latitude from the cyclone center.

Figure 19 (concluded).—Radiation difference maps for May 5 and 6, 1969. (d) 20- to 23-μm. Isolines are equivalent blackbody temperature differences. The circles are in degrees of latitude from the cyclonic center.
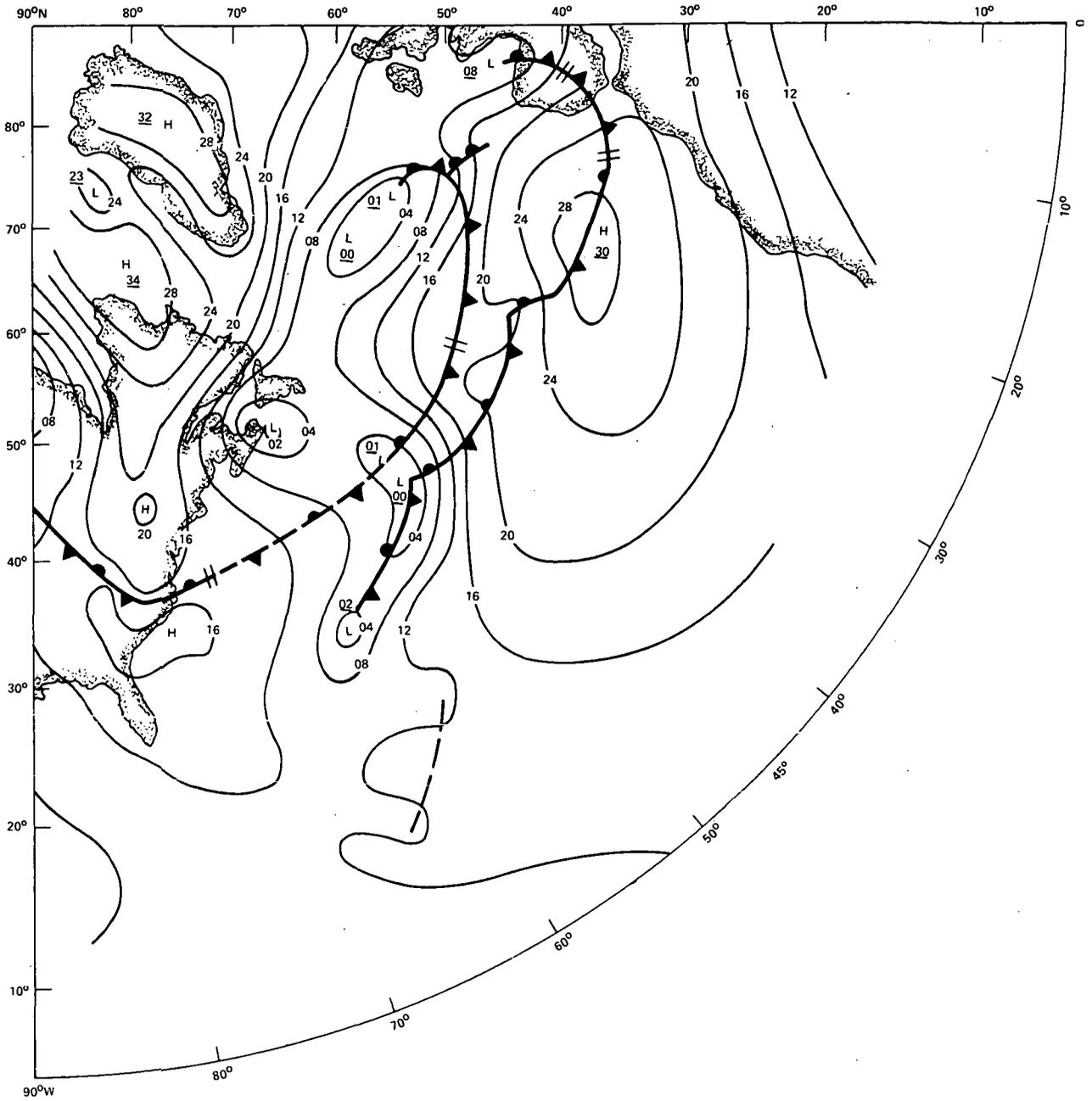
Figure 20.—NMC surface chart, 1200 GMT May 6, 1969.
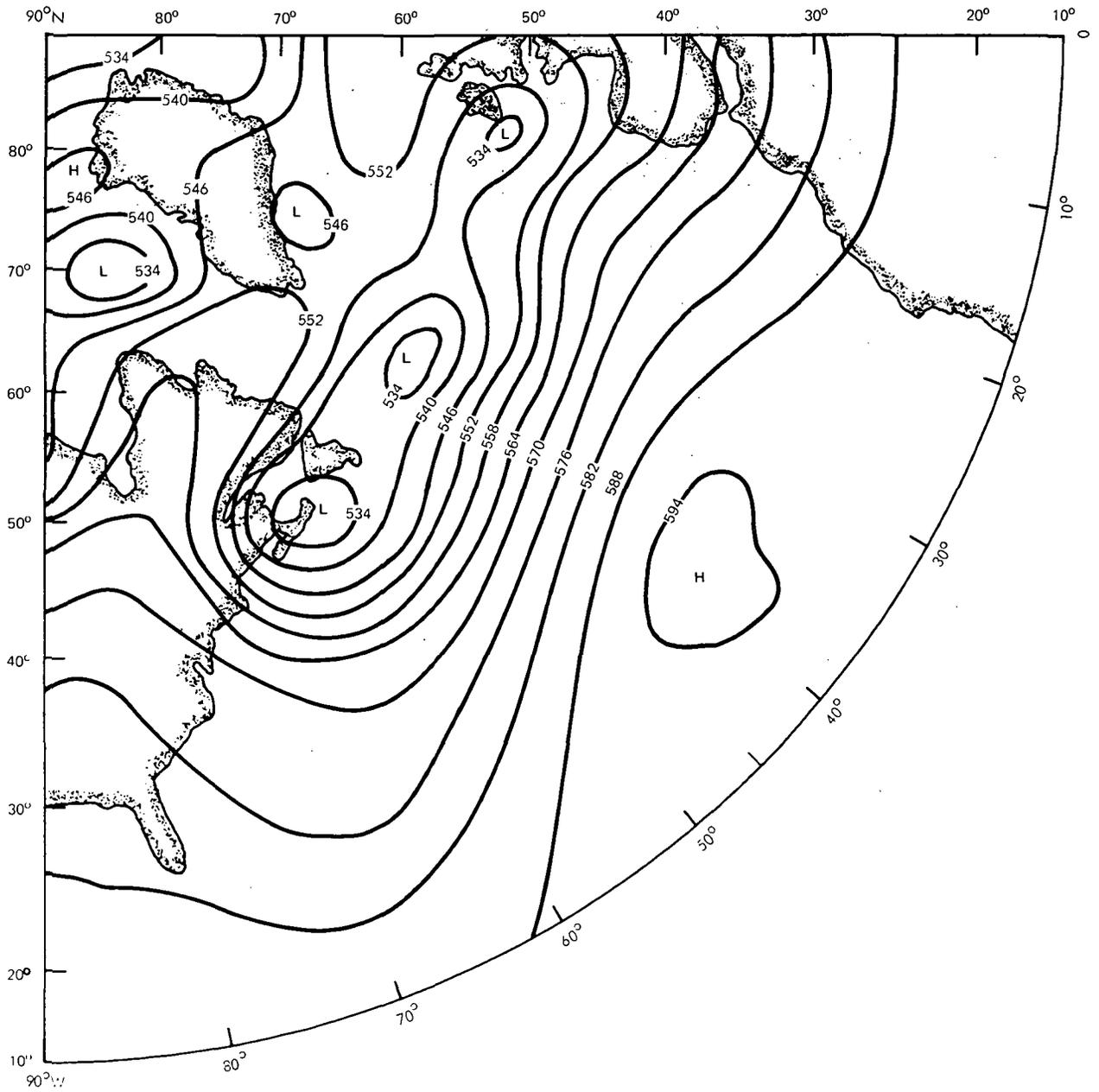
Figure 21.—NMC 50 kN·m^{-2} (500-mb) chart for 1200 GMT May 6, 1969 with geopotential heights in decameters.
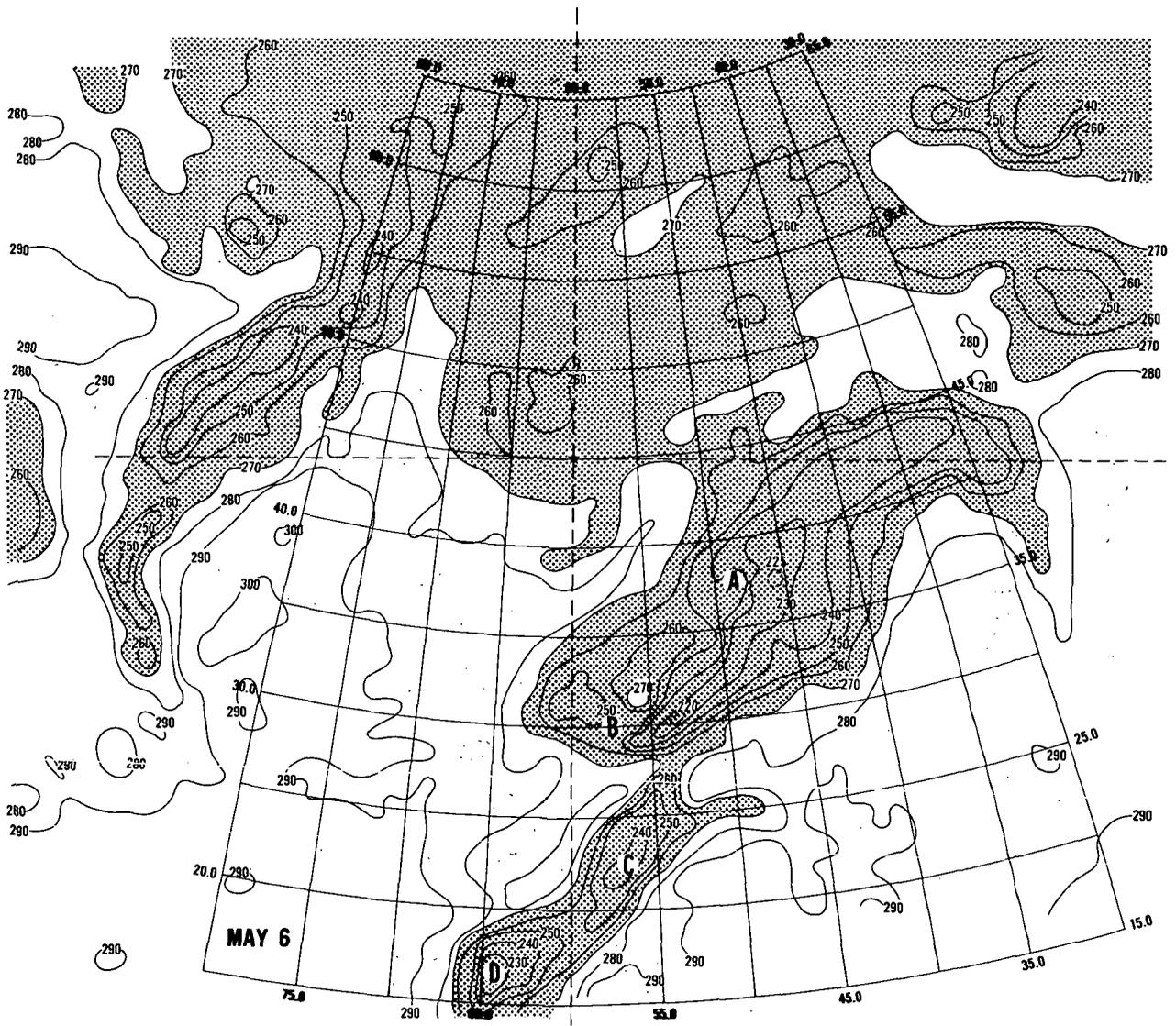
Figure 22.—Radiation maps for May 6, 1969. (a) 10- to 11-μm. Isotherms are in °Kelvin.
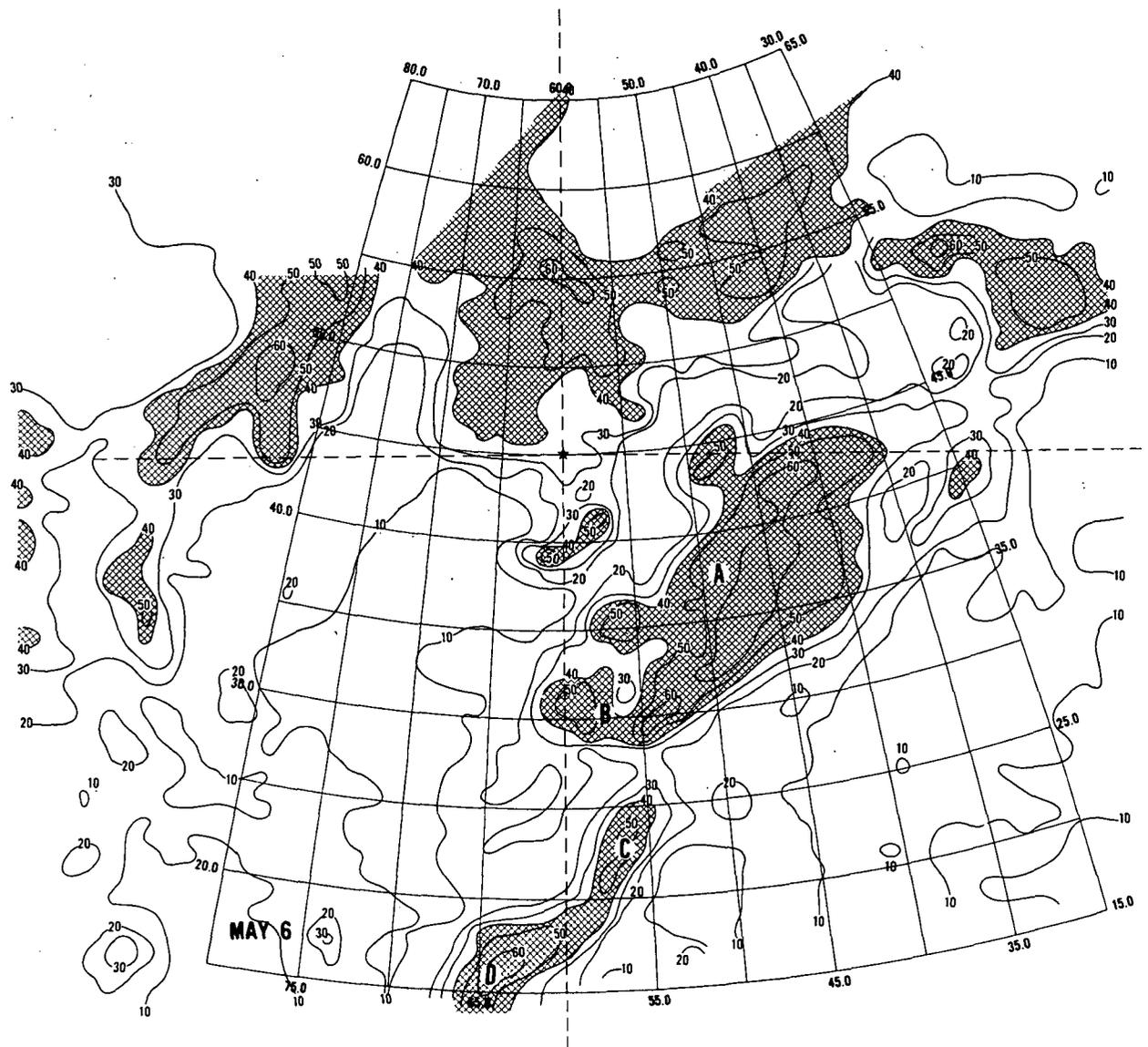
Figure 22 (continued).—Radiation maps for May 6, 1969. (b) 0.2- to 4.0-μm.   Isolines are normalized reflectances in percent.
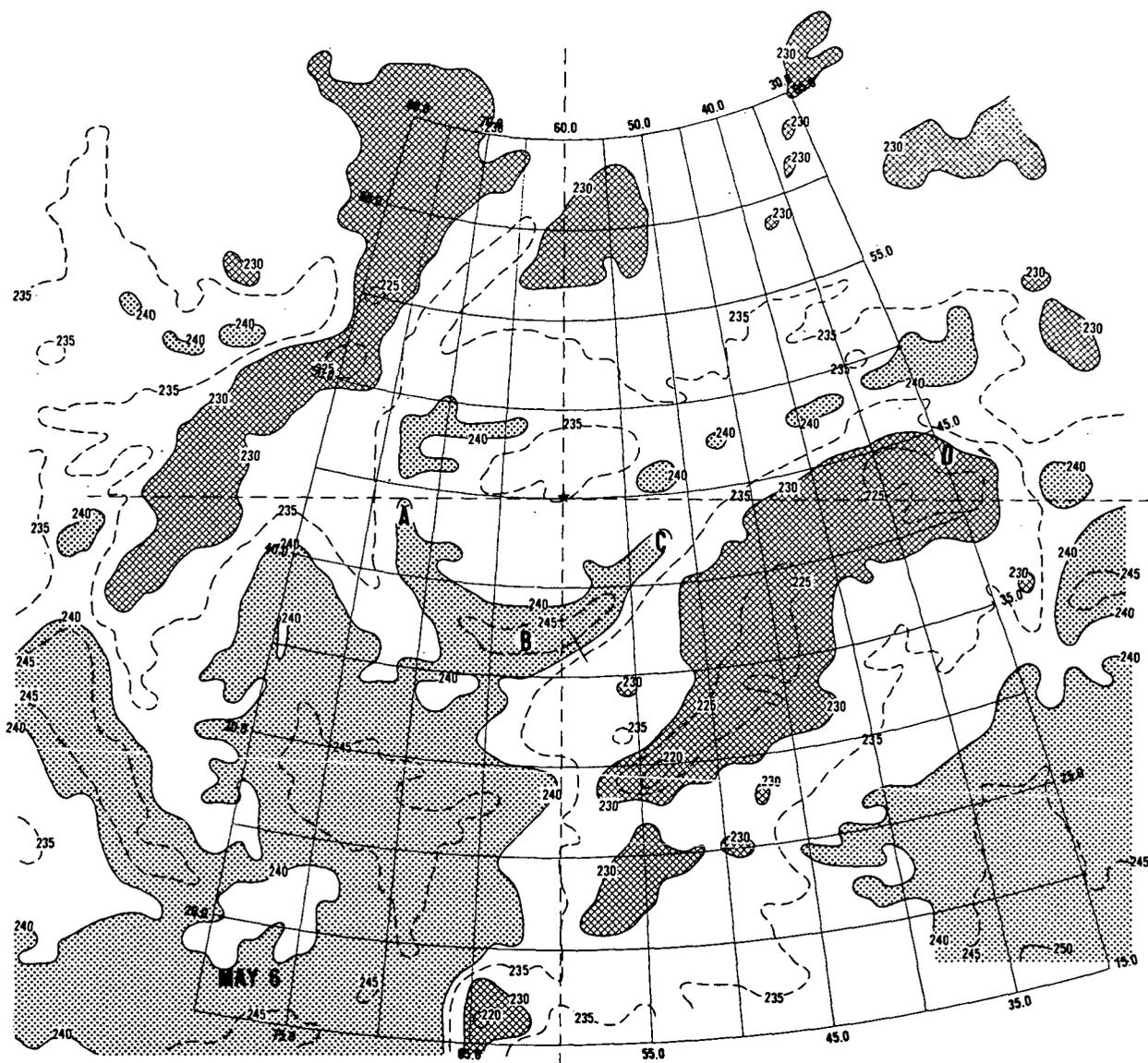
Figure 22 (continued).—Radiation maps for May 6, 1969. (c) 6.5- to 7.0-μm. Isotherms are in °Kelvin.
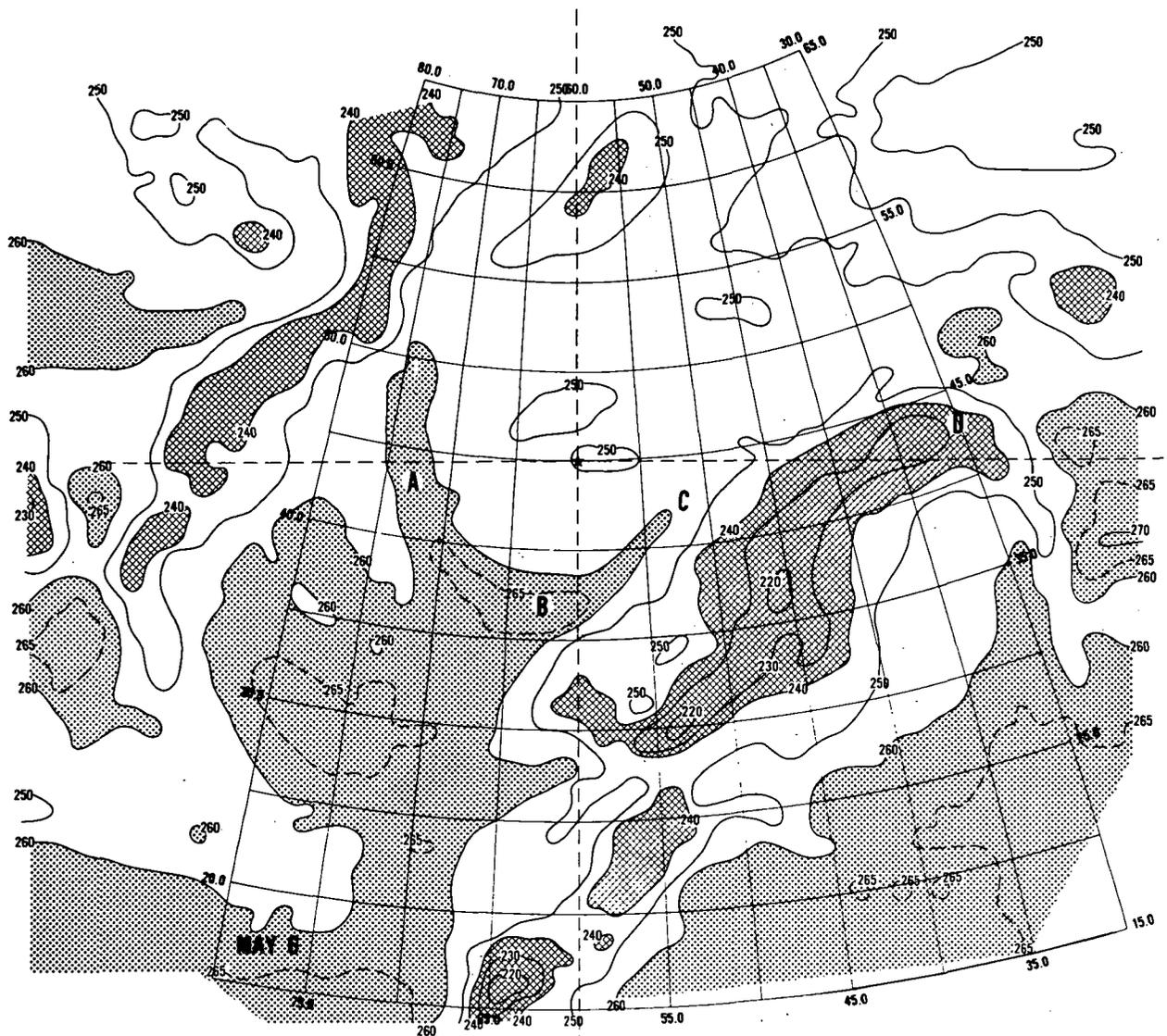
Figure 22 (concluded).—Radiation maps for May 6, 1969. (d) 20- to 23-µm. Isotherms are in °Kelvin.
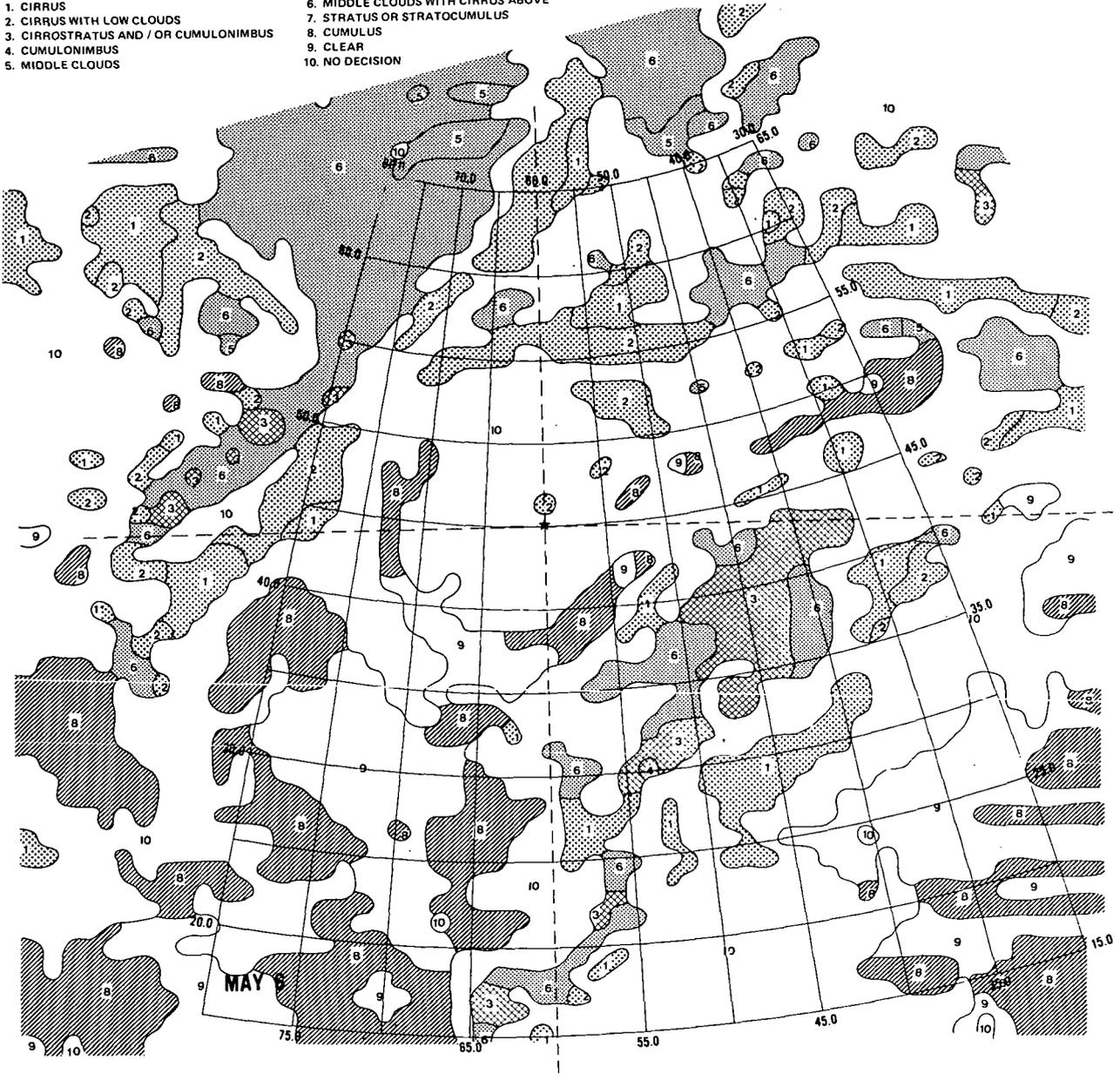
Figure 23.—Cloud-type decision map, May 6, 1969.

Page Intentionally Left Blank

APPENDIX A

CLOUD-TYPE DECISION CRITERIA

Unique cloud-type signatures were determined from MRIR data by Barnes and Chang (ref. 28) using Nimbus 2 photographic and radiometric data. Later, Greaves and Chang (ref.29) developed cloud-type signatures with radiometric measurements obtained by the Nimbus 2 MRIR. A statistical analysis of the 6.4- to 6.9-, 10- to 11-, and 0.2- to 4.0-μm data from this sensor produced signatures for five different cloud types:

(1) Stratus/stratocumulus

(2) Altocumulus

(3) Cirrus

(4) Cumulus (less than 50 percent cover)

(5) Cumulonimbus

A test of independent cases showed the difficulty in identifying cumulus-type clouds on a point-by-point basis, although results for the first three types were quite encouraging. Greaves and Chang therefore concluded that not only were multispectral cloud-identification techniques valid, but that they also offered great promise for automated computer-recognition schemes.

The computer generated cloud-type decision maps produced for this study continued the development of multispectral cloud-type decision mapping. In addition to the three channels employed by Greaves and Chang, the 20- to 23-μm region was used, because this channel is sensitive to water vapor in the middle troposphere and should offer further definition of the presence of midlevel clouds. Four additional cloud-type categories were added together with a "no-decision" case. The no-decision case is reserved for points for which confidence is not high enough to make a decision. As shown in the previous studies, uneven and broken layers of clouds offer a confusing array of spectral signals. Cloud elements partially filling the field of view of the sensor can also vary in size and height to produce similar amounts of upwelling radiation. The same effect can be produced by variation in the emissivity of high and midlevel clouds. Thus the signatures for the nine cloud types used have been restricted to cloud conditions where high confidence could be placed in the decisions. However, even this case adds some knowledge if the conditions for its selection are understood. In many cases, the reason for its selection can be determined by examination of surrounding points where cloud decisions have been made.

Table A-1.—Cloud-Type Decision Criteria for the Four MRIR Channels

Number and cloud type	Latitudes where valid	T_{bb}, K			Percent reflectance R (0.2 to 4 μm)
		6.5 to 7 μm	20 to 23 μm	10 to 11 μm	
1. Cirrus	South of 38° N	<235	<255	≤270	<25
	North of 38° N	<235	<255	<265	<25
2. Cirrus with low clouds	South of 38° N	<235	<255	<270	<25
	North of 38° N	<235	<255	<265	<25
3. Cirrostratus and/or cumulonimbus	All latitudes	<230	<235	<240	50 ≤ R ≤ 65
4. Cumulonimbus	All latitudes	<225	<225	<225	>65
5. Middle clouds	All latitudes	≤235	<255	260 ≤ T_{bb} ≤ 280	≤45
6. Middle clouds with cirrus above	All latitudes	225 ≤ T_{bb} < 235	<250	240 ≤ T_{bb} < 260	<45
7. Stratus or stratocumulus	South of 38° N	≤240	<260	≤280	<45
	North of 38° N	≤240	≤250	≤260	<45
8. Cumulus	South of 38° N	<240	≤255	<280	10 ≤ R < 45
	North of 38° N	≤240	≤250	<265	10 ≤ R < 45
9. Clear	South of 38° N	≤240	<260	<290	<10
	North of 38° N	≤240	<255	<270	<10
10. No decision	All latitudes	–	–	–	–

The 10 decisions and the radiation signatures for the nine cloud-type combinations are shown in table A-1. The work by Greaves and Chang (ref. 29) and by Shenk and Salomonson (ref. 30) was used to help establish the criteria. Some subjective values, however, had to be employed. Reflectance values were a special problem. Although some reflectances have been determined for cirrus and low clouds such as stratus, there is little information available for midlevel or layered clouds over the 0.2- to 4.0-μm spectral interval. Variations in surface reflectances also introduce some difficulties in establishing background values over land. Over land areas cumulus cloud-type selections must be cautiously interpreted because they might represent situations where clear conditions over land masses have reflectances greater than those established for the clear threshold value. In this study, the difficulty was minimized because the storm circulation was mostly over the ocean. Another problem is global variation in temperatures. This was treated with a latitude separation that delineated two different sets of decision criteria.

Verification of the cloud decision maps was somewhat subjective based on the interpretation of Nimbus 3 IDCS pictures. Cloud-type identifications from the IDCS photography matched very well with the automated product over fairly uniform cloud masses. The no-decision case was predominant where the clouds appeared to vary dramatically in either coverage or height (interpreted from cloud types). It was obvious that the resolution of the MRIR sensor could not describe these occurrences. Some ship observations were also studied and although good agreement was noted in several areas, they were of little use in multilayer situations. For these reasons, evaluation of the technique had to be indicated in part by the results themselves. When consideration is given to the expected cloud structure of an extratropical storm, the daily patterns appeared to be reasonable. Of considerable value was the fact that this approach insured cloud-type interpretation consistency throughout the period investigated.

REFERENCES

1. Shenk, W. E.; and Salomonson, V. V.: "Visible and Infrared Imagery From Meteorological Satellites." *Appl. Opt.* **9**(8): 1747-1760, 1970.

2. Fritz, S.; and Wexler, H.: "Cloud Pictures From Satellite Tiros I." *Mon. Weather Rev.* **88**(3): 79-87, 1960.

3. Stroud, W. G.: "Initial Results of the Tiros I Meteorological Satellite." *J. Geophys. Res.* **65**(5): 1643-1644, 1960.

4. Fritz, S.; and Winston, J. S.: "Synoptic Use of Radiation Measurements From Satellite Tiros II." *Mon. Weather Rev.* **90**(1): 1-9, 1962.

5. Nagle, R. E.; and Serebreny, S. M.: "Radar Precipitation Echo and Satellite Cloud Observations of a Maritime Cyclone." *J. Appl. Meteorol.* **1**(3): 279-295, 1962.

6. Anderson, R. K.; Ferguson, E. W.; and Oliver, V. J.: *The Use of Satellite Pictures in Weather Analysis and Forecasting.* WMO Tech. Note 75, World Meteorological Organization, 1966.

7. Anderson, R. K.; et al.: *Application of Meteorological Satellite Data in Analysis and Forecasting.* ESSA Tech. Rept. NESC 51, National Weather Satellite Center, June 1969.

8. Weinstein, M.; and Suomi, V. E.: "Analysis of Satellite Infrared Radiation Measurements on a Synoptic Scale." *Mon. Weather Rev.* **89**: 419-428, 1961.

9. Sherr, P.; and Rogers, C.: *The Identification and Interpretation of Cloud Vortices Using Tiros Infrared Observations.* Final Rept. (Contract CWB-10812), ARACON Geophysics Co., Concord, Mass., Mar. 1965.

10. Shenk, W. E.: "Meteorological Satellite Infrared Views of Cloud Growth Associated With the Development of Secondary Cyclones." *Mon. Weather Rev.* **98**(11), Nov. 1970.

11. Hunter, H. E.; and Kemp, N. H.: *Application of AVCO Data Analysis and Prediction Techniques (ADAPT) to Prediction of Cyclone Central Pressure and Its Derivatives Using Nimbus HRIR Data.* Final Rept., pt. I, AVSD-0362-70-RR, AVCO Corp., Aug. 1970.

12. Hunter, H. E.; and Kemp, N. H.: *Application of AVCO Data Analysis and Prediction Techniques (ADAPT) to Prediction of Cyclone Central Pressure and Its Derivatives Using Nimbus HRIR Data.* Final Rept., pt. II, AVSD-0142-71-RR, AVCO Corp., Mar. 1971.

13. Hunter, H. E.; and Kemp, N. H.: *Application of AVCO Data Analysis and Prediction Techniques (ADAPT) to Prediction of Cyclone Central Pressure and Its Derivatives Using Nimbus HRIR Data.* Final Rept., pt. III, AVSD-0334-71-RR, AVCO Corp., July 1971.

14. Rogers, C.; and Sherr, P.: *A Study of Dynamical Relationships Between Cloud Patterns and Extratropical Cyclogenesis.* Final Rept. (Contract E-47-67(N)), Allied Research Associates, Inc., Concord, Mass., Sept. 1967.

15. Nordberg, W.: *Interpretation of Radiation Data From Meteorological Satellites.* NASA TM X-63314, 1968.

16. Bandeen, W. R.: *Experimental Approaches to Remote Atmospheric Probing in the Infrared From Satellites.* NASA TM X-63188, 1968.

17. Beran, D. W.; Merritt, E. S.; and Chang, D. T.: *Interpretation of Baroclinic Systems and Wind Fields as Observed by Nimbus II MRIR.* Final Rept. (Contract NAS5-10334), Allied Research Associates, Inc., Concord, Mass., 1968.

18. Martin, F. L.; and Salomonson, V. V.: "Statistical Characteristics of Subtropical Jet Stream Features in Terms of MRIR Observation From Nimbus II." *J. Appl. Meteorol.* 9(3): 508-520, 1970.

19. Raschke, E.; and Bandeen, W. R.: "A Quasi-Global Analysis of Troposphere Water Vapor Content From Tiros IV Radiation Data." *J. Appl. Meteorol.* 6: 468-481, 1967.

20. Fritz, S.; and Rao, A. K.: "On the Infrared Transmission Through Cirrus Clouds and the Estimation of Relative Humidity From Satellites." *J. Appl. Meteorol.* 6(6): 1088-1096, 1967.

21. *Nimbus 3 Users' Guide.* National Space Science Data Center, NASA GSFC, 1969.

22. Shenk, W. E.; Powell, H.; Salomonson, V. V.; and Bandeen, W. R.: "Meteorological Uses of the Stereographic Horizon Map Projection." *J. Appl. Meteorol.* 10(3): 581-589, 1971.

23. Miller, J. E.: "Cyclogenesis in the Atlantic Coastal Region of the United States." *J. Meteorol.* 3: 31-44, 1946.

24. Mather, J. R.; Adams, H.; and Yoshioka, G. A.: "Coastal Storms of the Eastern United States." *J. Appl. Meteorol.* 3(6): 693-706, 1964.

25. Rodgers, E. B.; and Salomonson, V. V.: "A Quantitative Evaluation of the Nimbus Water Vapor Observations as Related to Middle and Upper Tropospheric Circulation Features." 1971 Fall Annual Meeting, Amer. Geophys. Union (San Francisco), Dec. 6-9, 1971.

26. Shenk, W. E.: "Tiros II Window Radiation and Large Scale Vertical Motions." *J. Appl. Meteorol.* 2(6): 770-775, 1963.

27. Kong Sam Pak: "Meteorological Application of Satellite Window Radiation." *J. Appl. Meteorol.* 9(3): 521-529, 1970.

28. Barnes, J. C.; and Chang, D.: *Accurate Cloud Cover Determination and Its Effects on Albedo Computations.* Final Rept. (NAS5-10478), Allied Research Associates, Inc., Concord, Mass., Oct. 1968.

29. Greaves, J. R.; and Chang, D. T.: *Technique Development to Permit Optimum Use of Satellite Radiation Data.* Final Rept., N62306-69-C-0227, Allied Research Associates, Inc., Concord, Mass., May 1970.

30. Shenk, W. E.; and Salomonson, V. V.: "A Multispectral Technique to Determine Sea Surface Temperature Using NIMBUS 2 Data." *J. Phys. Oceanogr.* 2: 157-167, 1972.

"*The aeronautical and space activities of the United States shall be
conducted so as to contribute . . . to the expansion of human knowl-
edge of phenomena in the atmosphere and space. The Administration
shall provide for the widest practicable and appropriate dissemination
of information concerning its activities and the results thereof.*"
—NATIONAL AERONAUTICS AND SPACE ACT OF 1958

NASA SCIENTIFIC AND TECHNICAL PUBLICATIONS

TECHNICAL REPORTS: Scientific and
technical information considered important,
complete, and a lasting contribution to existing
knowledge.

TECHNICAL NOTES: Information less broad
in scope but nevertheless of importance as a
contribution to existing knowledge.

TECHNICAL MEMORANDUMS:
Information receiving limited distribution
because of preliminary data, security classifica-
tion, or other reasons. Also includes conference
proceedings with either limited or unlimited
distribution.

CONTRACTOR REPORTS: Scientific and
technical information generated under a NASA
contract or grant and considered an important
contribution to existing knowledge.

TECHNICAL TRANSLATIONS: Information
published in a foreign language considered
to merit NASA distribution in English.

SPECIAL PUBLICATIONS: Information
derived from or of value to NASA activities.
Publications include final reports of major
projects, monographs, data compilations,
handbooks, sourcebooks, and special
bibliographies.

TECHNOLOGY UTILIZATION
PUBLICATIONS: Information on technology
used by NASA that may be of particular
interest in commercial and other non-aerospace
applications. Publications include Tech Briefs,
Technology Utilization Reports and
Technology Surveys.

Details on the availability of these publications may be obtained from:

SCIENTIFIC AND TECHNICAL INFORMATION OFFICE

NATIONAL AERONAUTICS AND SPACE ADMINISTRATION
Washington, D.C. 20546